Probing the Magnetic Fields of Distant Galaxies to Unravel the Evolution of Galactic Magnetic Fields

Rikuto Omae

March 2024

Abstract

Galactic Magnetic fields play important roles in various astrophysical processes. There are unresolved problems about Galactic magnetic fields. One of the problems is that the cosmological evolution of galactic magnetic field is largely unknown. To solve this problem, we need to observe magnetic fields of distant galaxies.

First, Observation of the magnetic fields of distant galaxies can be achieved by observing intervening galaxies. External galaxies often intervene in front of background radio sources such as quasars and radio galaxies. Linear polarization of the background emission is depolarized by Faraday rotation of inhomogeneous magnetized plasma of the intervening galaxies. Exploring the depolarizing intervening galaxies (DINGs) can be a powerful tool to investigate the cosmological evolution of the galactic magnetic field. In this theisis, we focus on the global disk magnetic field, a primary component of galactic magnetic fields, and investigate the effects of DINGs on background radio emission using a simple model. We find that the degree of depolarization significantly depends on the inclination angle and the impact parameter of the DING. We found that the larger the standard deviation, the more likely it is that depolarization will occur. When the DING is close to an edge-on view, depending on the angular size of the background source relative to the DING, the polarization fraction converges, behaving like oscillations at low frequencies. The Faraday dispersion function (FDF) represents the RM structure within the beam. The FDF exhibits multi components due mainly to the RM structure within the beam and the fraction of the DING that covers the background emission (the filling factor). The peak Faraday depth of the FDF is different from the beam-averaged RM of the DING. The Monte-Carlo simulations indicate that DING's contribution to the standard deviation of observed RMs follows $\sigma_{\rm RM} \propto 1/(1+z)^k$ with $k \sim 2.7$ and exhibits a steeper redshift dependence than the wavelength squared. DINGs will have a significant impact on RM catalogs created by future survey projects such as the SKA and SKA Precursor/Pathfinder.

Next, the applying the gravitational lensing effect has been considered as an observation of the magnetic field of distant galaxies. Mao et al. (2017) [1] used Faraday tomography to determine the magnetic field from the difference in Faraday depths at which the emission of the background source passes through different positions of the intervening galaxy due to the gravitational lensing effect. In the future, it is expected to find many polarization sources affected by gravitational lensing effects. All-sky polarization surveys using the SKA predecessor have now begun. We focus on the "Polarisation Sky Survey of the Universe's Magnetism" (POSSUM) with the Australian SKA Pathfinder (ASKAP). However, POSSUM may not be able to spatially resolve gravitational lensing sources. Previously, we have shown that Faraday spectrum represents the RM structure within the beam, even when they are unresolved. We investigate whether the RM structure of lensing galaxies can be extracted from the spectra. We

used a model fitting method that fits stokes Q and U spectra to extract the RM structure of lensing galaxies. At first, we consider the simple case that the RM structure is uniform on each path. In this case, using the model which has 2 components of RM, we can get the mean and variance of the RMs experienced by each path and these values are the same as given RM structures, even if they were not spatially resolved. Next, we consider the case of the existence of RM structure within the beam (complex case). In this case, using the model which has multi components of RM, comparing the observed spectrum with the model spectrum, we found a good match. However, we found physically strange values in the parameters. In particular, the polarization angle of the background polarization source is different from given angle. To solve this problem, we propose reducing the polarization angle of the background polarization source as the parameter. In the case of gravitational lensing objects, we can impose the requirement that the polarization angle of the background polarization source is the same. We can reduce one parameter. In the case of imposing this requirement, we found the model which has multi components of RM is the best fitting model. The polarization angle of the background polarization source is the same as given angle and we resolve uncertainty about the polarization angle. We could separate complex RM structure of unsolved source. It does not matter whether the radio image is spatially resolved or not and we will attempt to resolve the lensed components.

Contents

1 Introduction **1**
1.1 Galactic magnetic fields 1
1.1.1 Origin of galactic magnetic fields 2
1.2 Observations of magnetic fields in galaxies 2
1.2.1 Optical Polarization 3
1.2.2 Dust polarization 5
1.2.3 Zeeman effect 5
1.2.4 Radio synchrotron emission 7
Rotation measure 8
Depolarization 9
1.3 Dynamo theory 10
1.3.1 Mean-field dynamos 10
1.3.2 Small-scale dynamos 12
1.4 Theoretical models of galactic magnetic fields 12
Magnetic fields models of Milky Way galaxy 13
1.5 Evolution of galactic magnetic fields 14
1.6 Aim of the thesis 17

2 Effects of Depolarizing Intervening Galaxies on Background Radio Emission **19**
2.1 Introduction 19
2.2 Model and calculation 20
2.2.1 Numerical models 20
2.2.2 Observing specification and calculation 21
2.3 Results 24
2.3.1 Depolarization caused by a DING 24
2.3.2 Estimation of DING's RM 28
2.3.3 Statistical contribution of DING 29
2.4 Discussion 31
2.4.1 Model dependence 31
Density profile 31
Disk fields 32
Halo Fields 34

Turbulence 34
2.4.2 Quantification of depolarization 36
2.4.3 Shapes of the Faraday spectrum 38
2.4.4 Redshift dependence of σ_{RM} 39
2.5 Conclusion 42

3 Polarization Analysis of Gravitational Lens Galaxies for Future Polarization Surveys 43
3.1 Introduction 43
3.2 Calculation 44
3.2.1 Fitting models 45
3.2.2 Mock data for fitting 47
3.3 Results 47
3.3.1 Simple case, case1 52
3.3.2 Complex case, case2 52
3.3.3 Statistical results 57
3.4 Discussion 60
3.4.1 Differences in initial polarization angles and RM 60
3.4.2 Identification of well-fitting paths 60
3.5 Conclusion 63

4 Discussion 65
4.1 Estimation of the galactic magnetic field 65
4.2 Detection probability of inclination angles 66
4.3 Future observation of galactic magnetic fields 68
4.4 Impact on other fields 69

5 Summary 70

A Appendix 72
A.1 Polarization observation Stokes parameter 72
A.2 Synchrotron radiation mechanism 75
A.3 Faraday rotation 79
A.4 Faraday tomography 82
A.4.1 QU-fitting 83

Chapter 1

Introduction

1.1 Galactic magnetic fields

The existence of magnetic fields in the interstellar medium (ISM) of the Milky Way and other galaxies has been known for over 60 years. There are various types of galaxies, such as spiral galaxies and elliptical galaxies, and spiral galaxies in particular are known to have magnetic field structures along their spiral arms. Such a magnetic field is called a global magnetic field and has a value of a few μG. In particular, we will focus on the fact that the spiral galaxies often exhibit global magnetic fields over a wide area of the galaxy. How do such global magnetic fields originate and survive in the turbulence and chaos of the interstellar medium? Because global magnetic fields are subject to turbulent diffusion and the time scale of vertical diffusion is typically less than 10 times the age of the Universe [2], these fields must be replenished in situ, no matter what seed magnetic field is supplied. Since diffusion implies exponential decay, growth and replenishment must themselves be exponential. These facts led to the in-situ galaxy dynamo theory and its modeling to explain the large-scale magnetic fields of galaxies.

It is still unclear how magnetic fields affect galaxy formation and evolution [3, 4, 5]. The developing magnetohydrodynamic (MHD) models of galaxies is computationally challenging and requires various simplifications. Thanks to the development of modern high-sensitivity, broadband radio telescopes and new observational and data analysis methods, much more are known about the magnetic fields in the interstellar medium (ISM) of nearby galaxies and the Milky Way. Significant progress has also been achieved in the numerical modeling of the magnetized ISM (e.g. [6, 7, 8, 9, 10]). Naturally, further efforts on both sides are needed, as they do not always agree with observations.

Extensive arguments in the past for ignoring the galactic magnetic field were based on the assumption that the strength of the magnetic field derived from Faraday rotation data of the Milky Way galaxy, which tracks a small fraction of the total magnetic field, is a few μG. The importance of the galactic field dynamically is widely recognized in many areas of astrophysics. Magnetic fields and cosmic ray pressure control the overall star formation rate [11]. Magnetic fields are important for the gas dynamics of molecular clouds [12]. Stronger magnetic fields result in fewer but more massive cloud nuclei being formed [13]. Cosmic rays propagating along magnetic field lines within the galactic halo can heat warm ionized gas, potentially explaining the line ratio [14].

1.1.1 Origin of galactic magnetic fields

The galactic magnetic field consists of a three-step process: (1) seeding, (2) amplification, and (3) ordering and maintaining. Seed fields can be primordial generated in the early Universe [15], or they may form at later stages. For example, they could emerge during cosmic structure formation due to Weibel instabilities [16], from plasma fluctuations within primordial galaxies [17, 18], through emissions from the first stars [19] and the first black holes [20], or via the Biermann mechanism of the first supernova [21]. An efficient source of amplification arises from turbulence triggered by phenomena like supernova explosions [22] or spiral shocks [23], known as small-scale dynamos. This mechanism within protogalaxies can enhance a weak seed to an intensity of a few μG within 10^8 years [24, 25, 26, 27]. The final phase involves the ordering of the turbulent field. Evolving galaxy simulations through numerical models demonstrate the amplification and alignment of rapid magnetic fields aided by differential rotation [3, 28]. This alignment is potentially facilitated by the magnetic rotational instability (MRI) [4, 9]. Within these models, the ordered magnetic field takes shape in helical arm segments but experiences frequent reversals in both azimuthal and radial directions, ultimately resulting in anisotropic turbulence.

1.2 Observations of magnetic fields in galaxies

The spiral galaxies are known to have magnetic field structures along their spiral arms. Such a magnetic field is called a global magnetic field and has a value of a few μG. Because we are in the Milky Way, it is difficult to observe the overall pattern of the magnetic field in the Milky Way. The Planck satellite drive a detailed picture of the magnetic field in the Milky Way through dust polarization measurements in Figure 1.1. It shows that the magnetic field is the most ordered and strongest on the Galactic plane. The Milky Way magnetic field is smooth and regular on large scales, but random on small scales. Synchrotron polarization gradients can be used to extract the properties of ISM turbulence within the Milky Way galaxy [29]. External galaxies show the overall pattern of large-scale magnetic fields. However, the reduced spatial resolution makes it difficult for existing radio telescopes to direct survey the small-scale ISM properties within these systems. The magnetic field of the spiral galaxy M51 was studied in detail by Fletcher et al. (2011) [30]. The regular spiral pattern of the magnetic field shown in figure 1.2 does not produce a similar pattern in Faraday rotation measurements. Thus, the ordered field is a combination of a large-scale (or mean-field) dynamo-generated field and an anisotropic turbulent random field, the correlation length of the small-scale magnetic field is estimated to be about 50 pc by analyzing the polarization resolution of the synchrotron radiation. Many properties of the magnetic fields observed in the

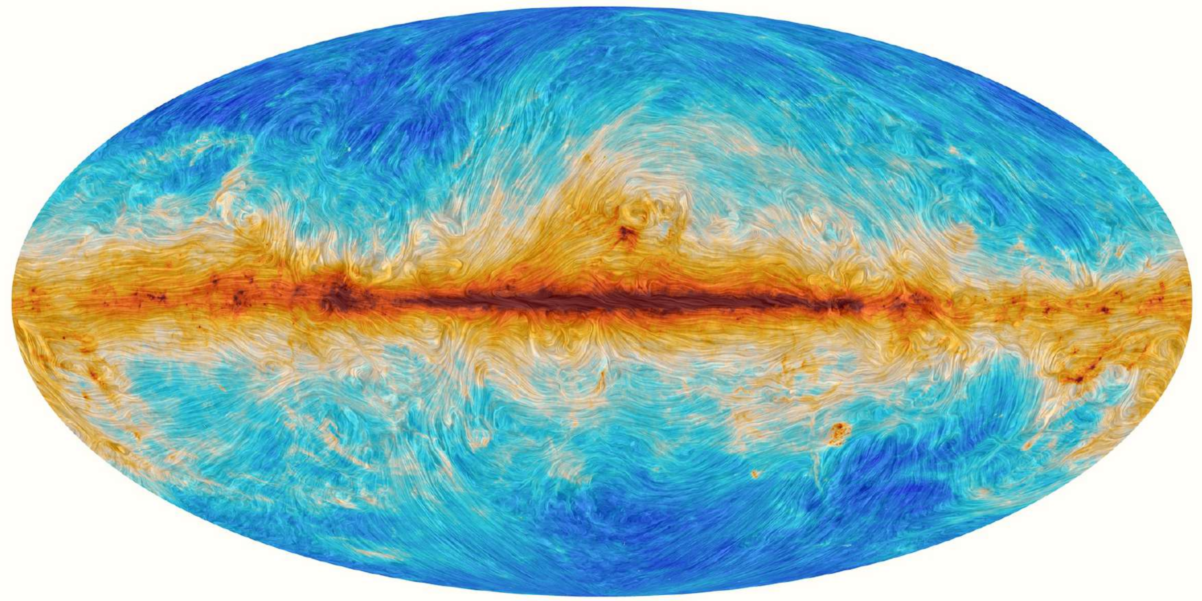

Figure 1.1: Figure taken from Planck ' s webpage - http://www.esa.int/spaceinimages/Images/2015/02/ Polarised emission from Milky Way dust. It shows the dust emission at 353 GHz and the colour scale represents the total intensity of dust emission. The texture shpws show the direction of the Milky Way magnetic field projected on the plane of the sky.

Milky Way and nearby spiral galaxies are consistent with galaxy dynamo theory [31]. It is important to measure the magnetic fields of galaxies with high-z and young galaxies in order to constrain the parameters of galaxy dynamo theory. However, the sensitivity and resolution of existing radio telescopes are limited, making it very difficult to do the same. The magnetic fields of young galaxies have been studied by numerical simulations [5, 32, 33], but there have been few attempts to study the magnetic fields by observation. Magnetic field observations of distant galaxies will be discussed in section 1.5.

1.2.1 Optical Polarization

Dust particles are aligned with the local galactic magnetic field because of the magnetic moment (Davis-Greenstein effect [34]). The major axis of the dust is perpendicular to the interstellar magnetic field lines. Starlight coming from behind the dust is quenched

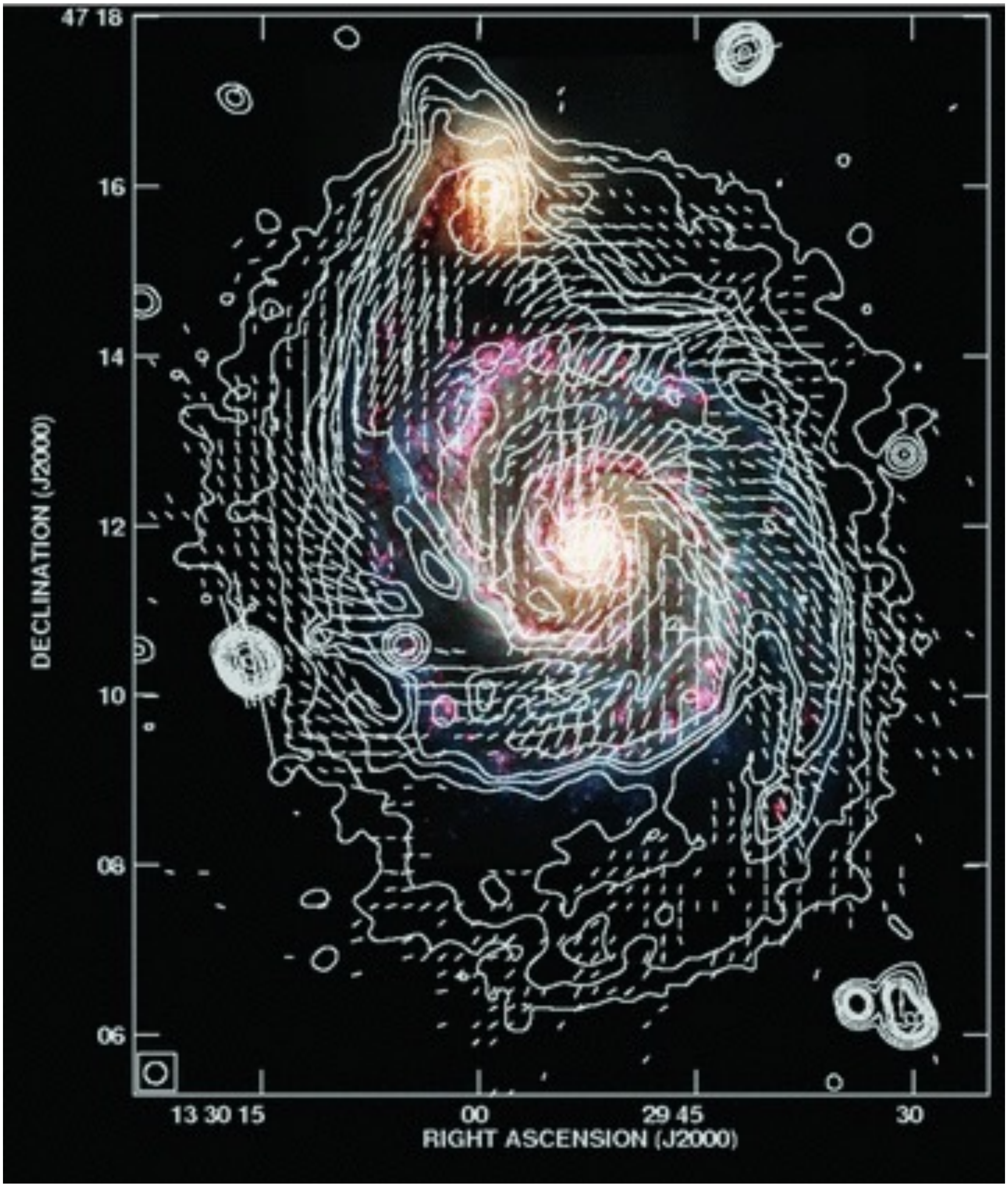

Figure 1.2: Contours of $\lambda 20$ cm total radio emission at 15 arcsec resolution, overlaid on the same optical image from [30]. Also shown are the B-vectors of polarized emission: the plane of polarization of the observed electric field rotated by 90°, not corrected for Faraday rotation.

to different degrees along its major and minor axes. The linear polarization (E-vector) of the starlight is parallel to the magnetic field components projected onto the sky plane. The resulting linearly polarized light also depends on the properties of the dust, especially its size and magnetic properties. Extinction is most efficient for particles with sizes close to their wavelength.

Polarization of stellar light has been used to determine the direction of the large-scale magnetic fields of the Milky Way Galaxy, M51[35] in Figure , NGC 6946[36], and the Small Magellanic Cloud[37]. There are problems with this method: the light may be polarized by scattering, which is independent of the magnetic field. In addition, the spatial sampling is sharply coarsened in high-density interstellar clouds because of high attenuation and few background stars.

1.2.2 Dust polarization

The type of polarization is due to background light stars as well as dust particles emitting at the sub-millimeter and far-infrared wavelengths. The direction of this polarized light (E-vector) is perpendicular to the magnetic field. The properties of this polarized radiation also depend on the properties of the dust particles. This polarized radiation is not affected by scattering. It has been used to observe the magnetic field structure of the Milky Way gas cloud massive star forming site W51 [38] and the magnetic field structure of the galaxy NGC 891 [39].

In the interstellar medium, the magnetic force (total magnetic field strength B_{tot}) competes with the kinetic force due to turbulent gas motion (turbulent velocity v_{turb} and density ρ).The perpendicular component of total field strength $B_{tot,\perp}$ of the sky plane can be estimated from the following equation [40].

$$B_{tot,\perp} \sim \sqrt{\frac{4}{3}\pi\rho}\frac{v_{turb}}{\sigma}. \tag{1.1}$$

σ is the dispersion of the direction of the polarization angle. In a strong magnetic field, σ is small because the magnetic field lines are straight. This method is called the Chandrasekhar-Fermi method.

1.2.3 Zeeman effect

The Zeeman effect is one of the most direct methods of magnetic field observation. A magnetic field splits the electron energy levels of an atom and depends on the strength of the magnetic field. This is called the Zeeman effect (Zeeman splitting). This is a direct observation of the magnetic field, not a tracer as described above. When measuring the magnetic field strength in interstellar space, Zeeman splitting has been observed in the 21cm emission lines of neutral hydrogen atoms, emission and absorption lines of OH molecules, and emission lines of CN molecules. However, the frequency difference of the radio spectral lines is so small that they can be used only in the strong magnetic

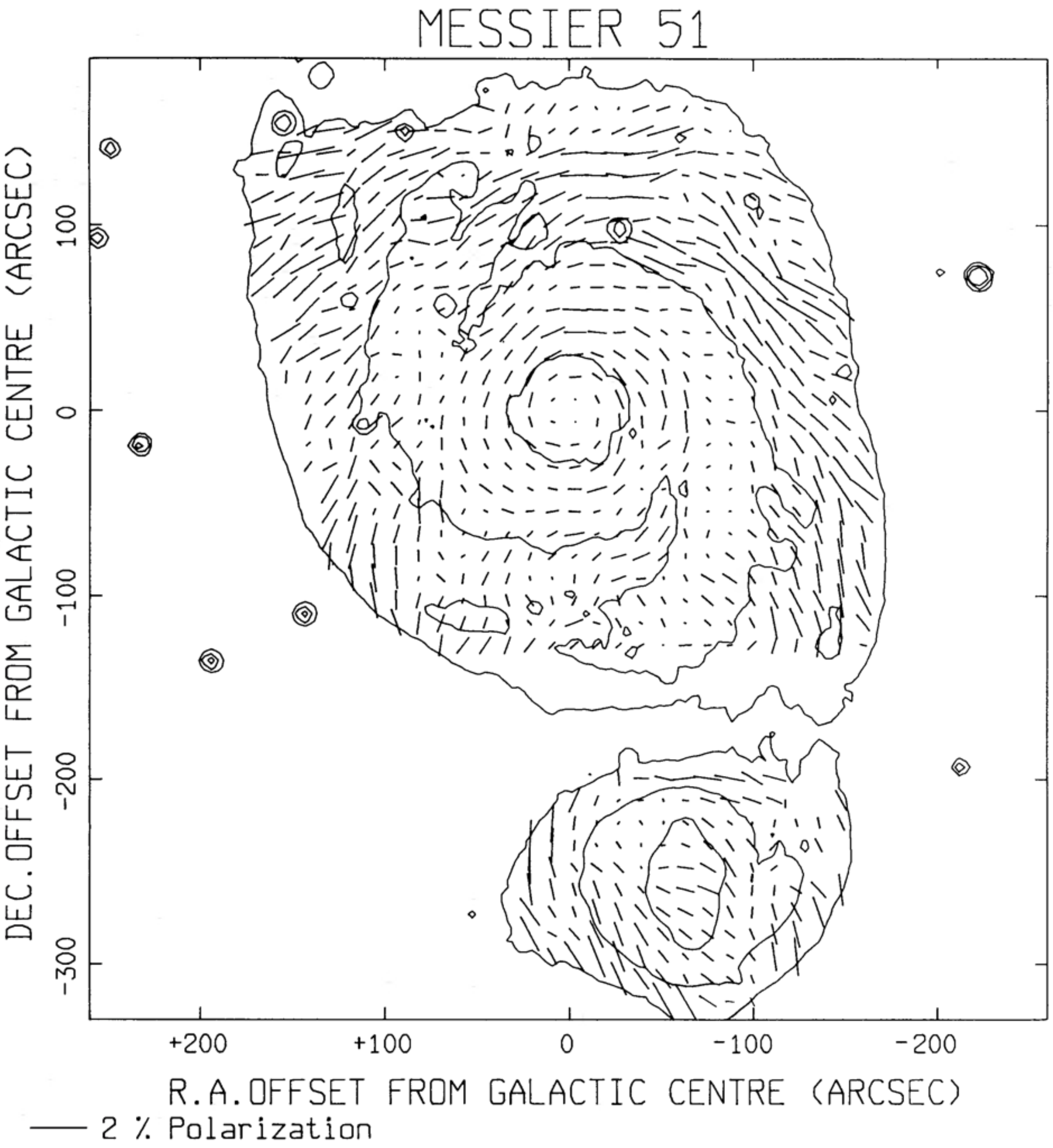

Figure 1.3: An optical linear polarization map of M51/NGC 5195. The integration bins are 18 arcsec square, spaced at 12 arcsec intervals. Figure taken from Scarrott et al. 1987.

field region. The temperature of the region must also be sufficiently low to compete with the Doppler broadening of those lines.

1.2.4 Radio synchrotron emission

Continuous radio emission from galaxies combines thermal and non-thermal components (synchrotron). At longer wavelengths, the thermal radiation is negligible and the synchrotron radiation is dominant. The first step in separating the thermal and non-thermal components is to use the spectral exponent ($I \propto \nu^{-\alpha}$) where I is the radiation intensity, ν is the frequency, and α is the spectral exponent. See appendix for details. The spectral exponent of non-thermal radiation, $\alpha \sim 0.8 - 1.0$, can be separated by assuming a spectral exponent of $\alpha \sim 0.1$ for thermal radiation in an optically thin layer. However, the synchrotron radiation intensity depends on the energy and age of the cosmic ray electrons. Cosmic ray electrons propagate from the spiral arms and lose energy due to inverse Compton scattering with synchrotron radiation and photons, so the synchrotron radiation spectrum is flatter in the spiral arms than in the inter-arm region, outer disk and halo. Additionally, there is a separation method [41] that uses a combination of Hα and 24 μm infrared images as a template for thermal radiation and subtracts it from the total radiation.

The energy density of total cosmic rays (protons are dominant) and the energy density of the total magnetic field are expected to be equally distributed. Since the energy density of cosmic rays is determined by integrating their energy spectrum, the total magnetic field intensity can be calculated from the synchrotron intensity [42]. The synchrotron intensity I_{syn} is proportional to the total field strength as $I_{syn} \propto B^{3+\alpha}$ and $B_{tot,\perp}$ is written by

$$B_{tot,\perp} \propto (I_{sys}(K_0 + 1)/L)^{1/(3+\alpha)}, \tag{1.2}$$

where α is the spectral index of the synchrotron ($I_{syn} \propto \nu^{-\alpha}$), L is the path length through the radiation source, and K_0 is the ratio of the number density of CR protons to electrons. $K_0 \sim 100$ is a reasonable assumption in star-forming regions of the disk [43]. For electron-positron plasmas, e.g., in jets of radio galaxies, $K_0 = 0$. The input parameters, in particular the path length L and the ratio K_0 , are not well constrained. There are several problems with the equipartition estimation. First, the equation 1.2.4 is only applicable to steeped spectra with $\alpha > 0.5$. For flat spectra, the integration over the energy spectrum of cosmic rays is restricted to a limited energy interval. Second, when the energy loss of cosmic-ray electrons is large, for example in the starburst region and in the spiral arms, the equipartition value is a lower limit and the strength of the magnetic field is underestimated. Since the energy loss of aging cosmic-ray electrons is much more severe than that of cosmic-ray protons, the ratio K becomes large. Using the standard value K_0, the total magnetic field in such regions is estimated by a factor of $(K/K_0)^{1/(3+\alpha)}$ [42]. Cosmic ray electrons need to propagate farther away from the place of generation, so the energy loss is higher. Hence, this problem can occur in the outer disks and haloes of galaxies. Third, it takes time for energy equipartition to take place, so it is not valid on small scales of time and space. Analysis of the radio continuum from the Milky Way and the nearby galaxy M33 shows that equipartition does not hold at scales smaller than about 1 kpc [44].

Rotation measure

Linear polarization Faraday rotation is a phenomenon in which the polarization angle rotates when a polarization wave passes through a magnetic fluid. If the polarization angle before the passage is χ, the polarization angle after the passage χ is proportional to the square of the wavelength λ and can be written as

$$\chi = \mathrm{RM}\lambda^2 + \chi_0, \tag{1.3}$$

where RM is called a Rotation Measure. The RM can be physically written as

$$\mathrm{RM} = 0.81 \int_{\infty}^{0} \left(\frac{n_e}{\mathrm{cm}^{-3}}\right) \left(\frac{B_{\parallel}}{\mu\mathrm{G}}\right) d\left(\frac{z}{\mathrm{pc}}\right) \mathrm{rad\,m^{-2}}, \tag{1.4}$$

where n_e is the free electron density, $B_{\parallel}$ is the component of the magnetic field parallel to the line of sight, and z is the line of sight distance. The integral is oriented toward the observer, and RM is positive if the magnetic field is oriented toward the observer. If χ is obtained from the polarization Stokes parameters Q and U, RM is obtained from the wavelength dependence of χ, and the free electron distribution is given in some way, the integral of the line-of-sight parallel component of the magnetic field can be found. See appendix A.1 for a detailed derivation of the Stokes parameters.

Recently, RM has been estimated using a technique called Faraday tomography [45, 46]. While RM gives the line-of-sight integral, Faraday tomography gives the line-of-sight distribution. See appendix A.4 for details. The expression for the linear polarized intensity $P(\lambda^2)$ can be written as

$$P(\lambda^2) = \int_{-\infty}^{\infty} F(\phi) e^{2i\phi\lambda^2} d\phi. \tag{1.5}$$

This $F(\phi)$ is called the Faraday Dispersion Function (FDF) or Faraday spectrum, and represents the polarized intensity distribution in ϕ space. ϕ is written as

$$\phi(r) = 0.81 \int_{r}^{0} n_e(r') B_{\parallel}(r') dr'. \tag{1.6}$$

It is a physical quantity similar to RM, but it is an integral up to position r, whereas RM is an integral from the observer to infinity. $\phi(r)$ is called the Faraday depth. Also, Equation A.60 is a Fourier transform with ϕ and λ^2 as conjugate variables. The inverse transformation can be written as

$$F(\phi) = \frac{1}{2\pi} \int_{-\infty}^{\infty} P(\lambda^2) e^{-2i\phi\lambda^2} d\phi. \tag{1.7}$$

We can estimate $F(\phi)$ from the observables $P(\lambda^2)$.

Depolarization

Depolarization is a mechanism by which an observer receives a weaker polarized emission than that emitted at the origin. It leads to a decrease in the polarization fraction since this mechanism does not affect the total intensity. Because depolarization is common in many astronomical cases, the properties of depolarization can be a useful tool for revealing the structure of the line of sight and the source itself. Analytical works have demonstrated various possible cases of depolarization [45, 47, 48, 49, 50]. Because the diffuse polarized emission of a DING is expected to be several orders of magnitude weaker than those of quasars and radio galaxies, we can safely neglect the polarized emission of the DING. Thus, the DING plays the role of Faraday screen and the external Faraday dispersion depolarization or the beam depolarization emerges [48].

Faraday screen consists of magnetized plasma that causes Faraday rotation. If there are only coherent magnetic fields and a constant RM structure in this Faraday screen, the emission of the background source experiences the same amount of Faraday rotation and the screen does not cause any depolarization. On the other hand, if the emission experiences different amounts of Faraday rotation at different positions, cancellation of the linear polarization can take place. This is the beam depolarization and is considered to be the primary mechanism of depolarization. Depolarization is thus more likely to occur when there is a RM gradient and/or there are turbulent magnetic fields within an observing radio beam (see, e.g., [48]).

In the case of the beam depolarization, the effect of depolarization is greater at longer wavelengths in general, because the effect of Faraday rotation is stronger at longer wavelengths. If the relationship between the total intensity $I(\nu) \propto \nu^{\alpha_I}$ and the linearly-polarized intensity $P(\nu) \propto \nu^{\alpha_P}$ holds, the most general expression for depolarization can be expressed as follows;

$$p = P/I \propto \nu^{\alpha_P - \alpha_I} = \nu^{\beta}, \tag{1.8}$$

where p is the polarization fraction, ν is the observed frequency, α_I is the total intensity spectral index, α_P is the polarization spectral index, and $\beta = \alpha_P - \alpha_I$. In reality, the emission of the background source is considered to be non-uniform and depolarized by itself. We will address these effects in future work.

The polarization that passes through regions of large RM tends to be more depolarized than that passes through regions of small RM, so that the polarization fraction is biased and the observed RM tends to be smaller than the average of intrinsic values within the beam. Furthermore, an observed RM is always smaller than the intrinsic value by $1/(1+z)^2$, where z is the redshift at which Faraday rotation happens because the rotation takes place at a higher rest-frame frequency.

The following are some examples of depolarization.

(1) Wavelength independent depolarization: This occurs when the magnetic field causing synchrotron polarization is non-uniform. Polarization is emitted with different polarization angles for each line of sight in the beam to be observed and reaches the observer, so that polarization cancellation can occur in the beam.

(2) Differential Faraday rotation depolarization: This occurs when cosmic ray electrons emitting synchrotron polarization and thermal electrons causing Faraday rotation coexist. Even if the far-field polarization and the near-field polarization are emitted at the same polarization angle in the line of sight, they reach the observer with different Faraday rotations, so that polarization cancellation can occur.

(3) Beam depolarization: Occurs when there is structure in the RM within the beam being observed. Even if the polarization waves in the beam are emitted at the same polarization angle, they reach the observer with different Faraday rotations for each line of sight in the beam, which can cause polarization cancellations.

1.3 Dynamo theory

The evolution and maintenance of magnetic fields are generally explained by dynamo theory, which converts kinetic energy into magnetic energy. Turbulence is common in astrophysics and is maintained by physical mechanisms that occur in interstellar convection, supernova explosions, and mergers within galaxy clusters. The dynamo process uses the kinetic energy of this turbulence to amplify an initially weak seed magnetic field.

The magnetic fields in these systems can be classified into two types based on scale. One is a large-scale or mean magnetic field that is consistent over scales comparable to the size of the system, and the other is a small-scale or fluctuating field. The length of the small-scale magnetic field is on the order of the driving scale of the turbulence. Both types of magnetic fields are equally important to ISM dynamics, since the root-mean-square (rms) magnitudes of both fields are usually comparable in the case of galaxies. Dynamos fall into two categories for producing each type of magnetic field: mean-field (or large-scale) dynamos and fluctuating (or small-scale) dynamos.

1.3.1 Mean-field dynamos

The most promising mechanism to sustain magnetic fields and generate large regular magnetic fields from the turbulent fields of the interstellar material in galaxies is the $\alpha - \Omega$ dynamo. It is based on differential rotation (Ω), expanding gas flows driven by supernova explosions [9, 22] or cosmic rays [51], and describes the Coriolis force (α effect) and the magnetic diffusivity (η) driven by turbulence. The "mean-field" approximation of the $\alpha - \Omega$ dynamo equation allows for an analytical solution by mathematically separating the large and small parts of the velocity and magnetic fields. The mean-field dynamo equation for the regular field $\mathbf{B}$ is

$$\frac{\partial \mathbf{B}}{\partial t} = \boldsymbol{\nabla} \times (\mathbf{u} \times \mathbf{B}) + \boldsymbol{\nabla} \times \alpha \mathbf{B} + \eta \nabla^2 \mathbf{B}. \tag{1.9}$$

Since magnetic fields do not diverge, they can be decomposed into toroidal and poloidal components. The mean-field dynamo is the process by which the toroidal and poloidal components of a magnetic field are mutually generated.

Using a cylindrical coordinate system, assume that the velocity field of the galactic gas disk is $(0, V(r), 0)$. Considering the axisymmetric case for simplicity, the equations describing the time evolution of each component of the magnetic field are as follows

$$\frac{1}{\eta}\frac{\partial B_r}{\partial t} - \left(\frac{\partial^2 B_r}{\partial r^2} + \frac{\partial^2 B_r}{\partial z^2} - \frac{V}{\eta r}\frac{\partial B_r}{\partial \phi} - \frac{\alpha}{\eta}\frac{\partial B_\phi}{\partial z}\right) = 0, \tag{1.10}$$

$$\frac{1}{\eta}\frac{\partial B_\phi}{\partial t} - \left[\frac{\partial^2 B_\phi}{\partial r^2} + \frac{\partial^2 B_\phi}{\partial z^2} - \frac{V}{\eta r}\frac{\partial B_\phi}{\partial \phi} + \frac{1}{\eta}\left(\frac{\partial V}{\partial r} - \frac{V}{r}\right) B_r\right] = 0, \tag{1.11}$$

$$\frac{1}{\eta}\frac{\partial B_z}{\partial t} - \left(\frac{\partial^2 B_z}{\partial r^2} + \frac{\partial^2 B_z}{\partial z^2} - \frac{V}{\eta r}\frac{\partial B_z}{\partial \phi} + \frac{\alpha}{\eta}\frac{\partial B_\phi}{\partial z}\right) = 0. \tag{1.12}$$

The term containing $(dV/dr - 1/r) = r d\Omega/dr$ represents the Ω effect, which produces an azimuthal magnetic field from a radial magnetic field due to the difference in radial rotational angular velocity (differential rotation). In the equations for the radial and vertical components, the term including α generates the radial and vertical magnetic fields from the azimuthal magnetic field.

Various criticisms have been made of mean-field galaxy dynamo theory in its current form. Of particular importance are the poorly understood nonlinear geometry and physics of turbulent diffusion, uncertainties in the explanation of flux removal from the disk, the effect of the multiphase structure of the ISM on the magnetic field, and its effect on the magnetic field. strong fluctuating magnetic fields that grow rapidly above the mean magnetic field [52, 53]. Most of the uncertainties are related to the α effect since the role of the Ω effect is physically and mathematically simple. One possible mechanism is the Parker instability. The Parker instability is a magnetic instability that grows when the buoyancy force acting on the lighter part of the magnetic fluid as it falls along the magnetic field lines exceeds the magnetic tension, and perturbations with a long wavelength of about 10 times or more the thickness of the disk grow. When the Parker instability grows in a disk with an initially azimuthal horizontal magnetic field, a magnetic loop emerges and a vertical magnetic field is generated from the azimuthal magnetic field. In a coordinate system rotating with the disk, the Coriolis force acting on the falling flow along the magnetic field lines twists the magnetic loop and generates a radial magnetic field. Other mechanisms in galactic gas disks include the generation of radial and vertical magnetic fields from azimuthal magnetic fields caused by supernova explosions. Although the equation of evolution of the mean magnetic field does not include the Parker instability and the velocity field generated by supernova explosions, their effects on the mean magnetic field are approximated by a term including α. Another important contribution to the large-scale magnetic field may be due to magneto-rotational instability (MRI), a local shear instability that occurs in weakly magnetized differential rotating disks [54]. Originally, MRI is cosidered to explain the loss of angular momentum in accretion disks. It generates turbulence and amplifies the magnetic fields. The appearance of large magnetic fields with this instability has been confirmed by numerical simulations [55, 56].

1.3.2 Small-scale dynamos

The existence of small-scale dynamos is fundamentally important to the evolution of the galaxy's magnetic field. Without the small-scale dynamo, the seed fields of primordial galaxies would be much weaker and it would take much longer to generate a large-scale normal field. Small-scale dynamos amplify the magnetic field on scales smaller than the driving scale of turbulence due to random stretching and contraction of magnetic field lines caused by turbulent velocities [57]. Fluctuation dynamos work on faster time scales, aligned with turbulent eddy turnover time, contrasting with the time scales of large-scale dynamos decided by rotation or turbulent diffusion [58]. The fluctuation dynamo rapidly amplifies an initial weak seed magnetic field, reaches saturation, and subsequently serves as the seed for the mean-field dynamo. The mean-field dynamo then controls the field over the size of the system.

1.4 Theoretical models of galactic magnetic fields

The global magnetic field structure of disk galaxies has a variety of configurations. For example, the magnetic field is ring-shaped or axisymmetric (ASS; the magnetic field has an apparent non-zero divergence) or bisymmetric spiral (BSS). The composition of the magnetic field in a disk galaxy can be determined by Faraday rotation observations. In this method, the value of RM (or polarization angle χ) is plotted as a function of azimuthal angle θ. where θ is the azimuthal angle along the circle on the plane of the galactic disk at a fixed radius. If the magnetic field of the galactic disk is a ring or ASS, the RM shows a single sinusoidal variation as a function of θ. In the case of BSS, RM is a double-peaked sinusoidal wave along the circle. A simpler analysis can be obtained by measuring the RM or χ relationship along the long axis. In the case of a ring or ASS field, the variation is asymmetric with respect to the galactic center. On the other hand, the BSS variation is symmetric. There are many galaxies for which the field configuration has been determined. Examples of intrinsic magnetic fields in galaxies include IC342, M31, and the Milky Way. Examples of possible BSS magnetic fields in galaxies are M81, M33, and M51.

ASS is produced by the winding of a vertical component. The twisted vertical magnetic field bends toward the galactic disk, creating a spiral structure. The direction of the helically twisted magnetic field is consistently outward on one side of the disk and inward on the other side, forming the ASS configuration. The figure shows the numerical results of magnetohydrodynamic (MHD) simulations of the ASS field formation.

Large-scale BSS configurations of the galactic magnetic field cannot be produced by the dynamo mechanism. BSS is believed to have been created during the formation of protogalaxies. Based on this primordial origin hypothesis, BSS is interpreted as fossils of intergalactic fields that were entrained during the formation and contraction of protogalactic disks. It should also be noted that the BSS is $\nabla \mathbf{B} \neq 0$.

Magnetic fields models of Milky Way galaxy

The Milky Way galaxy has been the subject of various radio observations. Models can be constrained from all-sky observations of synchrotron radiation total intensity, linear polarization, and RM, and analytical models exist. The magnetic fields (ASS and BSS) can be written in the cylindrical coordinate system as (following the equation in Sun et al. (2008) [59]),

$$\begin{cases} B_R(R,\Theta,z) &= D_1(R,z)D_2(R,\Theta)\sin p \\ B_\Theta(R,\Theta,z) &= -D_1(R,z)D_2(R,\Theta)\cos p \\ B_z(R,\Theta,z) &= 0, \end{cases} \tag{1.13}$$

where p is the pitch angle of arms in a Milky-way like galaxy, and

$$D_1(R,z) = \begin{cases} B_0 \exp\left\{\left(-\frac{R-R_\odot}{R_0} - \frac{|z|}{z_0}\right)\right\}, & R > R_c, \\ B_c \exp\left\{\left(-\frac{|z|}{z_0}\right)\right\}, & R \leq R_c. \end{cases} \tag{1.14}$$

We adopt the ASS+RING model for the ASS model, and the magnetic field reversals are written in the following way;

$$D_2(R,\Theta) = \begin{cases} +1, & R > 7.5 \text{ kpc}, \\ -1, & 6 < R \leq 7.5 \text{ kpc}, \\ +1, & 5 < R \leq 6 \text{ kpc}, \\ -1, & R \leq 5 \text{ kpc}, \end{cases} \tag{1.15}$$

where $+1$ means the clockwise direction as seen from the north pole. We adopt $R_0 = 10$ kpc, $z_0 = 1$ kpc,$R_c = 5$ kpc, $B_0 = 2$ μG, $B_c = 2$ μG, and $p = -12^\circ$. For BSS model, D_2 is written in the following way;

$$D_2(R,\Theta) = \sin\left(\Theta + \frac{1}{\tan p} + \ln\frac{R}{R_{\rm sb}}\right). \tag{1.16}$$

We adopt $R_0 = 6$ kpc, $z_0 = 1$ kpc,$R_c = 3$ kpc, $B_0 = 2$ μG and $B_c = 2$ μG. We also set $R_{\rm sb} = 9$ kpc and $p = -10^\circ$ for $R > 6$ kpc, and otherwise $R_{\rm sb} = 6$ kpc and $p = -15^\circ$. The all-sky RM maps suggest that milky-way galaxy has the existence of halo toroidal fields because we observe reverse RM structure across the galactic plane and across the galactic center (e.g.,[60]). The halo toroidal field is written in the following way [61]:

$$\begin{cases} B_{tR}(R,\Theta,z) & = 0 \\ B_{t\Theta}(R,\Theta,z) & = B_{t0}\frac{\mathrm{sign}(z)^{v}}{1+\left(\frac{|z|-z_{t0}}{z_{t1}}\right)^{2}}\frac{R}{R_{t0}}\exp\left\{\left(-\frac{R-R_{t0}}{R_{t0}}\right)\right\} \\ B_{tz}(R,\Theta,z) & = 0, \end{cases} \tag{1.17}$$

where sign(z) is the sign of z, the v is the parity of the toroidal field configuration. If we consider the asymmetric configuration in longitude and latitude relative to the Galactic plane and centre and the axisymmetric configuration without reversals relative to the Galactic plane, we adopt $v = 1$ and $v = 2$, respectively.The parameters are $B_{t0} = 2\mu$G, $R_{t0} = 4$kpc, $z_{t0} = 1.5$kpc, and $z_{t1} = 0.2$kpc for $|z| < z_{t0}$ and otherwise $z_{t1} = 4$kpc. The paramerters are based on Sun et al. (2010) [62].

1.5 Evolution of galactic magnetic fields

Typical models of the global magnetic field structure of spiral galaxies include the ring model, the ASS (Axy-Symmetric Spiral) model, and the BSS (Bi-Symmetric Spiral) model. Due to the lack of sensitivity in radio emission, few observations of extragalactic galaxies with redshift $z > 0.1$ have been achieved. Using the Faraday rotation and depolarization, the investigation of intervening galaxies that behave as absorption line systems has recently been progressing. One of the possible, less-biased ways to study galactic magnetic fields is to investigate the depolarizing intervening galaxies (hereafter, DINGs). There are a lot of external galaxies in intergalactic space so that the galaxies can intervene in the emission from background astronomical objects such as quasars and radio galaxies. Indeed, 40,429 out of 84,533 SDSS quasars are known to accompany Mg II absorber systems in front of the quasars [63]. Such absorber systems are likely DINGs, whose magnetic fields can depolarize background polarized emission and can contribute to Faraday rotation measure (RM). This overlap happens randomly in space, reducing the selection bias. The correlation between polarization properties and the existence of Mg II absorber systems has been reported in the literature [64, 65, 66, 67, 68]. Figure 1.4 shows cumulative distributions of RM of sightlines with and without strong MgII absorption line systems. It can be seen that the RM tends to be larger when the DING is in the line of sight. Large surveys of extragalactic sources with the Square Kilometre Array (SKA) (e.g., [69]) and its precursors/pathfinders will dramatically increase the number of extragalactic polarized sources, allowing us to improve previous statistical works for DINGs.

Recently, observations of background polarization sources using gravitational lensing effects of objects at $z = 0.439$ detected that galaxies at $z = 0.439$ also have ordered magnetic fields [1]. They used a method to determine the magnetic field from the difference in RMs of background source emissions passing through different positions of the lens galaxy due to the gravitational lensing effect of the lens galaxy. The difference

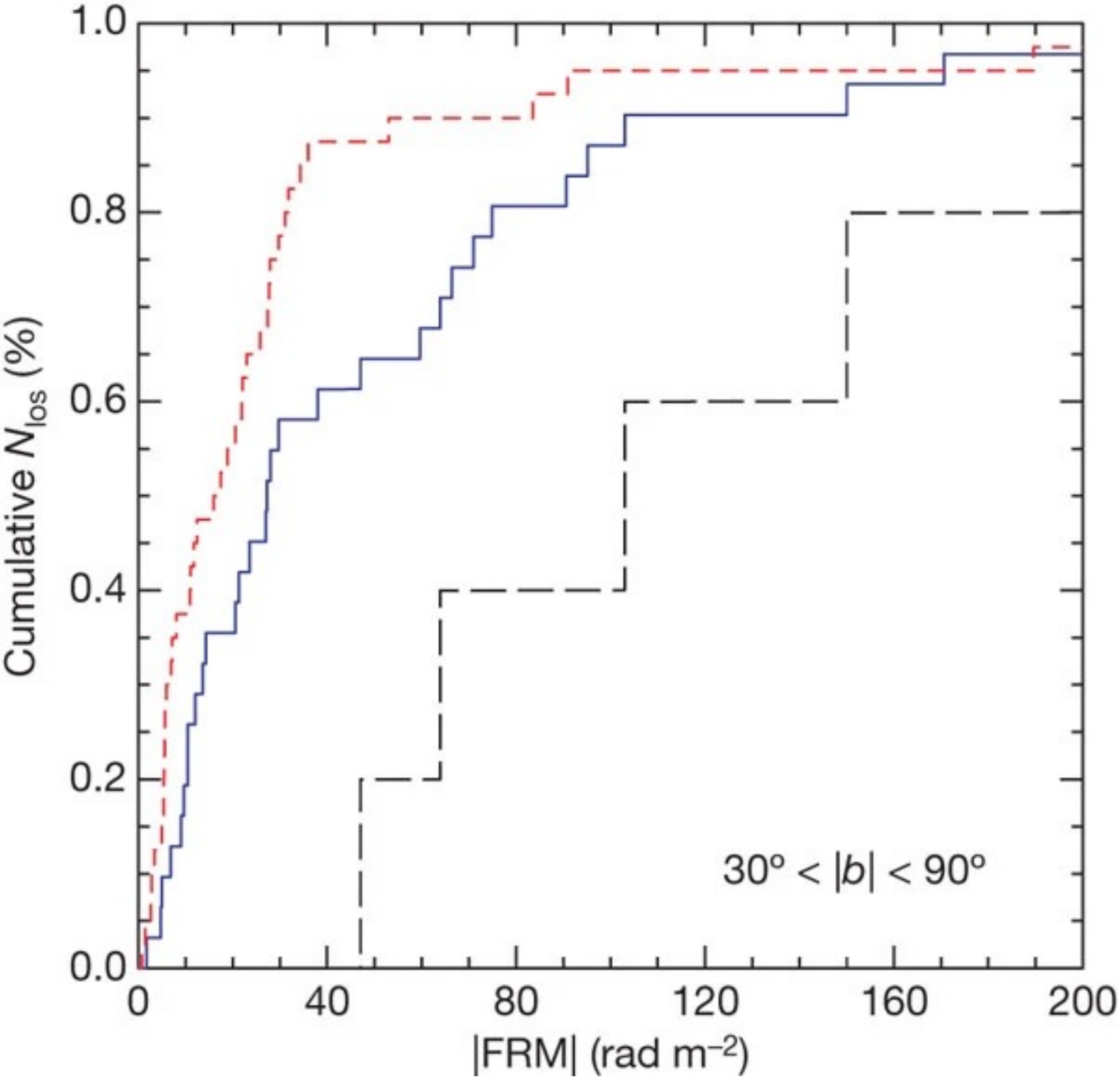

Figure 1.4: Cumulative distributions of Rotation Measures of sightlines with and without strong MgII absorption line systems. Figure taken from Bernet et al. (2008) [65].

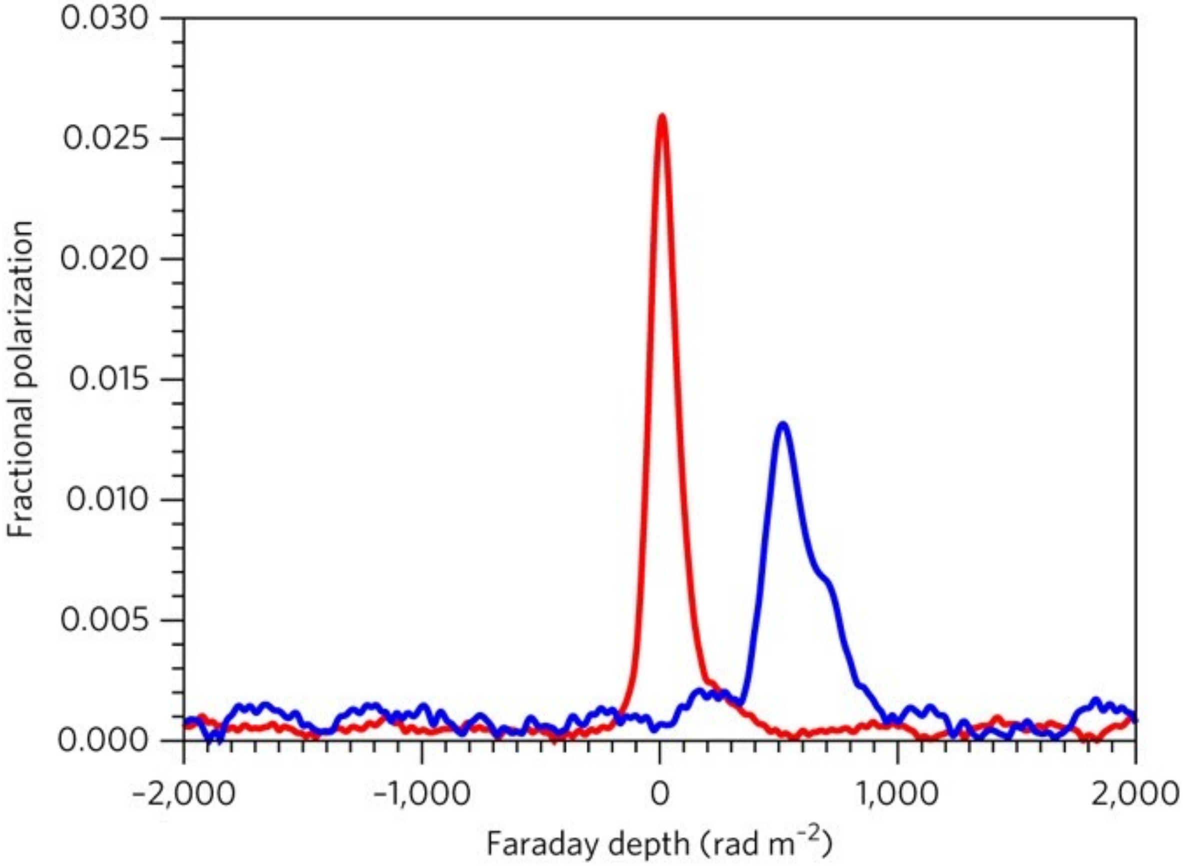

Figure 1.5: Faraday depth spectra of two gravitationally lensed images (blue and red) with lensing galaxy at a redshift of 0.439. Figure taken from Mao et al. (2017) [1].

between the means of the two components (the difference in RM between the two images) gives an estimate of the large-scale magnetic field in the lensing galaxy (see Figure 1.5). The difference in the standard deviations of the two components (difference in the standard deviations of the RM) gives information about the small-scale magnetic field. In the Square Kilometer Array (SKA) era, it is expected to find 10^5 polarization sources subject to gravitational lensing effects [70]. All-sky polarization surveys using the SKA predecessor have now begun.

It is expected that the small-scale magnetic field is genarated quickly by turbulence [71], while the global magnetic field is constructed over a long time (about the rotational period of a disk) [72]. According to numerical experiments [73], if a kpc-scale magnetic field of μG intensity is generated in a galactic disk at $z = 2$, it will take up to $z = 0.5$ for it to grow into a galaxy-scale aligned magnetic field. During this period, especially from redshift $z = 2$ to the present, when star formation was active, the effect of star formation will also be important to verify by direct observation by providing the SKA with a large light gathering power and observing even the high distant galaxies.

Faraday rotation and polarization resolution can also be discussed in more detail by increasing the number of background detectable polarization sources. Plasma density is expected to be explored through synchrotron polarization of galaxies, Faraday rotation and polarization resolution, and the Zeeman effect.

1.6 Aim of the thesis

We should know when a galaxy has a coherent magnetic field and how much the strength of it is. The Milky Way and nearby galaxies have been observed to have coherent magnetic fields and turbulent magnetic fields. Galactic magnetic fields affect star formation in galaxies and galactic evolution through the formation of interstellar gas clouds and the propagation of cosmic rays. Observations of the magnetic fields in distant galaxies are necessary to understand how the galactic magnetic field evolves and to put limits on theories of the evolution of galactic magnetic fields. One method to study the magnetic fields in distant galaxies is to observe intervening galaxies. The magnetic fields of intervening galaxies will be extracted from the observational data for the back ground source such as quasars, when the next-generation radio interferometer, the Square Kilometre Array (SKA), is going to be active in the late 2020s. Therefore, we will investigate the possibility of using the SKA predecessor to get information on the magnetic fields of the intervening galaxies using two different methods.

The first is to reveal how the magnetic field of an intervening galaxy affects the observed RM when there is an intervening galaxy in the line of sight. The major issues in chapter 2 are to determine if the characteristic magnetic field information (RM) of DING can be retrieved by examining the depolarization spectrum and FDF, and to determine on what effects the bias depends in a large survey of polarization sources. In addition, we will investigate their statistical importance for future large surveys of RM, and determine what redshift dependence there is on RM and which parameters of DING have a large effect.

The second is to determine how the RM structure behaves when the background polarization source is subjected to gravitational lensing effects. The Polarization All-Sky Survey (POSSUM) with the Australian SKA Pathfinder (ASKAP) has begun, and it is expected to detect polarization sources subject to gravitational lensing effects. However, POSSUM will not be able to spatially resolve gravitational lensing sources. Therefore, it is necessary to examine whether it is possible to extract the RM structure of lensing galaxies from lensing polarization sources that are not spatially resolved. The major issue in chapter 3 is whether it is possible to separate information about the RMs of intervening galaxies and background sources in cases where they are not spatially resolved.

In chapter 2, we show the depolarization spectra and FDFs caused by DING with various physical parameters. We show how the RM of DING can be estimated from the depolarization spectra and FDFs, and which parameters they depend on. In addition, we will investigate their statistical importance in future large surveys of RM and determine what redshift dependence of RM there is and which parameters of DING have a large effect. In chapter 3, we will investigate whether it is possible to extract the RM structure of lensing galaxies using QU-fitting when the background polarization source is subject to gravitational lensing and the polarization is observed.

Chapter 2

Effects of Depolarizing Intervening Galaxies on Background Radio Emission

2.1 Introduction

Various simple models have been used and many studies have been done to understand DING. (e.g., [45, 48]) and galaxy models (e.g., [66, 74, 75]). However, the redshift dependence of depolarization caused by a DING is not systematically addressed, remaining statistical contribution of DINGs in RM catalogs unclear. In addition, while modern radio polarimetry adopts Faraday tomography to estimate RM (e.g., [76, 77], [78]), DING's effects on Faraday dispersion function (FDF) is not paid much attention [79]. Clarification of DING's effects is crucial for exploring galactic [59, 80, 81, 82, 83] and intergalactic [84, 85, 86, 87, 88] magnetic fields with future large surveys.

In this paper, we show depolarized spectra and FDFs caused by the DINGs with various physical parameters and explore their statistical significance for large surveys of RM in the future, using theoretical DING models. The paper is organized as follows. We briefly summarize the nature of depolarization in Section 1.2.4 and describe our model and calculation in Section 2.2. We find that, while multiple galactic structures result in complicated depolarization features, the essence is made by the global disk magnetic field which is the primary component of galactic RM. Based on this fact, we show the results for the simplest, ring magnetic field in the galactic disk to clarify how DING's depolarization takes place in Section 2.3. Other galactic components, such as the disk spiral, the halo, and turbulent magnetic fields, are added in our discussion (Section 2.4). We also discuss systematic errors in estimating DING's RM mean and dispersion by the FDF peak and Burn's depolarization law, respectively. Finally, we discuss the redshift dependence of the DING's RM dispersion and a future prospect to study the intergalactic magnetic field. We summarize this work in Section 2.5.

2.2 Model and calculation

In this section, we describe our model and calculation. When we refer the angular size, we adopt a ΛCDM cosmology with $\Omega_{\rm m0} = 0.27$ and $\Omega_{\Lambda 0} = 0.73$, and $\mathrm{H}_0 = 70\,\mathrm{km\,s^{-1}Mpc^{-1}}$ in this paper. One arcsecond ($1''$) corresponds to 1.8, 6.2, and 8.2 kpc for redshifts of $z = 0.1$, 0.5, and 1.0, respectively.

2.2.1 Numerical models

We consider observing a radio lobe as a background polarized source behind a DING. We only consider RM of the DING and ignore any other RMs such as RMs of a background source and the Milky Way Galaxy; those are beyond the scope of this paper. Although a background radio source likely has inhomogeneous morphology, we assume that the source has uniform emission and a circular shape with $1''$ in diameter to focus on the effect of the DING.

We define the Stokes parameters, $I(\nu)$, $Q(\nu)$, $U(\nu)$, $V(\nu)$, and the polarized intensity, $P(\nu) = Q(\nu) + jU(\nu)$, of a background source as

$$I(\nu) = I_0 \nu^{\alpha_I}, \tag{2.1}$$

$$P(\nu) = P_0 \nu^{\alpha_P} = p(\nu) I(\nu) e^{2j\chi_0}, \tag{2.2}$$

where χ_0 is the intrinsic polarization angle, j is the imaginary unit, and we consider no circular polarization, i.e. $V(\nu) = 0$. For the intrinsic emission of the background source, we adopt the simplest parameters; $\alpha_I = \alpha_P = -1$ and $p_0 = P_0/I_0 = 1$. The choice of the parameters is useful to visualize depolarization effects of our interest in this paper, and does not affect our conclusion of depolarization effects caused by a DING.

DINGs are external galaxies that are dark in any observing frequency but are depolarizing background polarization. We consider a low surface brightness, disk galaxy as a DING since the field sky dominates a large survey volume. Magnetic fields in disk galaxies have been investigated in the literature (e.g., [59, 89, 90, 91]). They consist of global, regular components and local, turbulent components, where we only consider the former component as stated in Section 2.1.

We adopt the RING model as a global regular magnetic field of a DING (e.g., [92]). The ring-shape magnetic field can be written in the cylindrical coordinate system (R, ϕ, z') as

$$\left\{ \begin{array}{l} B_R = 0, \\ B_\phi = B_0 \ (0 \text{ kpc} \leq R \leq 10 \text{ kpc}), \\ B_{z'} = 0, \end{array} \right. \tag{2.3}$$

where we adopt the disk scale height of 1 kpc and the strength of $B_0 = 5\ \mu$G;

$$B_0 = \left\{ \begin{array}{l} 5 \ (-1 \text{ kpc} \leq z' \leq 1 \text{ kpc}), \\ 0 \ (z' < -1 \text{ kpc}, 1 \text{ kpc} < z'). \end{array} \right. \tag{2.4}$$

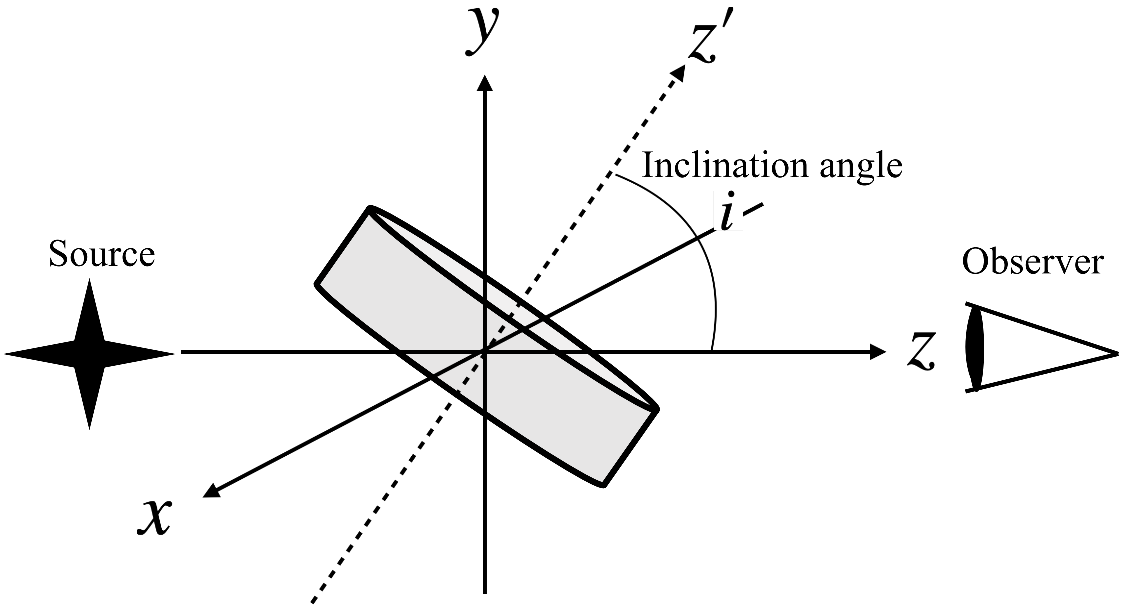

Figure 2.1: Schematic picture of the coordinates for observation.

The global electron distribution is assumed to be uniform with the density of $n_{\rm e} = 0.01$ cm^{-3}. This assumption is reasonable while we consider the disk component up to the scale height of the disk. We do not consider synchrotron emission from cosmic-rays in the DING because it is negligibly weak by the definition of the DING. For the study of FDF of diffuse polarized emission from external galaxies, see e.g., Eguchi et al. (2020) [93] and references therein.

Figure 2.1 depicts the definition of the Cartesian coordinates in this work. We set the z-axis becomes the direction of the sightline and the remaining x-axis and y-axis are on the projection screen perpendicular to the z-axis. The vertical direction from the disk mid-plane is z'-axis and we define the inclination angle, i, as the angle from the z-axis to the z'-axis, where $i = 0^\circ$ is the face-on view and $i = 90^\circ$ is the edge-on view. We place a DING at a redshift, z, from 0.1 to 1.0. Nearby DINGs with $z < 0.1$ are not considered because nearby galaxies are likely visible in optical and IR bands and those galaxies are no longer DING.

2.2.2 Observing specification and calculation

As described above, we assume that the background source has diffuse, uniform emission of a circular beam with a $1''$ diameter. The beam passes through the DING, experiencing Faraday rotation by the RM of the DING (see Figure 2.2). This effect is calculated as follows. The DING is produced in a cubic box consisting of $200 \times 200 \times 200$ computational grids. The grid size, which determines the spatial resolution of the calculation, is 100 pc which is sufficiently smaller than the curvature scale ($\sim$kpc) of the

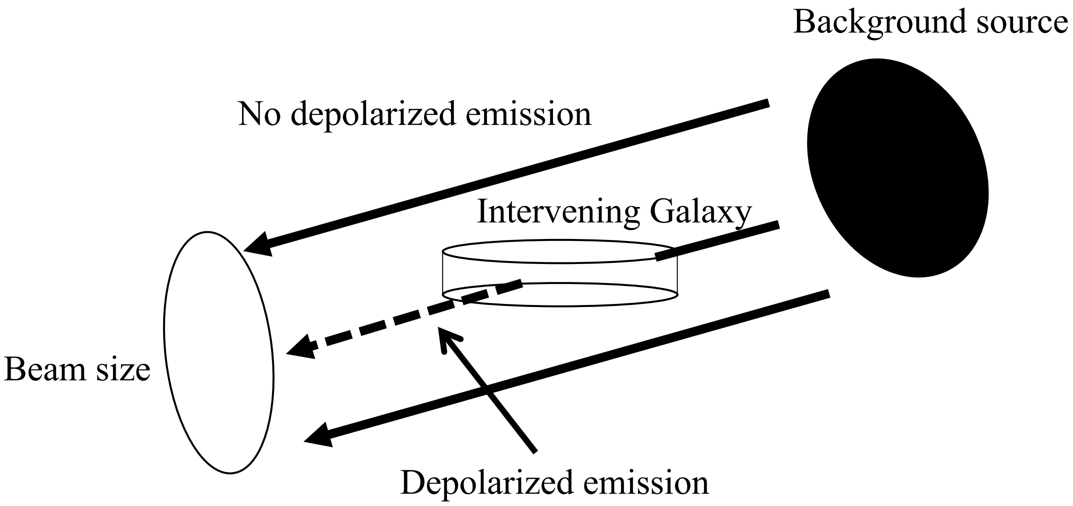

Figure 2.2: A schematic picture of observed polarized emission in situation of right panel of figure 2.4

disk magnetic field. The RM and Faraday rotation within the k-th grid along a certain line of sight are given by

$$\begin{cases} \Delta \mathrm{RM}_k = 0.81 n_e B_{k,\parallel} \Delta l \\ \Delta\chi = \mathrm{RM}_k \lambda^2 \Delta l \end{cases} \tag{2.5}$$

where $B_{k,\parallel}$ is the magnetic field parallel to the line of sight, $\Delta l = 100$ pc is the line element, and $\Delta\chi$ is the Faraday rotation of the polarization angle. We integrate RM and Faraday rotation along the z-axis and project the cumulative RM and Faraday rotation on the x-y plane as follows.

$$\begin{cases} \mathrm{RM} = \sum_{k=1}^{N} \Delta \mathrm{RM}_k \\ \chi = \chi_0 + \mathrm{RM}\lambda^2 \\ Q = Q_0 \cos\chi - U_0 \sin\chi \\ U = Q_0 \sin\chi + U_0 \cos\chi. \end{cases} \tag{2.6}$$

We sum up Q (or U) for the projected grids within the beam and obtain the observed Q (or U) within the beam. The observed polarization fraction, p, is calculated by using the observed Q and U as $p = \sqrt{Q^2 + U^2}/I$. The observed polarization fraction is written as $p \propto \nu^{\alpha_I - \alpha_P} = \nu^{\beta}$, so β will change if the depolarization takes place. We perform the least-square-fits for the p-ν relation using the power-law form to estimate β.

Figure 2.3 shows the distributions of rest-frame intrinsic RM of the DING for the inclination angle $i = 30°$. We define the beam offset parameters from the center of the

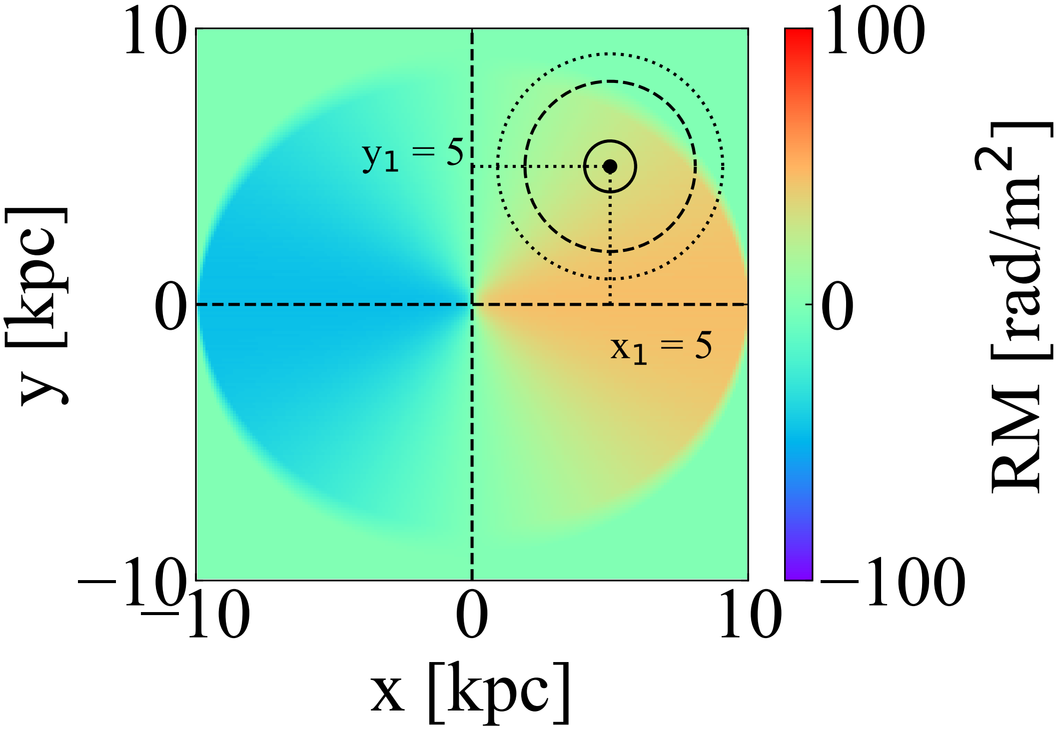

Figure 2.3: Example of the rest-frame intrinsic RM of a DING with inclination angle $i = 30°$. The solid, dashed, and dotted circles display the references of a $1''$ beam for $z = 0.1$, 0.5 and 1.0, respectively, centered at $x_1 = 5$ kpc and $y_1 = 5$ kpc.

DING, 10 kpc $\leq x_1 \leq$ 10 kpc in x-axis and 10 kpc $\leq y_1 \leq$ 10 kpc in y-axis. The solid, dashed, and dotted circles display the references of a $1''$ beam for $z = 0.1$, 0.5 and 1.0, respectively, centered at $x_1 = 5$ kpc and $y_1 = 5$ kpc.

In addition to the numerical integration of RM, we derive the observed RM, $\mathrm{RM}_{\mathrm{peak}}$, using Faraday RM synthesis (or Faraday Tomography; [45, 46]). We define $\mathrm{RM}_{\mathrm{peak}}$ as the Faraday depth at which the amplitude of the cleaned Faraday dispersion function (FDF) is maximum, where the RM CLEAN, a technique that removes the side lobes of the dirty FDF, is used [94]. Such a way of RM measurement will be considered in future large surveys of extragalactic RMs such as the SKA. We prepare the sufficiently-large number of frequency channels so as to avoid numerical errors regarding a lack of channels. Hence, in the Fourier transform for Faraday tomography we use the data with the sufficiently-large number of λ^2 channels, ensuring an ideal rotation measure spread function (RMSF). Any effects caused by coarse and/or unevenly-sampled data for Faraday tomography is beyond the scope of this paper, although the effects can be

Table 2.1: Frequency coverage and FWHM in this work.

Band	Frequency [MHz]	FWHM [rad/m^2]
Low	150 – 700	0.9098
Mid	700 – 1800	22.81
High	1800 – 4000	162.5

†The frequency bin is sufficiently narrow to minimize the resolution dependence.

crucial in actual observational work [95, 96]. The Frequency coverage and the corresponding full width at half maximum (FWHM) of the RMSF, i.e. the resolution of Faraday depth, is listed in table 2.1.

We also estimate the RM using the classical $\chi-\lambda^2$ relation (see equation 2.6), $\mathrm{RM_{cls}}$, and compare it with $\mathrm{RM_{peak}}$. Because the $\chi-\lambda^2$ relation does not follow a linear relation because of depolarization (e.g., [48]), it is in general difficult to derive $\mathrm{RM_{cls}}$ from such a polarization spectrum. We attempt to derive $\mathrm{RM_{cls}}$ using $\chi-\lambda^2$ relation at the relatively-high frequency, 3000 – 4000 MHz, at which we see a nearly-linear relation for our simulations.

We perform Monte-Carlo simulations and investigate the statistical contribution of DINGs on background polarization. We set the beam offsets, x_1 and y_1, and each inclination angle from 0 degrees to 90 degrees with a 5-degree step as the free parameters of Monte-Carlo simulations and calculate the FDF for each redshift of 0.1, 0.3, 0.5, 0.75, and 1.0. We performed 100,000 realizations for each redshift. The convergence of the results was confirmed from the runs with different realization numbers. We adopt $\mathrm{RM_{peak}}$ as the observed RM for each background source and measure the DING's RM from the shift of the $\mathrm{RM_{peak}}$ from zero because we do not consider any other RM contribution in the simulation. We consider the 700-1800 MHz band for Faraday tomography but $\mathrm{RM_{peak}}$ does not significantly depend on the frequency coverage (see discussion).

2.3 Results

2.3.1 Depolarization caused by a DING

Figure 2.4 shows the frequency dependence of the polarization fraction for a different inclination angle and a different beam offset. The left and right panels show the results with $(z, x_1, y_1) = (1.0, 5, 0)$ and $(z, x_1, y_1) = (1.0, 5, 3)$, respectively, and the top to bottom panels show the results for the inclination angles of 30°, 60°, and 90°, respectively. The insets show the RM maps, where the black circles indicate the $1''$ beam. The average and the standard deviation of RM within the beam are summarized in table 2.2. They monotonically increase with increasing the inclination angle and decrease with

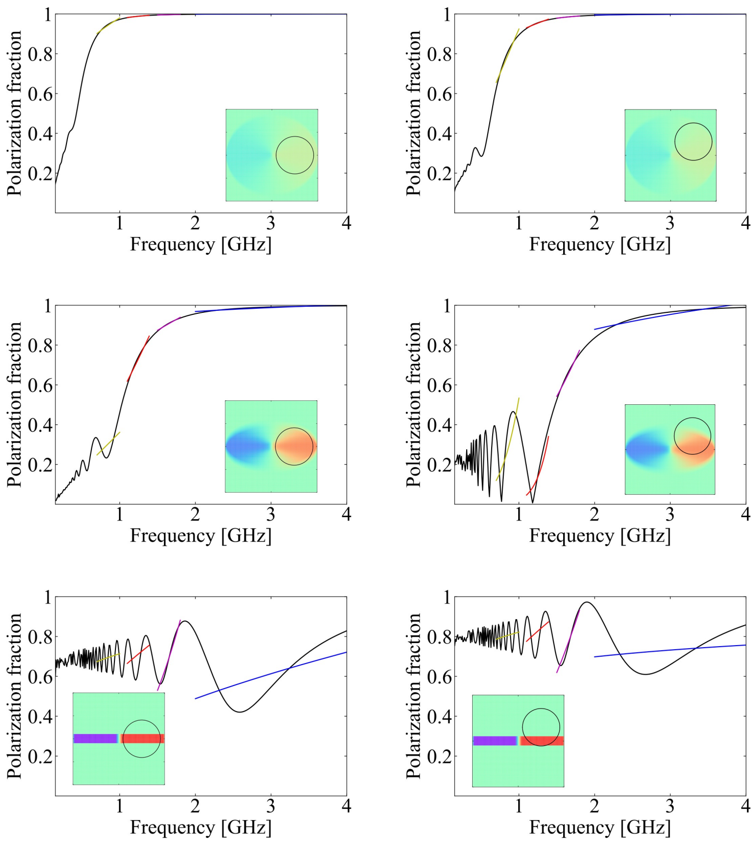

$(z, x_1, y_1) = (1.0, 5, 0)$ $(z, x_1, y_1) = (1.0, 5, 3)$

Figure 2.4: The polarization fraction as a function of the frequency. The left and right panels show the cases for $(z, x_1, y_1) = (1.0, 5, 0)$ and $(z, x_1, y_1) = (1.0, 5, 3)$, respectively, where the insets show the RM maps and the $1''$ beam position is shown as the black circle. The color scale is the same as that in Figure 2.3. The top and bottom panels show the results for the inclination angles of 30°, 60°, and 90°, respectively. The yellow, red, magenta and blue lines indicate the best fits assuming $p \propto \nu^{\beta}$ for the four different bands of 700−1000 MHz, 1100−1400 MHz, 1500−1800 MHz, and blue 2000−4000 MHz, respectively.

Table 2.2: The average and the standard deviation of the observer-frame, in-beam RMs of the DING for $z = 1.0$ and $x_1 = 5$ kpc.

y_1 (kpc)	i (degree)	average (rad/m^2)	standard deviation (rad/m^2)
0	30	10	1.3
0	60	26	6.5
0	90	35	54
3	30	8.7	2.6
3	60	16	13
3	90	25	50

increasing the beam offset.

In Figure 2.4, we see that background polarization is depolarized at low frequencies. However, although the standard deviation of RM monotonically increases with increasing the inclination angle, the degree of depolarization at low frequency does not. We see the decaying oscillation of the polarization fraction and its convergence at a certain value depending on i and y_1. The color lines in Figure 2.4 show what we obtain from the linear fit for such an oscillated profile.

Comparison between right and left panels indicates that the profile of the polarization fraction significantly depends on the beam offset. A decaying oscillation caused by depolarization appears at a smaller inclination angle (see the results for $i = 60°$) as we increase the beam offset. Since the beam offset determines the filling factor or the covering fraction of the DING for a beam, the filling factor is an essential parameter. Actually, for $(y_1, i) = (3, 60°)$, the polarization fraction converges at about 0.2 because the filling factor is about 0.8. The profile of the polarization fraction for $(y_1, i) = (3, 60°)$ is similar to that for $(y_1, i) = (0, 60°)$, but the polarization fraction of the former converges at a higher value than that of latter, because the polarized emission passes through more 0 rad/m^2 regions. As for $i = 30°$, we do not see the convergence of the polarization fraction. This is reasonable because the DING fully covers the beam area and the filling factor is unity. Similar results are found for x_1 instead of y_1.

The RM$_{\rm cls}$ derived from the $\chi - \lambda^2$ relation within the beam are summarized in table 2.3. RM$_{\rm cls}$ are mostly identical to the beam-averaged RM for $i = 30°$ and $i = 60°$, while they are very different from each other for $i = 90°$. The difference is made by significant depolarization which is seen even at the high frequency of 4 GHz (see Figure 2.4). The $\chi - \lambda^2$ relation suffers from estimating the beam-averaged RM in such a strongly-depolarized spectrum.

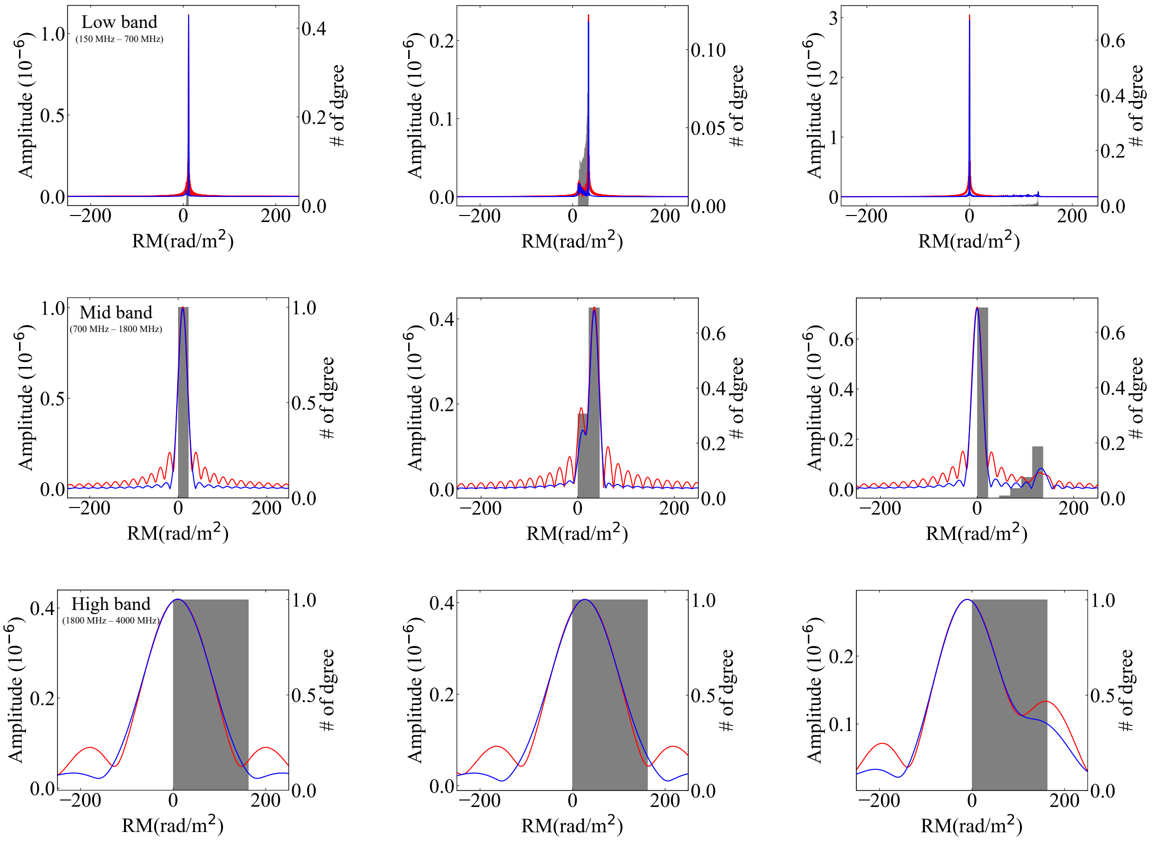

$i = 30°$ $i = 60°$ $i = 90°$

Figure 2.5: Histograms of RM (gray) and simulated FDFs (red and blue) for different inclination angles of the DING (left to right) and different frequency coverage (top to bottom). The gray color shows the histogram of RM, where the histograms are normalized by $1/(1+z)^2$. Red and blue lines show the dirty and cleaned FDFs, respectively. Panels from left to right correspond to the cases for the left to right panels shown in Figure 2.4.

Table 2.3: The observed RM, $\mathrm{RM_{cls}}$, with the $\chi-\lambda^2$ relation in-beam RMs of the DING for $z = 1.0$ and $x_1 = 5$ kpc.

y_1 (kpc)	i (degree)	$\mathrm{RM_{cls}}$ (rad/m^2)
0	30	10
0	60	26
0	90	12
3	30	8.7
3	60	16
3	90	-0.85

2.3.2 Estimation of DING's RM

Figure 2.5 shows the Faraday spectra obtained from Stokes parameters within the beam with $(z, x_1, y_1) = (1.0, 5, 0)$. Panels from the top to bottom show the results for low, mid, and high bands, respectively. The red and blue lines show the amplitudes of the dirty FDF obtained from Fourier transform of the complex polarized intensity and the cleaned FDF obtained from RM CLEAN, respectively. We also show the histograms of RM as the filled gray boxes, where the histograms are for observer-frame RMs of the projected numerical grids within the beam. If one refers to a rest-frame value of RM, it is reproduced by multiplying $(1+z)^2$. The bin size of x-axis (RM or Faraday depth) is equal to the FWHM of the RMSF for each band. The histogram does not depend on the observing band, but its appearance changes according to the adopted bin size.

If there is no DING, both the FDF and the histogram should have one peak at RM $= 0$ rad/m^2 with the zero width (i.e. the delta function). Figure 2.5 clearly indicates non-zero values of them, confirming that the DING significantly contributes to the FDF. Interestingly, the FDF and the histogram tend to show two peaks as the inclination angle increases (see e.g., the case with Mid band for $i = 90°$). The emission passing through a larger RM of the DING appears as a peak at non-zero Faraday depth, while the emission passing through a smaller RM of the DING or the emission not passing through the DING form another peak around RM $= 0$ rad/m^2. For $i = 90°$, most of the emission does not pass through the DING. Thus, the component around RM $= 0$ rad/m^2 becomes the dominant component of the FDF. The inclination angle close to the edge-on results in a larger RM gap between the two components than the case of a face-on, which means that the gap can be found at higher frequency even with a larger FWHM. Indeed, for $i = 60°$, it is difficult to identify the two component with high band, while for $i = 90°$ the two components are seen in the FDF even with high band. We note that this component may be numerical artifacts in Fourier transform (see Section 2.4.3).

We find that $\mathrm{RM_{peak}}$ tends to represent the RM value of the peak position of the histogram, and is clearly different from the actual, beam-averaged, observer-frame RM of the DING. The trend is clearly seen at the low band. For example, for $i = 30°$, $\mathrm{RM}_{\mathrm{peak}} \sim 12$ rad/m^2 overestimates the beam-averaged RM, ~ 10 rad/m^2, by about 15 %. Similarly, for $i = 60°$, $\mathrm{RM}_{\mathrm{peak}} \sim 34$ rad/m^2 overestimates the beam-averaged one, 26 rad/m^2. Then, when the undepolarized, intrinsic component dominates the FDF such as the case for $i = 90°$, $\mathrm{RM}_{\mathrm{peak}}$ suggests 0.0 rad/m^2, although the beam-averaged RM is 35 rad/m^2. The classical estimate of RM, $\mathrm{RM}_{\mathrm{cls}}$, tends to represent the mean RM of the LOS and is hence close to the beam-averaged RM value. As a result, $\mathrm{RM}_{\mathrm{peak}}$ is also different from $\mathrm{RM}_{\mathrm{cls}}$.

Overall, the shape of the cleaned FDF is similar to the histogram, except the result of Low band for $i = 60°$ which shows that the position of the secondary peak component is not at the peak of the histogram but around the edge of the histogram. We will discuss the reason in Section 2.4.3.

2.3.3 Statistical contribution of DING

Although our model of the DING is too simple to make quantitative predictions, we demonstrate how the effect of the DING qualitatively emerges (or is hidden) in statistical studies. Particularly, we focus on the redshift evolution of observed RMs, because such a study is one of the key Magnetism science of forthcoming surveys (Section 2.1).

To study the statistical contribution of the DING, we carry out Monte-Carlo simulations as described in Section 2.2. A foreground RM screen such as the DING shifts the Faraday depth of a background source, and the amount of the shift depends on the strength of DING's magnetic field as well as the DING's parameter such as the inclination angle and the beam offset. Thus, in a catalog of background polarized sources, DING's RM appears as the standard deviation of the observed RMs, σ_{RM}, where the observed RM is defined as the Faraday depth at the FDF peak, $\mathrm{RM}_{\mathrm{peak}}$, using Faraday tomography.

The standard deviation of the DING's RMs as a function of the DING's redshift is shown as the circles in Figure 2.6. We fit σ_{RM} with the following exponential function;

$$\sigma_{\mathrm{RM}}(z) = \frac{A}{(1+z)^k} \ [\mathrm{rad/m^2}]. \tag{2.7}$$

The best-fit (the solid line) values are $A \sim 60$ and $k \sim 2.7$.

The observed RM is always $1/(1+z)^2$ times the intrinsic value because RM is proportional to the square of the wavelength. To confirm this dependence, we perform the control run in which the region where the emission passes through the DING is constant regardless of the redshift (the beam size is changed at each redshift). The size of the region to be passed through is thus fixed at 1.8 kpc in diameter. The result is also shown as the triangles in Figure 2.6. The best-fit (the dashed line) values are $A \sim 51$ and $k \sim 1.8$ which is marginally consistent with the dependence of $1/(1+z)^2$. Therefore, the steeper redshift dependence of $k \sim 2.7$ relates to the change of the physical size of the beam. We discuss this mechanism in section 2.4.4.

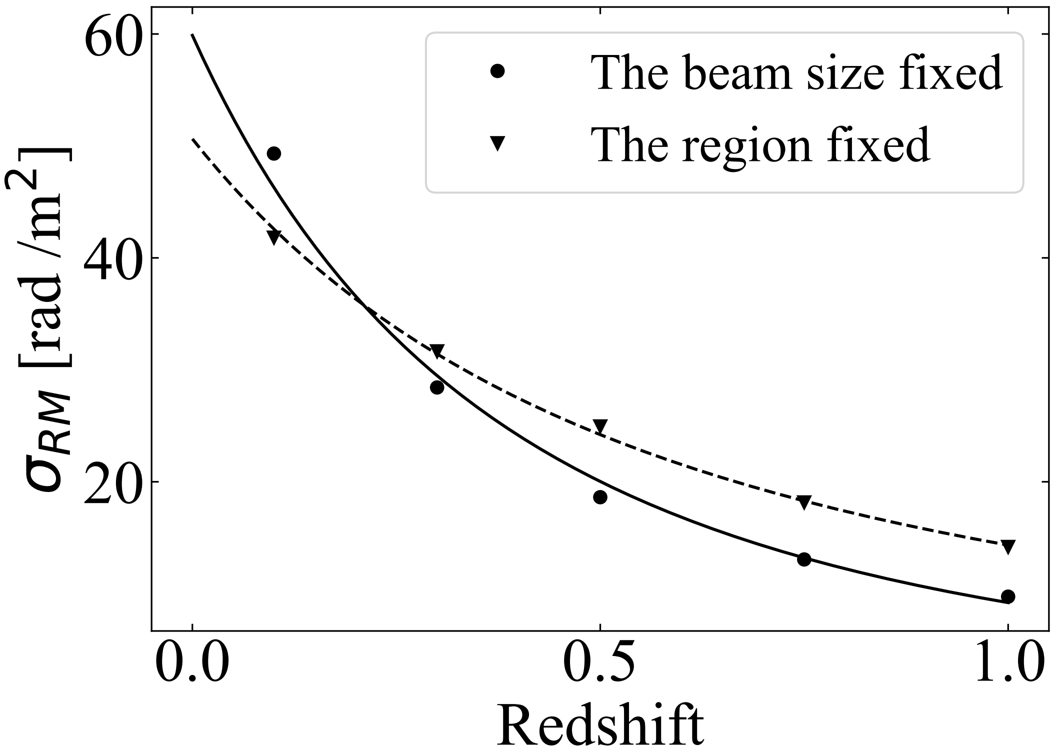

Figure 2.6: Standard deviation of $\mathrm{RM}_{\mathrm{peak}}$, σ_{RM}, as a function of the redshift, z. The circles and triangles, respectively, show the results of our fiducial runs and our control runs for which we fix the physical beam size of 1.8 kpc in diameter. The solid and dashed lines are the best least-square fit assuming the power-law, for our fiducial and control runs, respectively.

2.4 Discussion

2.4.1 Model dependence

We conducted numerical simulations of depolarization caused by a DING using the simplest model consisting of a uniform density and a ring magnetic field. In this subsection, we expand our simulations to more complicated but more realistic models of a DING, although the essence of depolarization effects caused by a DING can be understood based on the results of our simplest model. The magnetic field models are from the section 1.4.

Density profile

First, the global electron distribution is assumed to be uniform in this paper. The global electron distribution has been studied in the literature and some realistic models have been proposed such as NE2001 [97] and YMW16 [98]. These works suggest that the global electron distribution basically follows an exponential profile as functions of the distances from the galactic center and the disk mid-plane. Such a profile induces the two additional effects, bias and gradient. The bias effect is that RM is the largest around the central part of the DING and weaker at its outskirt. Nevertheless, the electron density is positive definite, so that the change of the sign of RM caused by the disk magnetic field remains regardless of the electron distribution model. The gradient effect is that the density gradient induces the RM gradient as well, resulting in more depolarization within the beam in general.

We consider exponential distribution for the electron density distribution, $n(z)$:

$$n(z) = n_0 \exp\left\{-\left(\frac{z}{H}\right)\right\}. \tag{2.8}$$

We adopt $n_0 = 0.014$ cm^{-3} and scale height, $H = 1.83$ kpc [99]. To see the effect of the density profile, we adopt the exponential distribution for the electron density (Equation 2.8) on our simplest ring magnetic field model and study the same case of $(z, x_1, y_1) = (1.0, 5, 0)$. We then see no apparent change of the results for $i = 30°$ and $i = 60°$, because the main disk component has approximately the same density value for the uniform and exponential models. Meanwhile, we see a difference between the two models for $i = 90°$. The second peak of FDFs, as seen in the right column of Figure 2.5, looks flat, because the electron distribution is exponential.

The above result clarifies that the exponential distribution does not significantly change the depolarization through the galactic disk. Hereafter, we consider the exponential distribution of the electron density to incorporate this effect on our additional simulations shown in the following sections.

Table 2.4: The average and the standard deviation of the observer-frame, in-beam RMs of the DING.

Model type	(z, x_1, y_1)	i (degree)	average (rad/m^2)	$\sigma_{\rm RM}$ (rad/m^2)
ASS	$(1.0, 5, 0)$	30	0.87	3.6
BSS	$(1.0, 5, 0)$	30	-3.1	2.7
BSS	$(0.1, 0, 8)$	90	0.0	0.0
BSS + D	$(0.1, 0, 8)$	90	0.0	0.17
BSS + Q	$(0.1, 0, 8)$	90	0.0	0.17
ASS	$(0.3, 5, 0)$	30	3.6	9.4
ASS + random	$(0.3, 5, 0)$	30	3.5	10

Disk fields

We considered the ring magnetic fields which indicate one pair of positive and negative RM structures through the disk (see e.g., Figure 2.3). Such pairs can be obtained if we consider a spiral magnetic field such as the axi-symmetric spiral (ASS). Significant depolarization and the bi-modal FDF profile are expected, if the beam covers such the pairs producing the large RM dispersion. If we consider even higher-mode spirals such as the bi-symmetric spiral (BSS), there are more reversals of magnetic fields and multiple pairs of positive and negative RM structures through the disk. Thus, the number of the peak components in the FDF depends on the mode. The mode also changes the amount of depolarization, because the dispersion of RM within the beam depends on the mode.

To assess the above speculation, we show the results for the ASS and BSS models [59]. The results with the inclination angle of 30° and $(z, x_1, y_1) = (1.0, 5, 0)$ are shown in Figure 2.7. The top panels are the same as Figure 2.4 but for ASS (left) and BSS (right) models. The middle and bottom panels are the same as Figure 2.5 but for ASS (left) and BSS (right) models. The average and the standard deviation of RM within the beam are summarized in table 2.4.

As expected, the dispersion of RM caused by the positive and negative RM pairs within the beam for the ASS and BSS models are larger than that for the RING model (tables 2.2 and 2.4), because the ASS and BSS models have more magnetic field reversals. A significant depolarization spectrum is seen as well (the top panels of Figure 2.7). As shown in the insets of the top panels, the ASS and BSS models possess positive and negative RM regions within the beam, so we expect multiple peaks in the FDF. Actually, the peaks can be resolved with the low-band data (the middle panels), and we can clearly see two peaks for the ASS model. Meanwhile, such multiple peaks are not apparent in the FDF with the mid-band data (the bottom panels), since the RM structure within the beam is smaller than the resolution of the FDF.

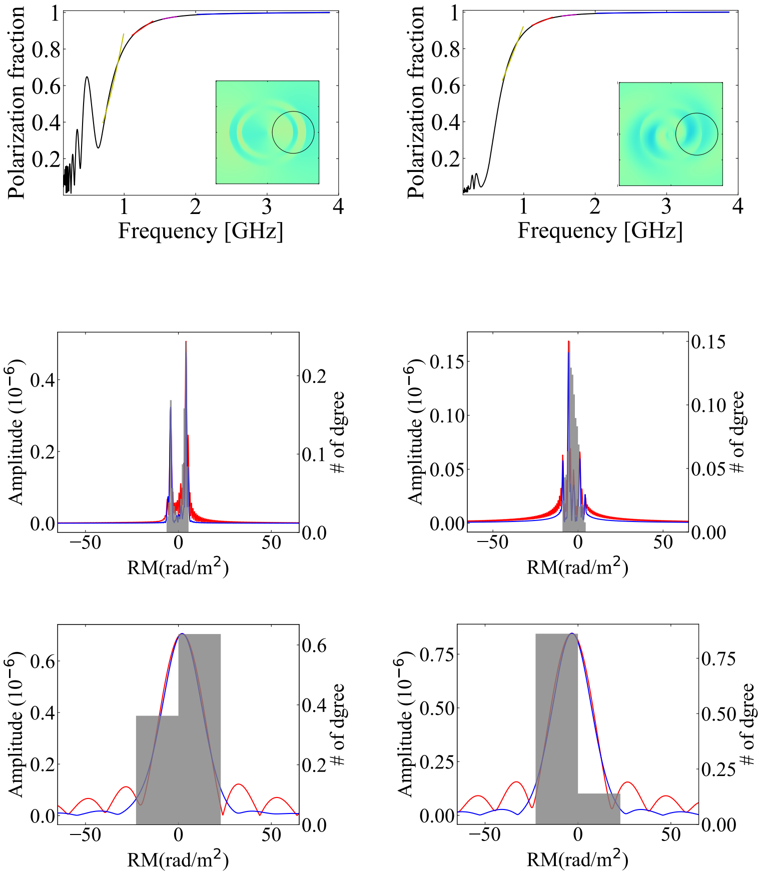

ASS model

BSS model

Figure 2.7: Top panels: The polarization fraction as a function of the frequency. The left to right panels show the results for the inclination angles of 30° with ASS and BSS model, respectively, where the insets show the RM maps and the 1″ beam position is shown as the black circle. The color scale is the same as that in Figure 2.3. The both panels show the cases for $(z, x_1, y_1) = (1.0, 5, 0)$. The yellow, red, magenta and blue lines indicate the best fits that is the same as that in Figure 2.4.Center and bottom: Histograms of RM (gray) and simulated FDFs (red and blue) for different models of the DING and different frequency coverage. The gray color shows the histogram of RM, where the histograms are normalized by $1/(1+z)^2$. Red and blue lines show the dirty and cleaned FDFs, respectively. Panels from center to bottom show the results for the frequency coverage of low (150 MHz – 700 MHz), mid (700 MHz – 1800 MHz), respectively.

Halo Fields

We did not consider magnetic fields in the galactic halo. Previous works have shown that there are global magnetic fields in the halo of the Milky Way [62, 100] and external galaxies [101, 102, 103]. Because of a lack of the halo component in this work, RM is exactly zero through the halo direction when we observe the DING in the edge-on view. This would be unlikely because the global electron and magnetic fields in the halo should have non-zero RM structures. Such RM can be small (say $\lesssim 1$ rad/m^2) because of an exponential decrease of the electron density toward the halo, supporting that the disk component is predominant for the DING.

To examine the contribution of halo magnetic fields to the DING's depolarization quantitatively, we add a toroidal magnetic field with the asymmetric configuration in longitude and latitude relative to the galactic plane and the center, respectively (labelled D), or an axisymmetric magnetic field without reversals relative to the plane (labelled Q) [62]. The results are shown in Figure 2.8. The average and the standard deviation of RM within the beam are summarized in table 2.4.

This additional halo component produces more complex RM structures in the FDF in general, regardless of the model (not shown). A clear difference made by the halo field is seen when we view the DING through the edge-on. The top panels in Figure 2.8 show the frequency dependence of the polarization fraction for the inclination angles of 90° and $(z, x_1, y_1) = (0.1, 0, 8)$. The left to right panels compare the results with BSS, BSS + D and BSS + Q models, respectively, showing that the additional halo component causes depolarization at low frequency because the BSS + D and BSS + Q models have non-zero standard deviations within the beam (table 2.4). The bottom panels in Figure 2.8 show the Faraday spectra respectively corresponding to the top panels. Because the RM structure within the beam is finer than the resolution of the Faraday depth, the FDF apparently indicates one component. This demonstrates that, even when the effect of DING is not clearly seen in the Faraday spectrum, we may be able to find depolarization caused by a weak magnetic field such as a halo magnetic field at very low frequencies.

Note that galaxies including DINGs probably possess the circumgalactic medium (CGM) that extends to 400 – 500 kpc from the center [33, 104]. Although the typical values of the density and magnetic field of the CGM are not clear, CGM's RM could be small like the gas in the halo. With realistic halo gas and RM, our results relating to the filling factor will be improved.

Turbulence

We did not consider small-scale random and turbulent magnetic fields which have been addressed in the previous works as a source of depolarization (e.g., [59]). If we consider turbulent magnetic fields, our results will largely change. More specifically, our results show the minimum case and an additional depolarization takes place by the turbulent component. For example, for the case with $i = 30°$ in Figure 2.4, the polarization fraction remains almost unity at above 1000 MHz. This is because the standard de-

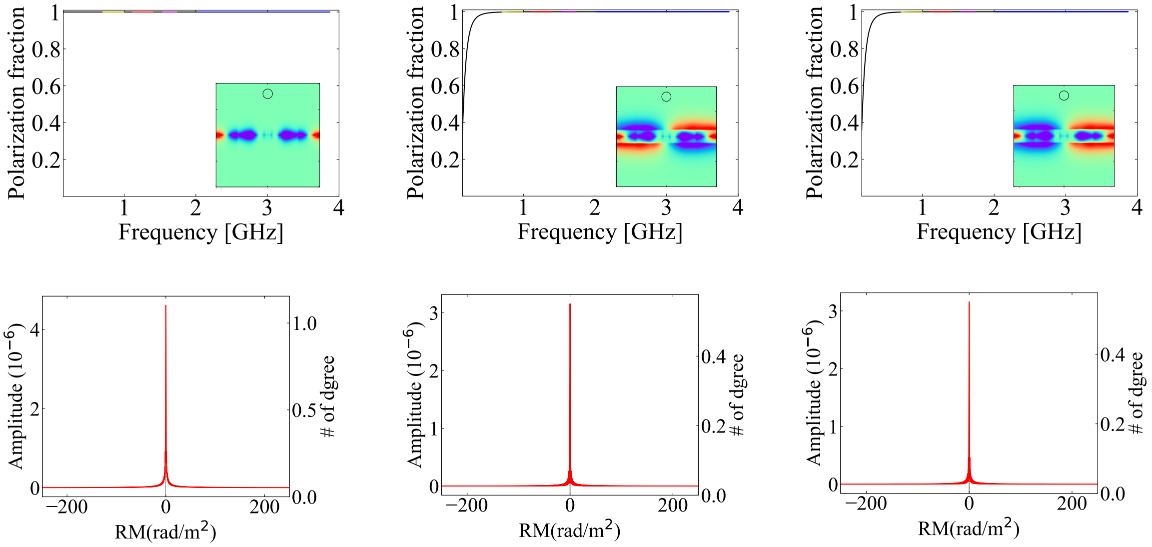

BSS

BSS + D

BSS + Q

Figure 2.8: Top: The polarization fraction as a function of the frequency. The left to right panels show the results for the inclination angles of 90° with BSS, BSS + D and BSS + Q model, respectively, where the insets show the RM maps and the $1''$ beam position is shown as the black circle. The color scale is the same as that in Figure 2.3. The panels show the cases for $(z, x_1, y_1) = (0.1, 0, 8)$. The yellow, red, magenta and blue lines indicate the best fits that is the same as that in Figure 2.4. Bottom: Histograms of RM (gray) and simulated FDFs for different models of the DING (left to right). The gray color shows the histogram of RM, where the histograms are normalized by $1/(1+z)^2$. Red show the dirty.

viation of intrinsic RM within the beam, 5.6 rad/m^2, does not significantly rotate the polarization angles at those frequencies. Such a result varies if there is an additional RM dispersion induced by turbulent magnetic fields. The significance of this addition depends on the model of turbulence and hence accurate modeling of turbulent magnetic fields is crucial [81].

To explore the contribution of the random component, we adopt a simple model that the random component is homogeneous and follow a Gaussian distribution in strength with an average of zero and a scatter of $\sigma_b/\sqrt{3}$ in each dimension, where σ_b is the standard deviation of the random component. We set the parameter, $\sigma_b = 3$ (μG), based on the previous work [59].

The results for the ASS model and the ASS + random field model are compared to each other in Figure 2.9. The average and the standard deviation of RM within the beam are summarized in table 2.4. As expected, the random component induces more depolarization, because the random component increases the standard deviation of RM within the beam. The FDF has two peaks for both the ASS and ASS + random models, but the latter indicates a broader FDF with more spikes. The random magnetic field can smooth the coherent RM structure formed by the global magnetic field, because random components have a Gaussian distribution. Thus, the amplitude of the FDF will become lower and the width of the FDF will become wider, but remaining the split of FDF. We note that we see one Gaussian RM structure if RM structure has no global component.

2.4.2 Quantification of depolarization

The polarization spectral index β of $p \propto \nu^\beta$ has been adopted to quantify the degree of depolarization (e.g., [67]). We derived the best-fit values of β for the four frequency bands (color lines in Figure 2.4), but it demonstrates that the linear fit is unreasonable to represent the oscillation of the polarization fraction caused by the DING. Such oscillation happens when the DING's RM is large. Here, as already shown, a larger inclination angle causes a larger RM, because not only the path length through the disk but also its $B_\parallel$ component becomes larger. Hence, a larger inclination angle results in stronger depolarization, because the standard deviation of intrinsic RM for the DING becomes larger. However, a larger inclination angle can reduce the chance for the beam to overlap the disk (see Figure 2.2), i.e. reduce the filling factor from unity. As a result, two components of polarization are found within a beam; one is the emission which is significantly depolarized by passing through the galactic plane with a large RM, showing a decaying oscillation in the profile of the polarization fraction. The other is the emission that can reach us without passing through the galactic plane, determining the convergence of the observed polarization fraction at the value of 1 - the filling factor.

The " Burn law" [45] is another analytic formula to quantify the depolarization. The formula is written as

$$p(\lambda) = p_0(\lambda) \exp\{(-2\sigma^2\lambda^4)\}, \tag{2.9}$$

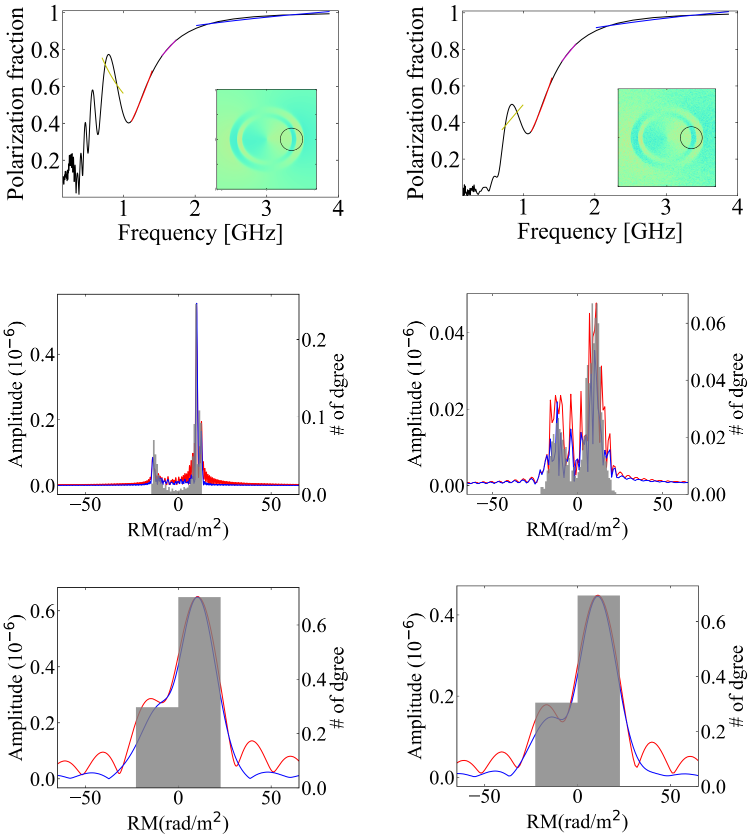

ASS model

ASS + random model

Figure 2.9: Top: The polarization fraction as a function of the frequency. The left to right panels show the results for the inclination angles of 60° with, ASS and ASS + random model, respectively, where the insets show the RM maps and the $1''$ beam position is shown as the black circle. The color scale is the same as that in Figure 2.3. The panels show the cases for $(z, x_1, y_1) = (0.3, 5, 0)$. The yellow, red, magenta and blue lines indicate the best fits that is the same as that in Figure 2.4. Bottom: Histograms of RM (gray) and simulated FDFs for different models of the DING (left to right). The gray color shows the histogram of RM, where the histograms are normalized by $1/(1+z)^2$. Red and blue lines show the dirty and cleaned FDFs, respectively.

where λ is the wavelength and σ is the standard deviation of RMs within a considering beam. Obviously, the exponential formula is difficult to reproduce the non-monotonic change of the polarization fraction caused by the DING. But this discrepancy is reasonable because RMs within the beam do not follow the Gaussian distribution which is assumed in the Burns law. Moreover, a condition that a typical size of incoherent structures is sufficiently smaller than the beam is not satisfied.

These results indicate that the above traditional methods can only quantify a part of the DING's broadband depolarization properties at relatively high frequency of ~GHz. Careful examination of the profile of the polarization fraction at a few to several hundred MHz is important to understand the depolarization caused by the DING. Fitting of the profile of the polarization fraction with advanced models such as the two components model (see Appendix of [67]) would be useful to extract the features caused by the filling factor.

2.4.3 Shapes of the Faraday spectrum

The shape of the FDF obtained from RM CLEAN is similar to the shape of the histogram of RM within the beam. While the histogram is the normalized histogram of RMs for the pixels within the beam, the FDF is the sum of the FDFs for the pixels within the beam. Because we consider a uniform linear polarization within the beam, the sum of the FDFs results in the histogram of Faraday depths for the pixels within the beam and the histogram can be compared to the normalized histogram of RMs. In reality, the shape of the FDF can depart from the shape of the histogram, if the amplitude of linear polarization is very inhomogeneous within the beam. This situation can occur when the emission has a significant structure, such as radio lobes, or when there is strong intrinsic depolarization due to small-scale turbulence. Another factor that causes the departure is numerical artifacts in the Fourier transform. We can see the artifact at the edge of the histogram in the top-middle panel of Figure 2.5. We speculate that the peak is spurious that appears at the edge when we reproduce a square wave using a sine wave in the Fourier series expansion. A sophisticated method of Faraday tomography is required to make sure that we obtain the FDF which accurately reproduces the shape of the histogram.

We find that the beam-averaged RM of the DING deviates from $\mathrm{RM}_{\mathrm{peak}}$, Faraday depth at the peak of the FDF. The reason why the peak of the FDF stands at a non-average RM position within the beam is that the region through which polarized emission passes contains many 0 rad/m^2 regions. The discrepancy is, however, not surprised because the mean value and the mode value of the distribution are not always the same for a statistical distribution like the histogram. In the future, we need to perform Faraday RM synthesis for millions of sources obtained from large surveys. A choice of $\mathrm{RM}_{\mathrm{peak}}$ as the RM toward the source is reasonable because that is easy to obtain from a simple Faraday RM synthesis (and RM CLEAN as an option). But it is not reasonable to refer $\mathrm{RM}_{\mathrm{peak}}$ for the study of magnetic fields of DINGs because $\mathrm{RM}_{\mathrm{peak}}$ (the mode value) can be far from the average RM (the mean value, i.e. the first moment of the FDF) which is a more representative value for the study of DING's magnetic fields. Another problem relating to the RM catalog is that we can obtain multiple FDF peaks (Figure 2.5) depending on the filling factor, although we consider a single background source. The split of a single source into multiple sources by a DING impacts on the studies of, for example, modeling of the foreground Milky Way RM map, study of the luminosity distribution function, and exploration of the intergalactic magnetic field (IGMF). Examining the profile of the polarization fraction as well as referring to optical absorption lines are promising ways to identify the existence of DINGs along the line of sight.

2.4.4 Redshift dependence of $\sigma_{\rm RM}$

The standard deviation of DING's RM, $\sigma_{\rm RM}$, depends on the redshift (Section 2.3.3). But the dependence, $k \sim 3$ for $\sigma_{\rm RM} \propto (1+z)^{-k}$, deviates from the expectation of $k \sim 2$ based on the wavelength-squared dependence of the RM. We claim that this steeper redshift dependence relates to the change of the physical size of the beam, i.e. the filling factor of the DING in the beam. To understand the effect of the filling factor more clearly, we again perform the control runs in which we fix the physical size of the beam. Since the filling factor significantly depends on the inclination angle of the DING, we separately show the results of the Monte-Carlo simulations for different inclination angles. The results are shown in Figure 2.10. As expected, we obtain $k \sim 2.1$ and $k \sim 2.0$, for $i = 30^\circ$ and $i = 60^\circ$, respectively, both in good agreement with $k \sim 2$ based on the wavelength-squared dependence. Meanwhile, for $i = 90^\circ$with a small filling factor, we find that the result does not follow the expected dependence; $\sigma_{\rm RM}$ of ~ 80 rad/m^{2}quickly decreases as the redshift increases and then it reaches about 0 rad/m^{2}at $z \gtrsim 0.3$.

Let $\sigma_{\rm RM_{sum}}$ be the sum of the standard deviations for the three inclination angles, $\sigma_{\rm RM30}$, $\sigma_{\rm RM60}$, and $\sigma_{\rm RM90}$, respectively,

$$\sigma_{\rm RM_{sum}} = \sqrt{\sigma^2_{\rm RM90} + \sigma^2_{\rm RM60} + \sigma^2_{\rm RM30}}, \tag{2.10}$$

we obtain Figure 2.11 and $k \sim 2.9$, which is closer to $k \sim 2.7$ of our Monte-Carlo simulations. This simple test suggests that the deviation from $k \sim 2$ is caused mainly by the quick drop of $\sigma_{\rm RM90}$ in redshift. This drop is caused by an enlarge of the physical beam size and a quick decrease of the filling factor for the case of the edge-on. Note that we consider 700 -1800 MHz to determine $\rm RM_{peak}$. Even if we consider wider frequency coverage such as 120 -1800 MHz, the result does not significantly change.

Understanding the above statistical property of the DING's contribution to observed RM is crucial to exploring the IGMF. Recent works adopt the idea to see the RM gap between extragalactic polarized sources located at different redshifts [105] and reduce foreground contributions by comparing random and physical pair-sources [87, 88]. Here, for random pair-sources, the sources at a higher redshift have more chance to be intervened by DINGs as well as more contribution from the IGMF. It would be difficult

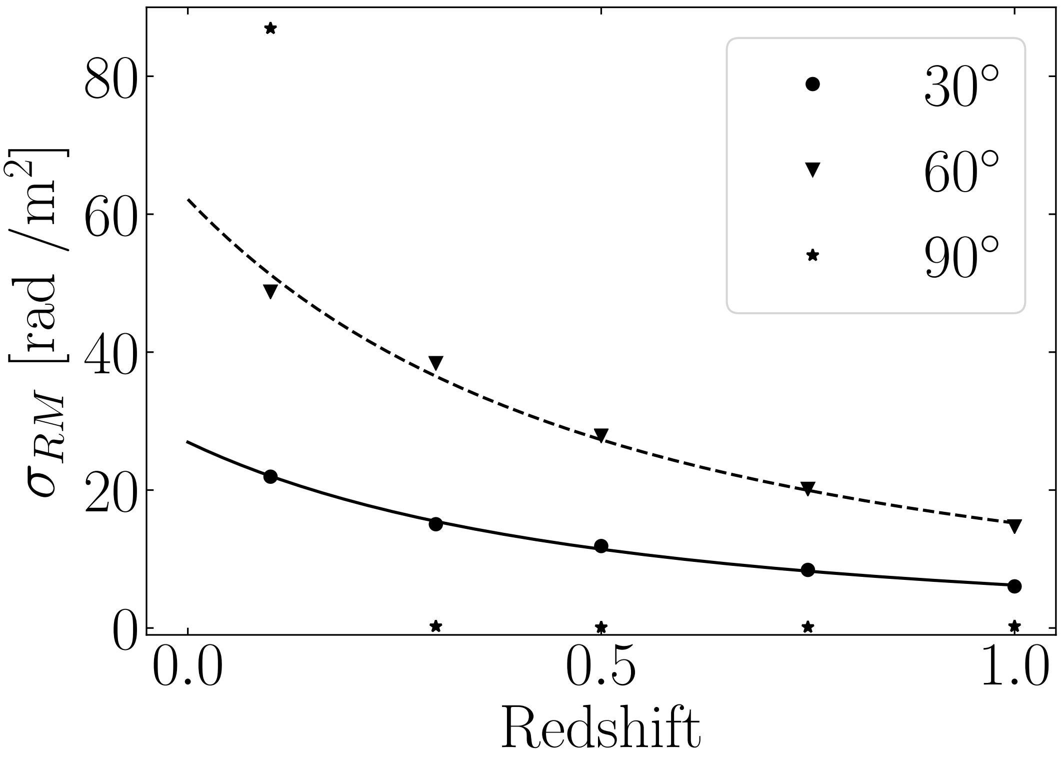

Figure 2.10: Same as the control run in Figure 2.6 but separately shows the results of a different inclination angle, the circles for $i = 30°$, the triangles for $i = 60°$, and the stars for $i = 90°$. The solid and dashed lines indicate the best-fit power laws for $i = 30°$ and $60°$, respectively.

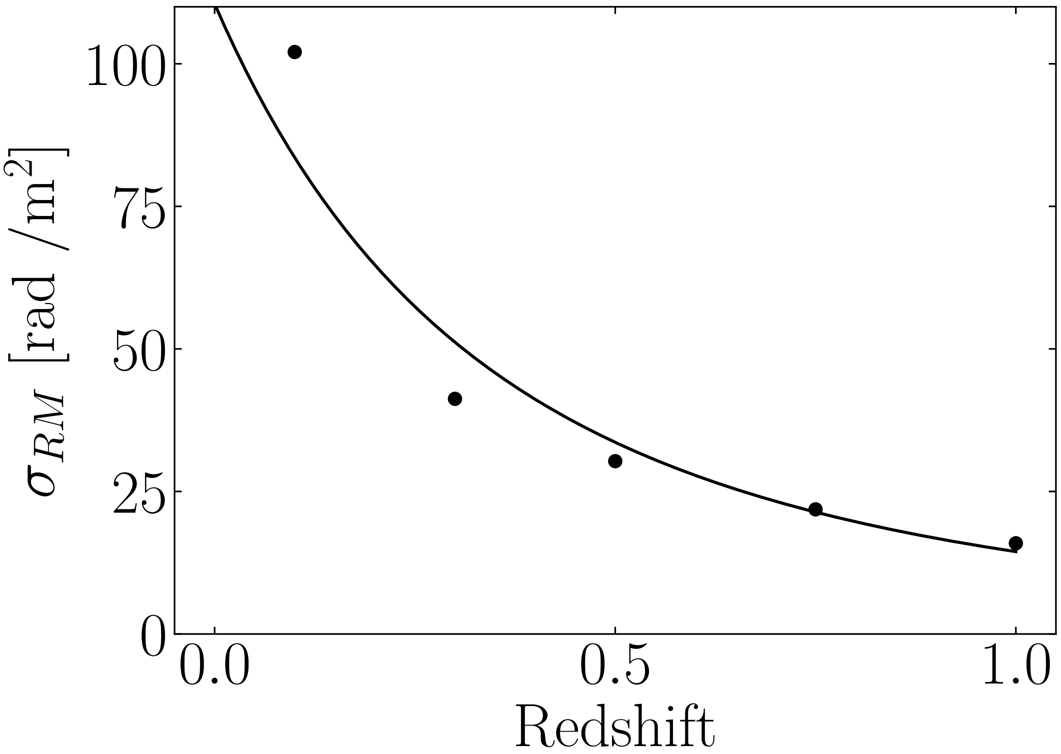

Figure 2.11: Same as the control run in Figure 2.6 but the sum of only the cases for $i = 30°$, $60°$, and $90°$. The solid line indicates the best-fit power laws.

to distinguish these contributions from RM data only, remaining a large uncertainty of the estimation of the IGMF. This contamination is also a major problem when we probe the IGMF from the relationship between the RM and redshift of extragalactic sources ([85], [86], [106]). Our results suggest that to reduce this uncertainty, we should either focus on polarized sources found at low frequencies and/or select sources that do not show strong depolarization features. In both cases, it is expected no strong DING along the line of sight. Consequently, we obtain a limited number of available sources so far, but future large surveys of RM would deliver a sufficient number of the sources to detect the excess RM caused by the IGMF (see [107]).

2.5 Conclusion

In order to clarify the contribution of intervening galaxies to the observed polarization properties, we simulated the depolarizing intervening galaxy (DING) along the line of sight when observing a uniform background source. We find that the degree of depolarization depends on the inclination angle and the impact parameter of the DING. We found that the larger the standard deviation, the more likely it is that depolarization will occur. The shape of the Faraday dispersion function (FDF) obtained from RM CLEAN represents the shape of the histogram of RM within the beam and the multi components are clearly visible in the FDF. The appearance of the multi components depends on the model of the DING, but the fraction of the DING that covers the background emission (the filling factor) and the RM structure within the beam are essential. Faraday tomography indicated that the peak Faraday depth of the FDF is different from the beam-averaged RM and the observed RM with the classical style of the DING. We performed Monte-Carlo simulations to understand statistics of polarization properties. The simulations suggest that the standard deviation of observed RMs for the DINGs follows $\sigma_{\mathrm{RM}} \propto 1/(1+z)^k$ with $k \sim 2.7$.

Finally, the SKA and SKA Precursor/Pathfinder will probe a large number of extragalactic polarized sources that can be depolarized by DINGs discussed in this paper. Although we did not consider observational specifications in detail such as angular resolution and frequency coverage, our simulations indicate that the specifications are very important to accurately evaluate the impact of DINGs on these observations. Such work should be achieved along with the development of survey strategies in the future.

Chapter 3

Polarization Analysis of Gravitational Lens Galaxies for Future Polarization Surveys

3.1 Introduction

We should know when a galaxy has a coherent magnetic field and how much the strength of it is. Strong gravitational lensing galaxies have been focused on for their importance in magnetic field observations of distant galaxies. Polarization of the background source passes through different parts of the gravitational lensing galaxy and experiences different Faraday rotations. Since the paths are the same except for the region passing through the gravitational lensing galaxy, it can be assumed that the Faraday effect of the background source and the foreground of the Milky Way are negligible for the galaxy. Therefore, the Faraday rotation of each path represents information about the large-scale and small-scale magnetic fields of the gravitational lensing galaxy.

Greenfield et al. (1985)[108] studied radio polarization from two gravitational lensing images of quasar 0957 +561 at multiple wavelengths and found that the RMs of the two paths differ by 100 rad/m^2. However, this study did not discuss magnetic field information in detail due to frequency bandwidth and channel number issues. Approximately 30 years later, Mao et al.(2017)[1] performed broadband polarization observations of the gravitational lensing galaxy CLASS B1152+199. They used Faraday tomography to obtain Faraday spectra of the lensing images and found that the RMs of the two paths differ by 500rad/m^2. Using this technique, they detected a coherent magnetic field with a magnitude of about μG at $z = 0.439$. More recently, Geach et al. (2023)[109] focused on a lensed galaxy and detected linearly polarized thermal radiation from dust in a strongly gravitationally lensed galaxy ($z = 2.6$). It was suggested that the dust has a coherent magnetic field of 5 kpc with an intensity of less than about 500 μG parallel to the molecular gas disk. As described above, the method using strong gravitational lensing is very useful for observing the magnetic field of distant galaxies. However, the separation of gravitational lensing images is typically less than 1 arcsecond, which makes spatial resolution difficult with existing radio interferometers. In other words, the development of magnetic field observations of distant galaxies should be advanced if we can use the same gravitational lensing RM differencing technique, even if it is spatially unresolved in radio observations. As we show in chapter 3, we can use Faraday tomography to determine the RM structure in the beam as multiple peaks [110]. Therefore, we focused on the possibility of using this feature to extract the RM structure of lensing galaxies from the unresolved spectrum. We will investigate whether this feature can be used to extract the RM structure of lensing galaxies from the unresolved spectra.

In the Square Kilometer Array (SKA) era, it is expected to find 10^5 polarization sources subject to gravitational lensing effects [70]. All-sky polarization surveys using the SKA predecessor have now begun. Thus, it is an excellent opportunity to observe the magnetic fields of distant galaxies. This method should be established because many polarization sources affected by gravitational lensing effects will be found in the next few years.

In this chapter, we investigate whether it is possible to retrieve the RM structure of lensing galaxies when the background polarization sources are subject to gravitational lensing effects and are spatially unresolved. In Section 3.2 we discuss the model and calculations, and in Section 3.3 we show the results of estimating the RM structure using QU-fitting with and without the requirement of the same polarization angle. We also will investigate what paths the method can be applied to. We show the statistical trends. In Section 3.4, we discuss whether the multiple peaks in the Faraday spectrum can be distinguished from background sources. We also discuss the extent to which QU-fitting can be applied when the gravitational potential is changed. Finally, we summarize this work in Section 3.5.

3.2 Calculation

We use a similar observation simulation method as described in Omae et al. (2023) [110], with the exception of our consideration of background emission passing through two lines of sight (LOS). The Stokes parameters, polarized angle, and RM are calculated by

$$\begin{cases} \mathrm{RM}_k = 0.81\left(\frac{n_e}{\mathrm{cm}^{-3}}\right)\left(\frac{B_\parallel}{\mu\mathrm{G}}\right)\left(\frac{\Delta l}{\mathrm{pc}}\right) \\ \mathrm{RM} = \sum_{k=1}^{N}\mathrm{RM}_k \\ \chi = \chi_0 + \mathrm{RM}\lambda^2 \\ Q = Q_0\cos\chi - U_0\sin\chi \\ U = Q_0\sin\chi + U_0\cos\chi, \end{cases} \tag{3.1}$$

where RM_k is RM within the k-th grid along a certain line of sight, n_e is thermal electron density within the k-th grid, $B_\parallel$ is the component of the magnetic field that is parallel to the line of sight within the k-th grid, $\Delta l = 100$ pc is the line element.

We integrate the RM and the polarized angle, χ, along the z-axis and project the cumulative values onto the x-y plane. We sum up Q (or U) values for the projected grids that the background emission passes through and obtain the observed Q (or U) within that region. In this chapter, we consider two lines of sight at the lens. After calculating each path using Equation 3.2, we add them together to obtain the observed quantity.

We perform Monte Carlo simulations and investigate the statistical feature. We set the positions of background sources as the free parameters of Monte-Carlo simulations. We use the background source as a point source of quasars and supernovae to calculate the light path. As we calculate the light path through the intervining galaxy, we adopt the lens model software PyAutoLens (AutoLens) [111, 112, 113]. We use PyAutoLens's 'PositionSolver' for this purpose. This study assumes a strong gravitational lens with two separate images. We choose only two of these solutions through the path. We consider the point source as the background source and the mass model of the lensing galaxy is the point source. The Einstein radius is 1". Figure 3.1 shows the positions of two split images. We calculate the RM within the beam and polarization data, then adopt QU-fitting, and estimate RM structures.

3.2.1 Fitting models

We considered the following two Faraday screen models for QU-fitting. These models are based on the external Faraday screen mode [114]. This model consists of isotropic turbulent magnetic fields within the beam and the gradient of RM within the beam. The external Faraday screen model was written by

$$P(\lambda^2) = A\exp\bigl(2i(\mathrm{RM}_0\lambda^2 + \chi_0) - 2\sigma_{\mathrm{RM}}^2\lambda^4\bigr)\frac{\sin\Delta\mathrm{RM}\lambda^2}{\Delta\mathrm{RM}\lambda^2}, \tag{3.2}$$

where $P = q + ju$, $q = Q/I,\ u = U/I$, A is amplitude of FDF, RM_0 is RM of intrinsic background source, σ_{RM} is the standard deviation of RM within a beam and $\Delta\mathrm{RM}$ is the variation in RM across the beam. Since the Stokes parameters Q and U are proportional to frequency, we need to divide each polarization Stokes parameter by the radiation intensity, I, to remove this effect.

The first model is the external screen model as above [48], and we will refer to this model as m1 for ease of reference. The second model is a model that reduces uncertainties in the initial polarization angle. This model has imposed a requirement, which is the initial polarization angles are the same. In the case of gravitational lensing systems, both polarization sources visible in the image are the same background source, so the polarization angles are the same. This is why we can reduce parameters by imposing this requirement. We call this model m2 hereafter. Even if there are multiple screens, i.e., multiple parameters, χ_0 is treated as a common parameter.

The χ^2 test is used to see the accuracy of the fitting, where χ^2 is written by $\sum\frac{(\mathrm{observed}-\mathrm{expected})^2}{\mathrm{expected}}$.

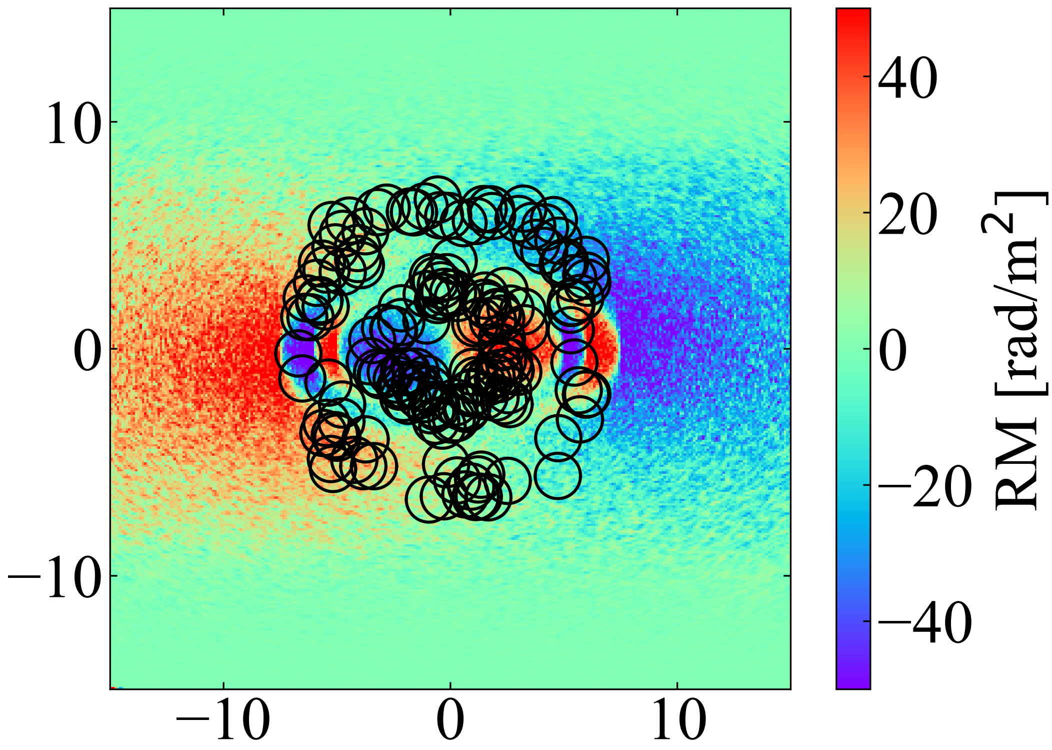

Figure 3.1: The positions of two split images overlap RM map and the Einstein radius of the mass model of the lensing galaxy is 1". The black circle is the position through which the background emission passes.

Table 3.1: parameters

RM_1 (rad/m^2)	σ_{RM_1} (rad/m^2)	RM_2 (rad/m^2)	σ_{RM_2} (rad/m^2))
-24.4	5.72	13.8	4.76

3.2.2 Mock data for fitting

This study aims to investigate whether we can separate spatially resolved emissions affected by gravitational lensing using QU fitting. To achieve this goal, we will generate mock data for analysis. We consider 2 types of mock data. First, we consider the simplest case where no sign conversion of RM occurs along each path. Second, we consider the case of the existence of RM structure within the beam (complex case). One path has no sign of conversion of RM, the same as the simple case, and the other path has a sign of conversion of RM. Figure 3.2 and 3.4 show the RM map of the galaxy, where the big black circle indicates the observed beam and the small circles indicate the region that emission passes through. The small circles of Figure 3.2 and 3.4 show simple case and complex case, respectively Figure 3.3 and 3.5 show RM distribution in the beam of the simple case and complex case, respectively. We observe strokes parameter I, Q, U that are the sum of small circles in figure 3.2 (and figure 3.4). Table 3.1 contains the mean and standard deviation of this distribution.

3.3 Results

We investigate whether the RM structure of lensing galaxies can be extracted from the QU spectra. We show the results of estimating the RM structure using QU-fitting with (m1) and without (m2) the requirement of the same polarization angle. At first, the simple case where no sign conversion of RM occurs along each path (case 1). Next, we consider the case of the existence of RM structure within the beam (complex case, case 2). In each case, the two fitting models described in section 3.2.1 are used. In section 3.3.3,

we will calculate various paths and consider what paths this method can be applied to when passing through them. We will examine the extent to which the method can be applied to this statistical result with (m1) and without (m2) the same polarization angle requirement. As in Section 3.2, we select only those that result in two lens images. We consider each path to have an RM screen and fit it with a two-screen model which means we apply Equation 3.2 to each path. Due to the computational cost of fitting, we apply the two-screen model, but it is important as a first attempt because we fit the two-screen model first when applying it to actual observations.

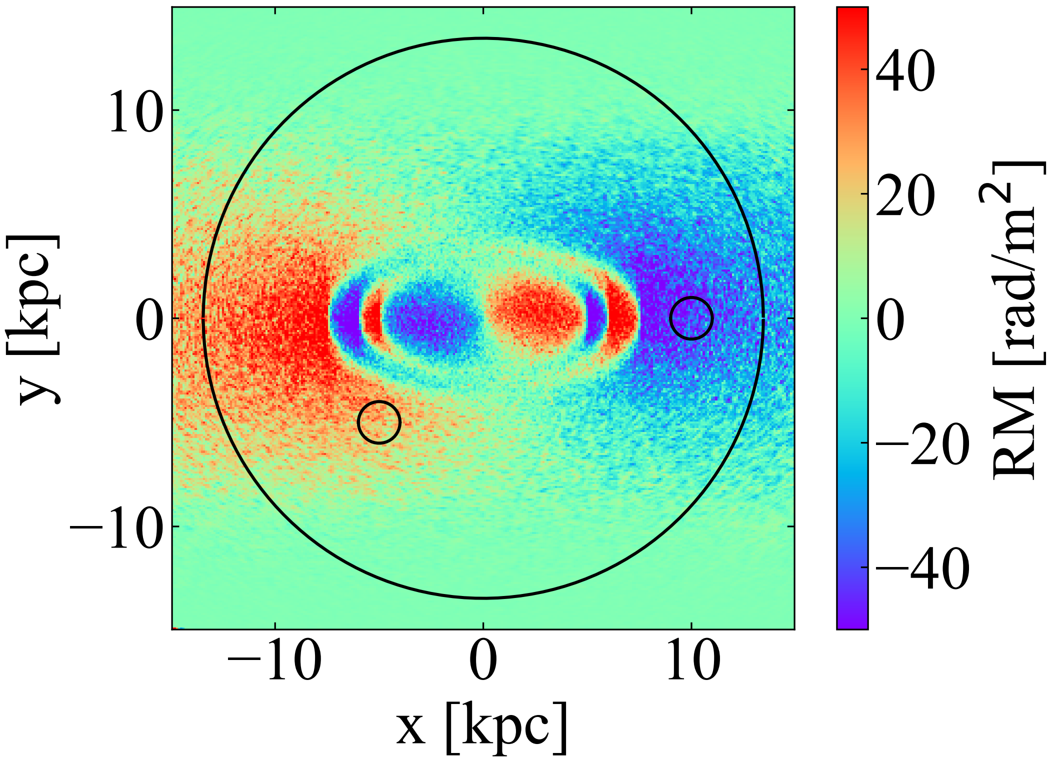

Figure 3.2: RM map of the galaxy, where the big black circle indicates the observed beam and the small circles indicate the region that emission passes through in case of simple case.

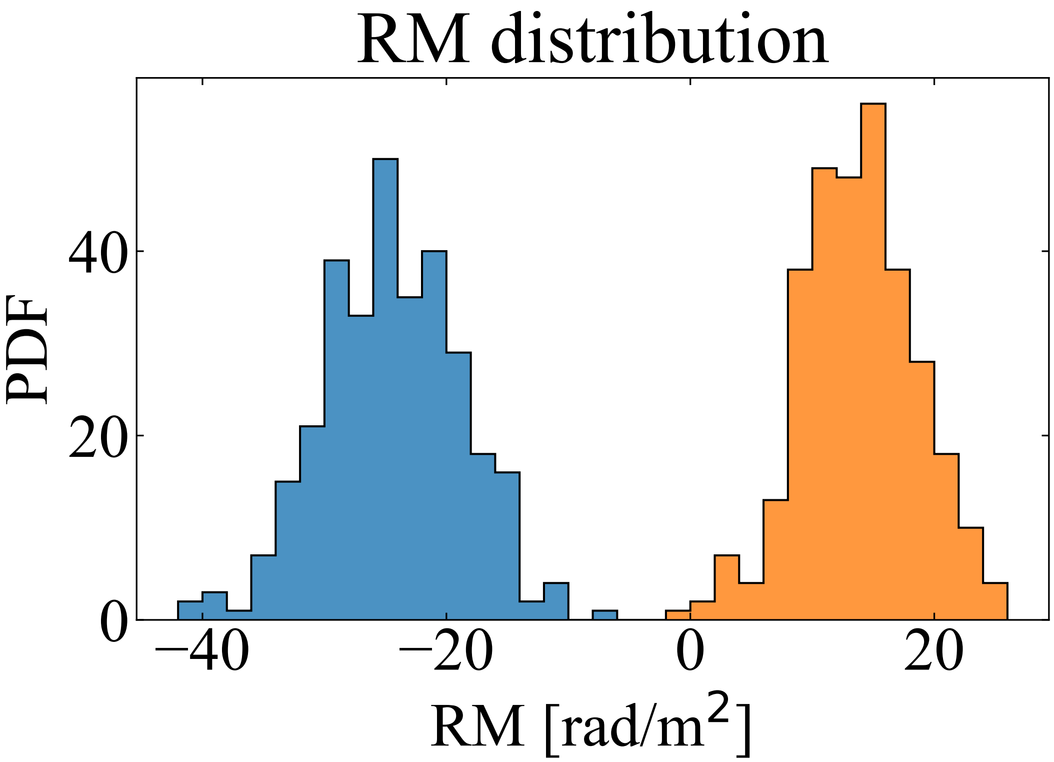

Figure 3.3: RM distribution in the beam of the simple case.

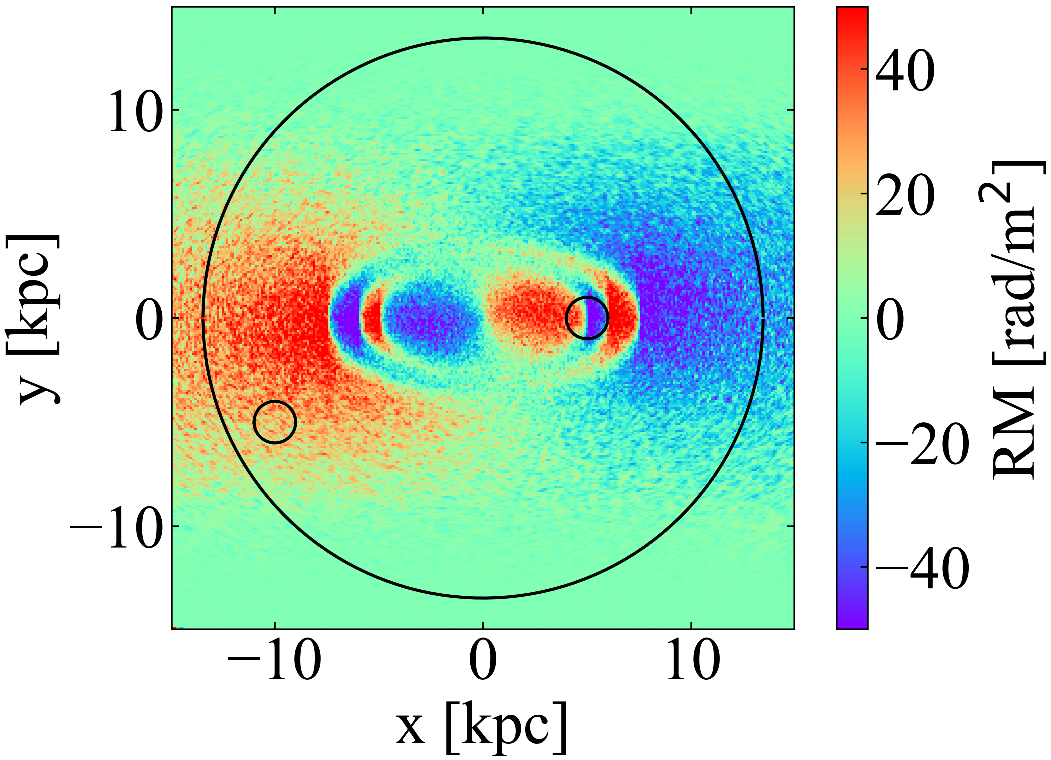

Figure 3.4: RM map of the galaxy, where the big black circle indicates the observed beam and the small circles indicate the region that emission passes through in case of complex case.

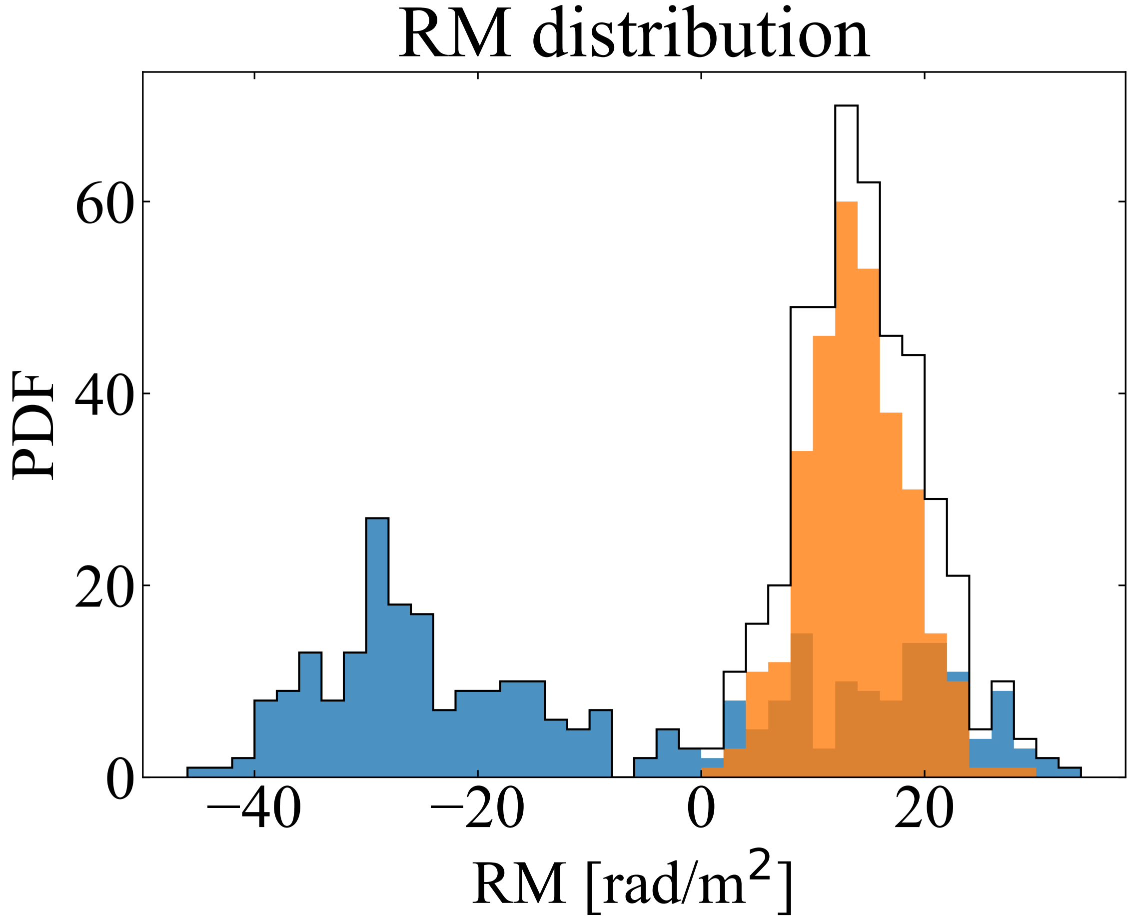

Figure 3.5: RM distribution in the beam of the complex case

Table 3.2: Best fit parameters in the case1

RM_1 (rad/m^2)	σ_{RM_1} (rad/m^2)	RM_2 (rad/m^2)	σ_{RM_2} (rad/m^2)	χ_1 (rad)	χ_2 (rad)
-24.70	5.495	13.70	3.331	0.017	0.012
-24.65	5.600	13.68	3.341	0.014	—

3.3.1 Simple case, case1

We consider each path to have an RM screen and fit it with a two-screen model which means we apply Equation 3.2 to each path. In the case of the m2 model, we apply Equation 3.2 to each path but χ_0 is the same. The table shows the best-fit parameters of both cases. Both models can explain the mock data of the simple case comparing parameters. Figure 3.6 shows the observed QU spectrum and fitted one with the m1 model. As you can see in figure 3.6, fitting data is adapted to observed data well. Figure 3.7 shows the observed QU spectrum and fitted one with the m2 model. The values of RM_1, σ_{RM_1}, and χ_0 are almost the same in the two models and the accuracy is similar. In both cases m1 and m2, we can say that using QU fitting (model fitting), we can obtain the mean and variance of the RM generated in each path, even if they are spatially unresolved. In other words, if there is no RM reversal (magnetic field reversal) in each path, as in case 1, this method can prove the existence of a global magnetic field structure. Furthermore, if we assume an electron number density model as in Mao et al. (2017)[1], we can also estimate the magnetic field strength.

3.3.2 Complex case, case2

We fit the m1 and m2 to the data like the simple case. The table shows the best-fit parameters of both cases. We consider each pathway to have an RM screen and fit it with a multi-screen model. Four-screen model is better in both cases. Figure 3.8 shows the observed QU spectrum and fitted one with the m1 model. As you can see in figure 3.8, fitting data is adapted to observed data well. Figure 3.9 shows the observed QU spectrum and fitted one with the m2 model. The fitted values are then shown in the table 3.3. In the case of m1, we can see physically strange values in the parameters. For example, in the case of m1, one of the best values is $\mathrm{RM}_0 = 4984$, which is a strange value. In addition, the polarization angle is not zero and does not match the mock data. In contrast, in the case of m2, the polarization angle is zero and matches the mock data. Looking at the RM_0 value, it is almost identical to the RM that peaks in Figure 3.5.

Using m2, we find that QU-fitting can be used to estimate the spatially unresolved RM structure, even in complex cases such as case 2. In this calculation, we know from the mock data that one path corresponds to one screen and the other to three screens, but it should be noted that we do not know which path each parameter corresponds

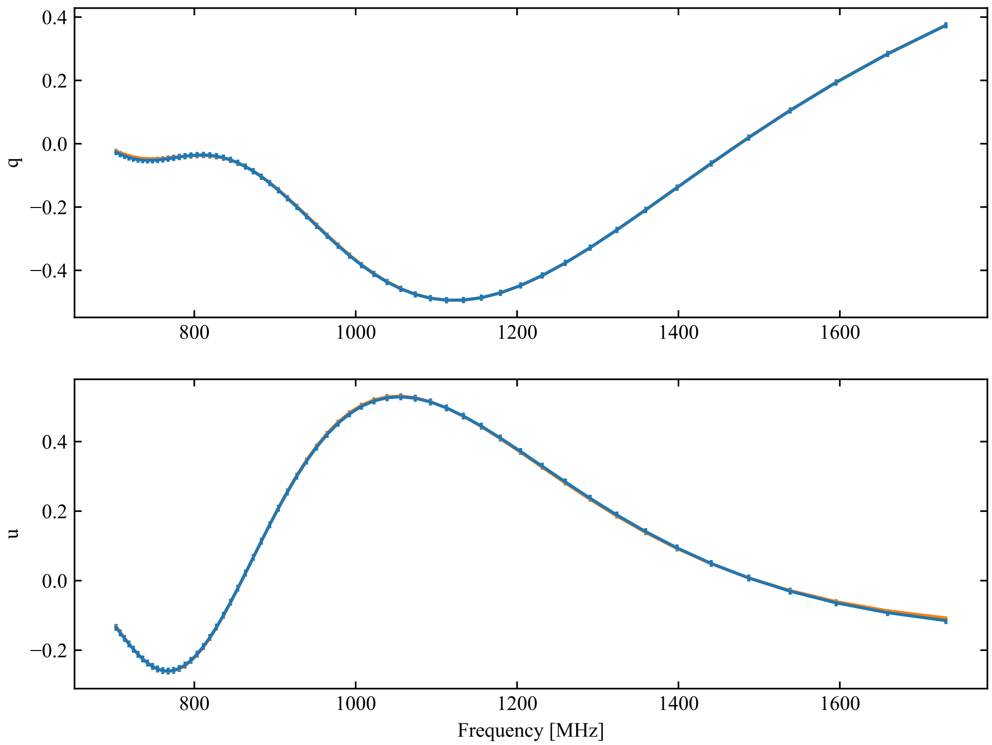

Figure 3.6: The observed QU spectrum and fitted one with the m1 model. Blue: observed data, orange: fitting data using 2 screen model.

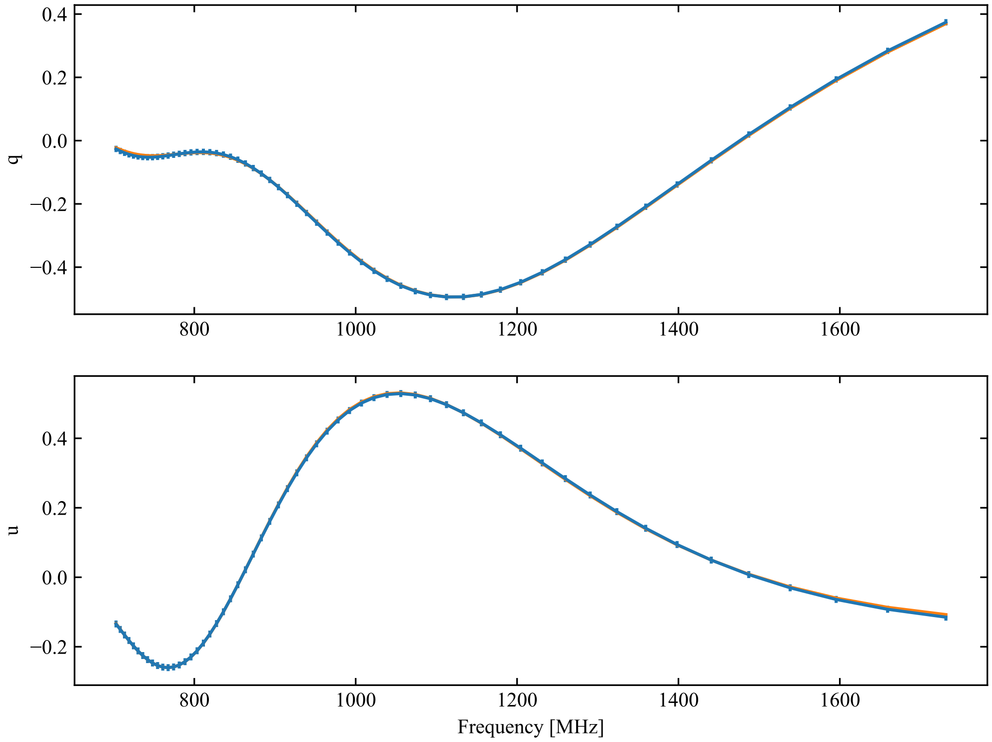

Figure 3.7: The observed QU spectrum and fitted one with the m2 model. Blue: observed data, orange: fitting data using 2 screen model.

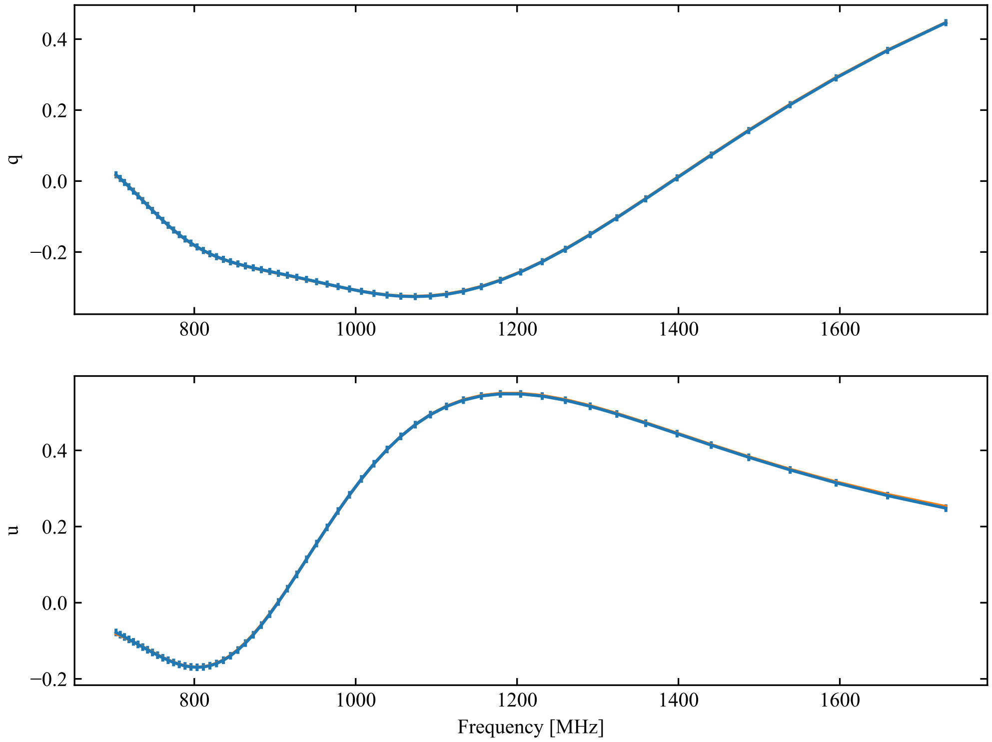

Figure 3.8: The observed QU spectrum and fitted one with the m1 model. Blue: observed data, orange: fitting data using 4 screen model.

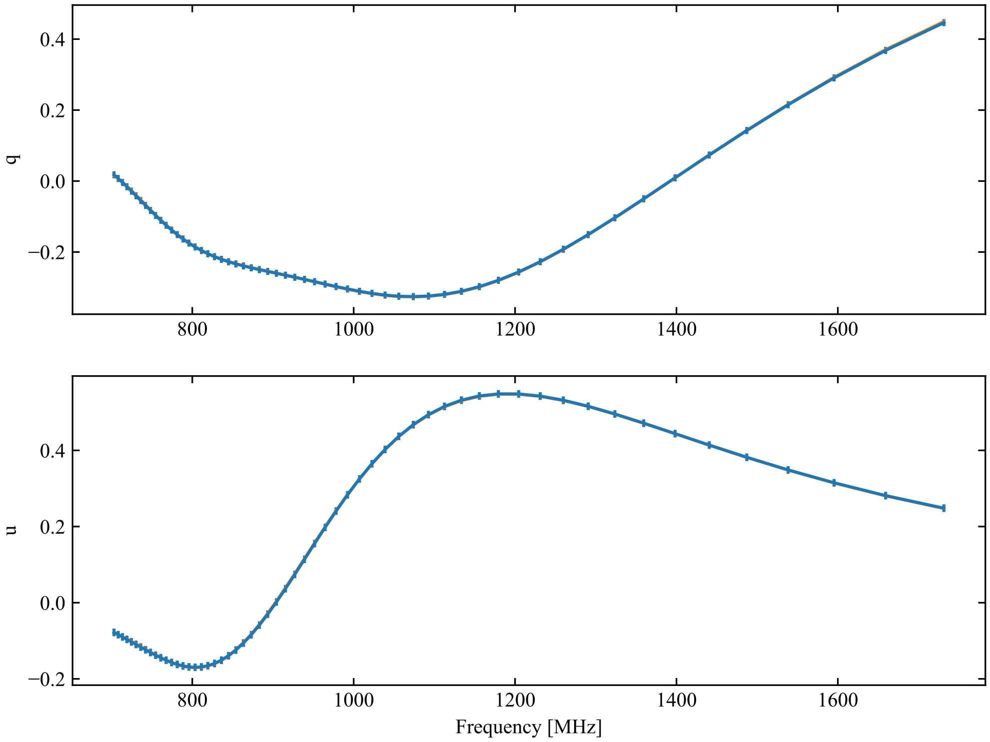

Figure 3.9: The observed QU spectrum and fitted one with the m2 model. Blue: observed data, orange: fitting data using 4 screen model.

to in the actual observation. However, we do know that there is an RM difference for each path, so we know that there is a global magnetic field structure. In other words, if such a fitting is successful for a high-redshift gravitationally lensing galaxy, it suggests the existence of a coherent magnetic field from that redshift galaxy.

3.3.3 Statistical results

The position of the split into two images was fitted with the two-screen models m1 and m2, respectively. To check if the fitting is successful, we examine $\chi^2 < 10$ and $|\phi - \mathrm{RM}| < 3$ with initial polarization angles less than 1 degree, where ϕ is the Faraday depth. The upper row of Figure 3.10 is the result for m1 and the lower row is the result for m2. The left side is the one that satisfies the above conditions, and the right side is the one that does not. In the case of the m1, 8 satisfy the condition, or about 10 percent and 76 do not satisfy the condition, or about 90 percent. In the case of m2, 37 satisfy the condition, or about 44 percent and 47 do not, or about 56 percent. The case of m2 is better than that of m1. We will focus on the cases where the fitting is successful and the cases where it is not. If we focus on the areas that did not go well from Fig. 3.3.2, we can see that the RM inversion (reversal of the magnetic field) is concentrated in certain areas. This is an area that must be fitted with a multiscreen, as can be seen in Section 3.3.2, case2. We can also see that cases like case1 in Section 3.3.1 tend to work well. However, it is important to note that m2 is more accurate than m1, even in cases like case1. To see where this difference comes from, consider the case where the accuracy of the polarization angle is not evaluated for m1. Then, we check m1 with $\chi^2 < 10$ and $|\phi - \mathrm{RM}| < 3$. There are 49 percent that satisfy these. This is close to the percentage (44 percent) for which m2 satisfies $\chi^2 < 10$ and $|\phi - \mathrm{RM}| < 3$ and the condition that the polarization angle is less than 1 degree. Thus, this result shows that the accuracy of the polarization angle is not particularly good for m1.

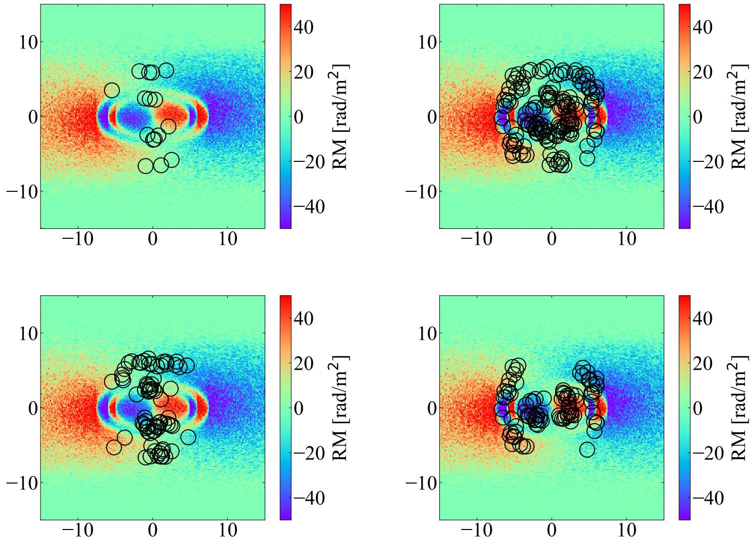

Figure 3.10: The upper row is the result for m1 and the lower row is the result for m2 in the case of the Einstein radius of the mass model of the lensing galaxy is 1”. The left side is the one that satisfies the above conditions, and the right side is the one that does not.

Table 3.3: Best fit parameters in the case2

RM_1 (rad/m^2)	σ_{RM_1} (rad/m^2)	RM_2 (rad/m^2)	σ_{RM_2} (rad/m^2)	RM_3 (rad/m^2)	σ_{RM_3} (rad/m^2)	RM_4 (rad/m^2)	σ_{RM_4} (rad/m^2)	χ_1 (rad)	χ_2 (rad)	χ_3 (rad)	χ_4 (rad)
-15.46	0.57	4984	433.369	-32.62	1.32	-24.70	5.495	-0.28	-1.46	0.014	0.106
13.2	3.7	-30.0	5.61	-16.7	8.48	17.6	6.60	0.00	—	—	—

Table 3.4: Best fit parameters in the case that the background source has two RM components

RM (rad/m^2)	σ_{RM} (rad/m^2)	χ_0 (rad)
-23.76	5.83	0.00
26.24	5.812	0.6998

3.4 Discussion

In the section 3.3, when two peaks appear on the FDF, it is not possible to distinguish whether the source has two RM components or whether a source with one RM element is split into two by the lens. We will discuss whether they can be distinguished using the method in this chapter. We investigate whether it is possible to distinguish between background sources and galaxies when sources with different intrinsic polarization angles and different RMs pass through the same region (one region).

We also discuss the extent to which QU-fitting can be applied when the gravitational potential is changed.

3.4.1 Differences in initial polarization angles and RM

The background source has two RM components, $(\mathrm{RM}_0, \chi_0(\mathrm{rad})) = (0, 0)$, $(50, 0.698)$. Suppose background source passes through a region with $\mathrm{RM} = -23.72, \sigma_{\mathrm{RM}} = 5.965$ (Figure 3.11). When background source with $(\mathrm{RM}_0, \chi_0[\mathrm{rad}]) = (0, 0)$, $(50, 0.698)$ passes through the region, we get $Q1$ and $U1$, $Q2$ and $U2$, respectively. We sum up $Q1$ and $Q2$ ($U2$ and $U2$) values for the projected grids that the background emission passes through and obtain the observed Q_{sum} and U_{sum}. Figure 3.12 shows each QU spectrum. We discuss whether we can distinguish between two background sources, each with different polarization angles and RMs. If the background radiation passes through the foreground region with $\mathrm{RM} = -23.72, \sigma_{\mathrm{RM}} = 5.965$, then we should get $(\mathrm{RM}_0, \sigma_{\mathrm{RM}}, \chi_0[\mathrm{rad}]) = (-23.72, 5.965, 0), (26.28, 5.965, 0.698)$ from the QU spectrum. We fit the m1 to the data. The table 3.4 shows the best-fit parameters. As can be seen from the table, QU fitting can be used to distinguish between background sources with two RM elements when they pass through the same area with RM distribution (one area). If two RM components in the FDF have different polarization angles of the background source, the RM components can be distinguished as originating from the background source.

3.4.2 Identification of well-fitting paths

Referring to section 3.3.3, the most successful cases are those in which no magnetic field reversal occurs in the field of view, while the least successful cases are those in which

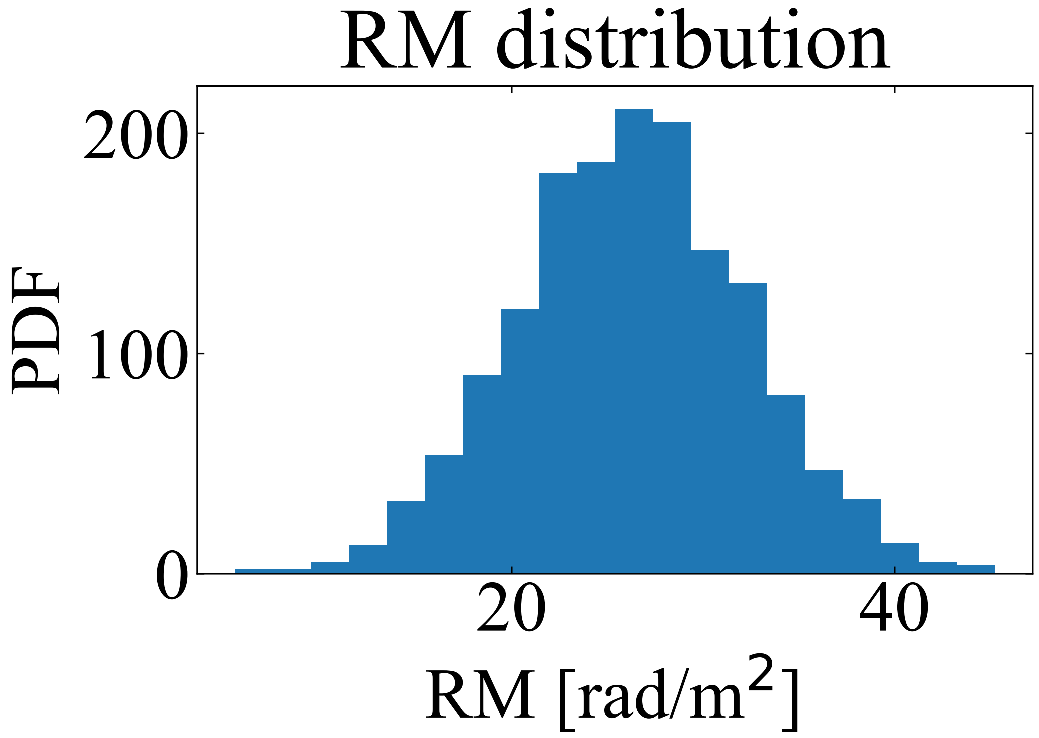

Figure 3.11: RM distribution in the region which background source passes through.

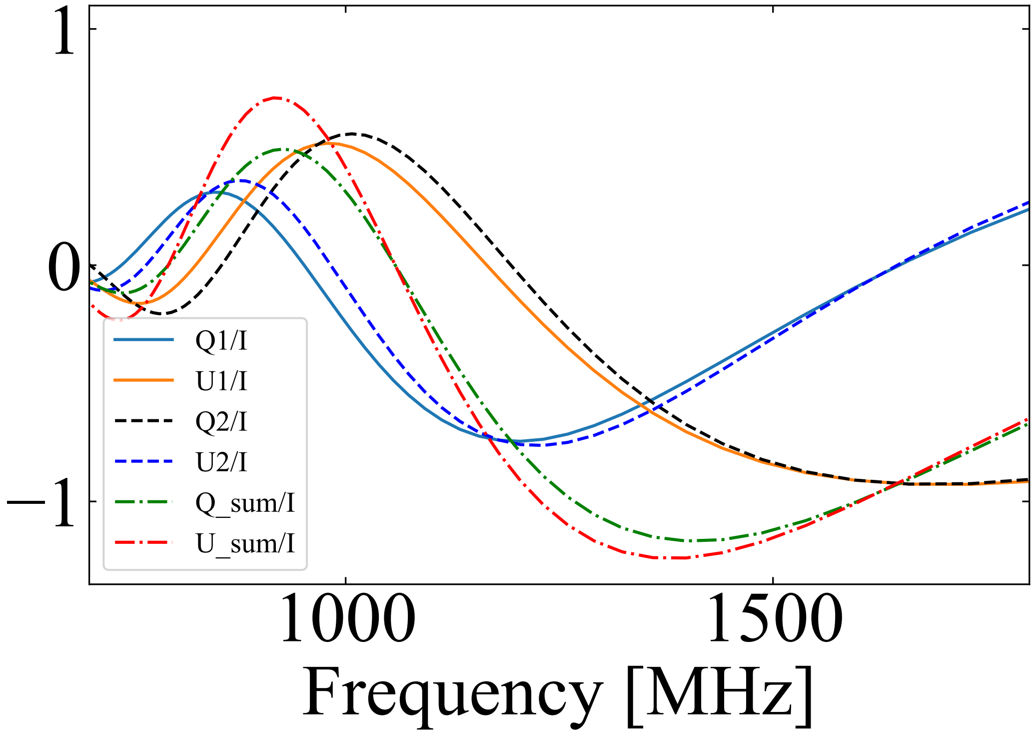

Figure 3.12: QU spectrum. Blue solid line: Q1/I, Red solid line: U1/I, Blue dashed line: Q2/I, Red dashed line: U2/I, Bule 1-dot dashed line: Q_{sum}/I, Red 1-dot dashed line: Q_{sum}/I.

magnetic field reversal occurs. This is because, as shown in Section 3.3.2, when there is a magnetic field inversion, fitting must be performed on multiple screens. It is clear that this does not work well when the foreground is complex. Thus, if the two-screen model does not fit well, multiple screens are needed.

We consider Einstein radius to be larger than in the case of section 3.3.3. When Einstein radius is larger, there are cases that the paths do not pass through the magnetic field reversal region. Fig 3.13 shows the result for m1 and the lower row is the result for m2 with Einstein radius at 1.5". The left side is the one that satisfies the above conditions, and the right side is the one that does not. In the case of the m1, 7 satisfy the condition, or about 7 percent and 98 do not satisfy the condition, or about 93 percent. In the case of m2, 53 satisfy the condition, or about 50 percent and 51 do not, or about 49 percent. As in Section 3.3.3, the case of m2 is better than that of m1. Focusing on the areas that fit well shows that many of them have no RM reversal (magnetic field reversal). In contrast, focusing on where things are not going well is when the RM passes through an area that is inverted as in Section 3.3.3. However, there are other cases where things are not going well. This is the case if there are two paths through the region causing the same degree of RM. The polarization rotates the same amount on each path, so they are indistinguishable. We note that the pathway is potential-dependent.

Based on these, if the two-screen model fits well, then the two paths have different RMs. In other words, the galaxy has coherent magnetic field structure.

3.5 Conclusion

We focused on using strong gravitational lensing to observe distant galaxies. In the next few years, we expect to find many polarization sources affected by gravitational lensing. However, current radio interferometers can't resolve gravitational lensed images.

We investigated whether it is possible to extract the RM structure of spatially unresolved lensing galaxies from Faraday spectra. Even if the background polarization source is not resolved, the Faraday depth difference appears when using Faraday tomography. Using QU-fitting (model fitting), get the mean and variance of the RMs experienced by each path, even if they were spatially unresolved. In the case of gravitational lensing objects, we can require that the polarization angle of the background polarization source is the same. We can reduce one parameter. In the case of the existence of RM structure within the beam (complex case), using the model that has multi-components of RM, we compared the observed spectrum with the model spectrum. In the case of imposing this requirement, we found the model which has multi-components of RM is the best fitting model. The polarization angle of the background polarization source is the same as the given angle and we resolve uncertainty about the polarization angle. We could separate complex RM structures of unsolved sources. We calculated many paths and examined what paths the method could be applied to when they passed through. We considered only those that resulted in two lens images being

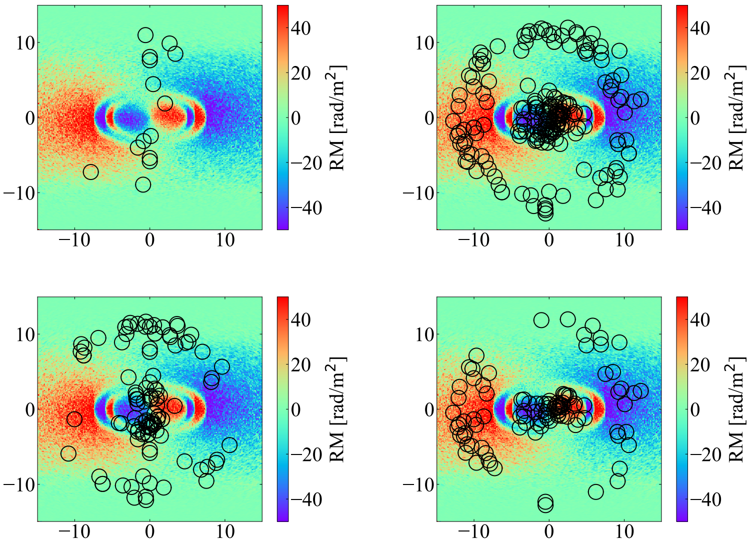

Figure 3.13: The upper row is the result for m1 and the lower row is the result for m2 in the case of the Einstein radius of the mass model of the lensing galaxy is 1.5”. The left side is the one that satisfies the above conditions, and the right side is the one that does not.

selected, and two screens were adapted as the screen model. The results showed that the method can be successfully applied when the polarization passes through each path where there is no RM reversal and that it is difficult when there are RM reversals. It was also found that the model works better when conditions regarding the polarization angle are imposed. The other case where it could not be applied was when the two paths experienced the same Faraday rotation.

We show that the RM structure can be extracted even in the spatially unresolved case for the first time in the world. It is possible to prove the existence of a coherent magnetic field structure.

Chapter 4

Discussion

4.1 Estimation of the galactic magnetic field

From model fitting to a Faraday spectrum, we can estimate the Faraday depth (RM), the variance of the Faraday spectrum (σ_{RM}), and third and fourth order moment quantities such as skewness and kurtosis of the spectrum (ΔRM). The following is an example of the estimation of the spectra. In this study, σ_{RM} corresponds to the variance of the RM in the beam, and ΔRM is the gradient of the global RM in the beam.

The strength of the global and turbulent magnetic fields can be estimated from σ_{RM} assuming the magnetic field model and electron number density. Assuming that the turbulent magnetic field is uniformly isotropic turbulence, using the random walk approach, the variance of the RM in the beam is equal to the variance of the RM in one path if it is a random walk. The σ_{RM} can be written as $\sigma_{\mathrm{RM}} = 0.821 B_{r\parallel} n_e N^{1/2}$ [31], where $B_{r\parallel} = \sqrt{1/3} B_r$ for the intensity of the isotropic turbulent field [μG], n_e is the electron density [cm^{-3}] in cells of size d [pc], $N = Lf/d$ is the number of cells along line of sight L [pc] with volume filling factor f and It is. Let $\langle n_e \rangle = n_e/f$ be the average electron number density

$$\sigma_{\mathrm{RM}} = 0.821 B_r \langle n_e \rangle \sqrt{Ld/f} \tag{4.1}$$

is obtained. Since the model used in this study is a uniformly isotropic turbulent field, and the electron number density is dependent only on the height direction, σ_{RM} should be constant for any path. However, the model σ_{RM}s (table 3.1) are different. This is because there is a global RM structure (ΔRM) in the beam, so σ_{RM} is different. It is possible that the ΔRM behaves as an anisotropic turbulence in the beam. In previous studies, it has been found that the global magnetic field component is involved in the skewness and kurtosis of the Faraday spectrum. It is important to investigate the relationship between ΔRM, skewness and kurtosis in the future.

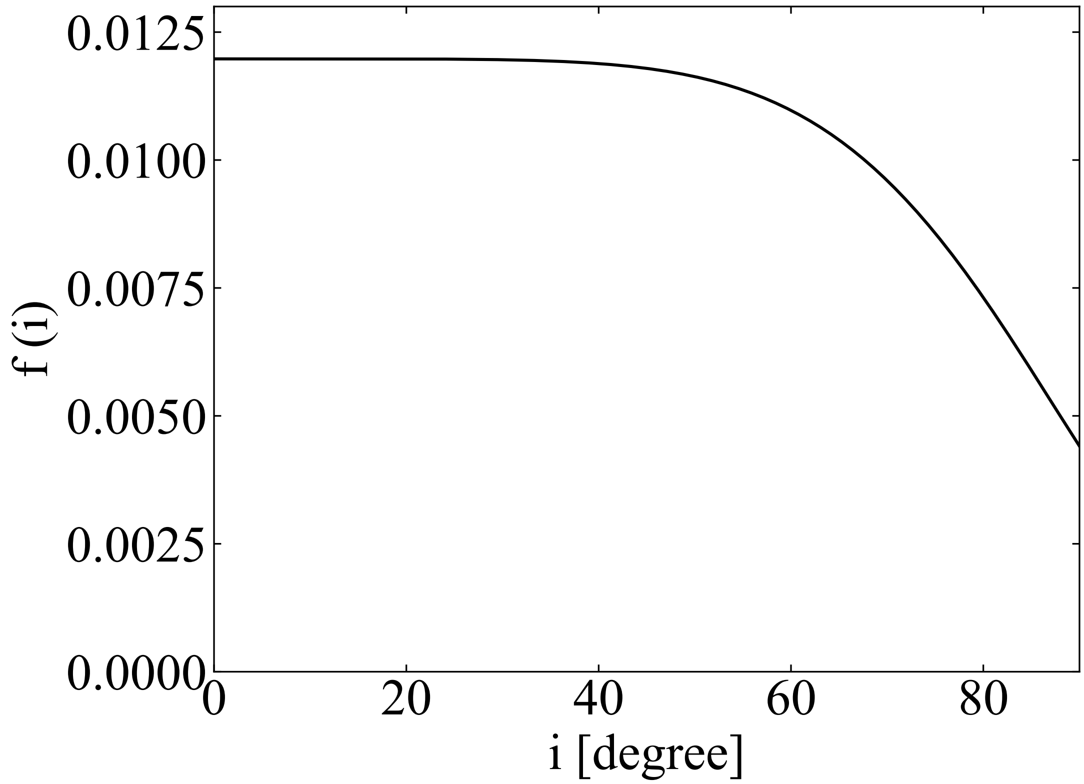

Figure 4.1: Modified distribution of inclination angle of galaxies given by Equation 4.2

4.2 Detection probability of inclination angles

As we discussed the validity of the uniform distribution of galaxy inclination angles in chapter 2, we should consider the dependence of the detection probability for inclination angles. Since face-on galaxies have a relatively large projected area in the sky, the probability of overlapping a quasar behind them is higher than for heavily inclined galaxies. We test how the RMs vary for a different assumption of the distribution of inclination angles. We model the distribution of inclination angles [115] as in

$$f(i) = \frac{6}{i_{\max}\Gamma(1/6)} \exp\left\{-(i/i_{\max})^6\right\}. \tag{4.2}$$

Figure 4.1 shows a modified distribution of inclination angles for $i_{\max} = 90^\circ$ so that galaxies with lower inclination are given priority.

The observed RM is always $1/(1+z)^2$ times the intrinsic value because RM is proportional to the square of the wavelengt. According to the Monte Carlo simulations in chapter 2, the DING contribution to the standard deviation of the observed RM is

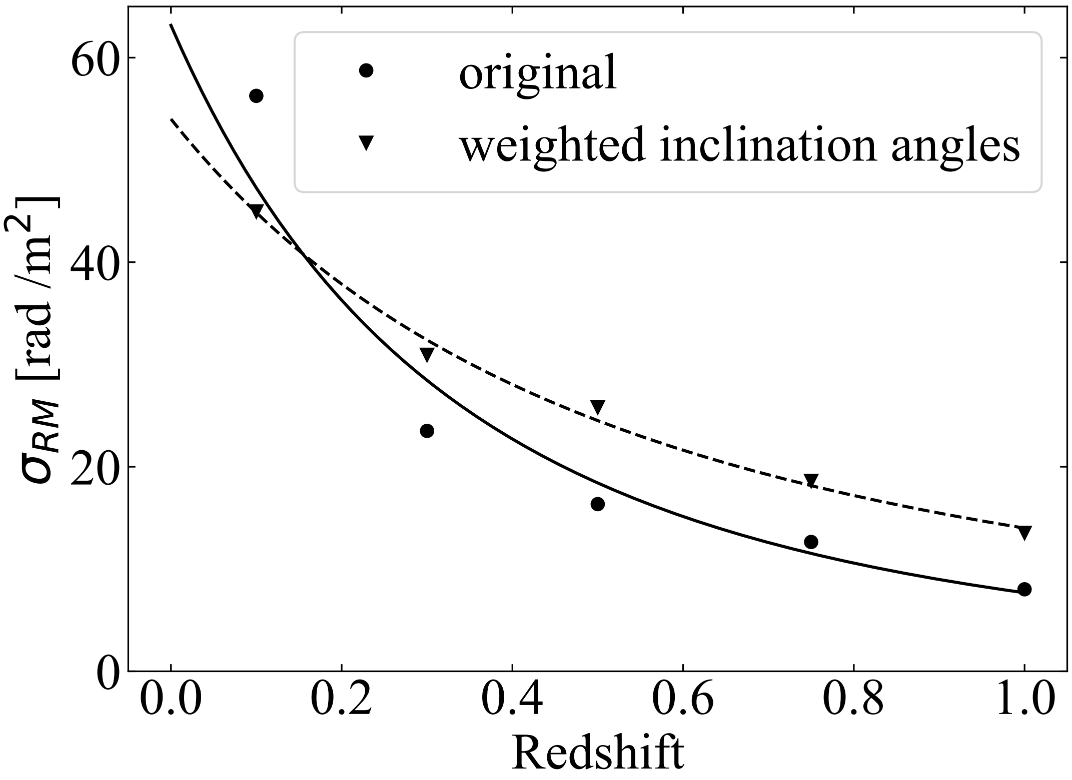

Figure 4.2: Standard deviation of $\mathrm{RM}_{\mathrm{peak}}$, σ_{RM}, as a function of the redshift, z. The circles and triangles, respectively, show the results of our fiducial runs and our control runs for which we weighted by inclination angles. The solid and dashed lines are the best least-square fit, assuming the power-law, for our fiducial and control runs, respectively.

$\sigma_{\mathrm{RM}} \propto 1/(1+z)^k$ and $k \sim 2.7$, which is steeper. The reason for the large value of k is caused by the increase in physical beam size and the rapid decrease in filling factor in the edge-on case. The best fit (dashed line) in Figure 4.2 shows the results weighted by inclination angles. The values are $A \sim 54$ and $k \sim 1.9$, which is consistent with the $1/(1+z)^2$ dependency. Therefore, it can be suggested that a polarization source passing through an intervening galaxy is more likely to observe an RM experienced by the intervening galaxy.

The probability that the observed RM has a value (i.e., passes through the intervening galaxy) is about 78% when the inclination angle is 30°, about 53% when the angle is 60°, and about 14% when the angle is 90°. Furthermore, if the distribution of inclination angles (Equation 4.2) is also considered, it is about 58%. The size of the galaxy in this paper is about 10 kpc radius. This means that by restricting the impact parameter to 10 kpc in actual observations, the RM of the intervening galaxy can be observed with a probability of about 58%. This is also true for gravity lenses.

Next, consider the effect of the error of the inclination angle on the RM estimation. If the magnetic field is a ring field, the line-of-sight magnetic field is given by

$$B_{\|} = -B_0 \cos\theta \sin i \tag{4.3}$$

where θ is the azimuthal angle and i is the iclination angle. We also assume that the electron number density is in a disk of uniform thickness, h_{ion}. For a line of sight at an inclination angle i with respect to the sky plane, the optical path length through the disk is $\mathrm{L} = h_{\mathrm{ion}}/\cos i$. From this, RM can be written in

$$\mathrm{RM} = -0.81 B_0 n_0 h_{\mathrm{ion}} \tan i. \tag{4.4}$$

Considering the error δ in the inclination angle, the line-of-sight direction RM can be written as

$$\mathrm{RM} = -0.81 B_0 n_0 h_{\mathrm{ion}} \tan{(i+\delta)}. \tag{4.5}$$

From this, the impact of the error δ of the inclination angle on the estimated RM increases as i increases, but the probability of a large inclination angle is decreased shown in Equation 4.2. Thus, it is unlikely that our approximation has a large impact on the results.

4.3 Future observation of galactic magnetic fields

This thesis focuses on one of the open questions regarding the galactic magnetic field: the cosmological evolution of the galactic magnetic field. It is expected that the small-scale magnetic field is genarated quickly by turbulence [71], while the global magnetic field is constructed over a long time (about the rotational period of a disk) [72]. According to numerical experiments [73], if a kpc-scale magnetic field of μG intensity is generated in a galactic disk at $z = 2$, it will take up to $z = 0.5$ for it to grow into a galaxy-scale aligned magnetic field.

During that time, especially from redshift $z = 2$ to the present, when star formation has been active, the effects of star formation will also be important. Direct observation of magnetic fields at the distant galaxy over $z \sim 2$ give us the evidence how magnetic fields affect the cosmological evolution, and upcoming SKA with high sensitivity and wide field-of-view, will provide us that information. In this study, we reported the observation of distant galactic magnetic fields by using two methods. One is to investigate whether the magnetic field information can be extracted from the effects of intervening galaxies when observing distant polarization sources, and the other is to investigate whether the RM structure of lensing galaxies can be extracted when polarization waves are observed due to gravitational lensing effects. The results show that it is possible to extract the magnetic field information even when direct observation of the galaxies is not possible.

However, the present study does not include redshift dependence in the magnetic field model and does not show how the observed results are obtained until the magnetic field grows into a galaxy-scale aligned magnetic field. Future studies are needed to investigate how the magnetic field model behaves with redshift dependence (evolutionary model). We also believe that this study can be applied to elliptical galaxies. For example, if we can observe elliptical galaxies that may still have the initial dynamo magnetic field as a gravitational lensing object, and if the RM varies with position, it means that there is a small amount of global magnetic field, and we can provide feedback to the turbulent dynamo theory. Shah & Seta (2021)[116] examined the possibility of detecting RMs in elliptical galaxies using background sources. They summarized that σ_{RM} is $4 - 30$ [rad/m^2] and observable in POSSUM when the intensity of the background source is 14.7 - 440 μJy and the polarization ratio is 75%.

4.4 Impact on other fields

This study has great significance for the theory of galaxy magnetic field evolution. This study is expected to obtain global magnetic field strength and turbulent magnetic field strength of distant galaxies, which will provide new constraints on the theory of the evolution of the galactic magnetic field. In addition, if elliptical galaxies, which may still have the initial dynamo magnetic field, can be observed as gravitational lensing sources, feedback can be provided to turbulent dynamo theories. If the polarized radiation of background sources passes through the CGM region due to the gravitational lensing effect, individual CGM magnetic fields can be obtained; although the observation of CGM magnetic fields has been limited to a limited extent, new knowledge will be obtained through this study. Combining the obtained CGM magnetic field distribution (spread and bias) with visible light observations of the outflow of metallic elements into intergalactic space will provide new insights into the chemical evolution of intergalactic material in terms of the transport of metallic elements produced in the galactic interior. Observations on cosmological magnetic field evolution have been made to measure the magnetic field from the polarization properties of high-redshift sources (e.g., [117]). However, it has been reported that the presence of an intervening galaxy in the line of sight of the polarization source can affect the observation results (e.g., [118]). Therefore, this study can provide magnetic field information and models to remove the influence of intervening galaxies, which should be useful for understanding cosmological magnetic field evolution.

Chapter 5

Summary

This thesis focuses on one of the unsolved problems regarding the galactic magnetic field: the cosmological evolution of the galactic magnetic field. To solve this problem, it is necessary to observe the magnetic fields of distant galaxies. We investigated whether the magnetic field information can be extracted from the effects of intervening galaxies when observing distant polarization sources.

First, in order to determine the contribution of intervening galaxies to the observed results, we investigated the effect of intervening galaxies on the observed polarization when they are in the line of sight. The main results are summarized below.

- Depolarization by the intervening galaxies strongly depends on the inclination angle of the intervening galaxies, and the more edge-on the galaxies are, the larger the RM and the stronger the depolarization is. On the other hand, when the proportion of intervening galaxies in the beam becomes smaller, the proportion of the region where the polarization of the intervening galaxies and the background source do not overlap increases, resulting in a smaller RM and weaker depolarization.

- The Faraday spectra represent the RM structure in the beam region, and the information in the beam can be extracted, showing the possibility of detecting magnetic fields that cannot be extracted by conventional methods.

- We found that the number of spectral peaks increases with the presence of an intervening galaxy in the line of sight when observing a polarized source.

- Monte Carlo simulations with the parameters of the inclination angle and the central position of the beam showed a redshift dependence in the standard deviation of the observed RM. The dependence depends on the redshift dependence of wavelength and the inclination angle.

Next, we turned our attention to a method that uses strong gravitational lensing as an observation of intervening galaxies. In this method, since the background polarization sources that are subject to the gravitational lensing effect are the same, the effect of the background polarization sources can be ignored, and the focus can be on the magnetic field of the galaxy itself. However, recent radio interferometers cannot spatially resolve objects subjected to gravitational lensing effects. Therefore, we investigated whether it is possible to extract the RM structure of spatially unresolved lensing galaxies from Faraday spectra. The main results are summarized below.

- Even if the background polarization source is not resolved, the Faraday depth difference appears when using Faraday tomography.
- Using QU-fitting (model fitting), get the mean and variance of the RMs experienced by each path, even if they were not spatially resolved.
- In the case of the existence of RM structure within the beam (complex case), using the model that has multi-components of RM, we compared the observed spectrum with the model spectrum. In the case of gravitational lensing objects, we can require that the polarization angle of the background polarization source is the same. We can reduce one parameter. In the case of imposing this requirement, we found the model which has multi-components of RM is the best fitting model. The polarization angle of the background polarization source is the same as the given angle and we resolve uncertainty about the polarization angle. We could separate complex RM structures of unsolved sources.

In order to clarify the contribution of intervening galaxies to the observed results, we investigated the effect of intervening galaxies on the observed polarization when they are in the line of sight. We found that the RM structure in the beam is reflected in the FDF. This allows us to examine the existence of a global magnetic field in the galaxy by the FDF. We were the first in the world to show that the RM structure can be extracted even in the spatially unresolved case by a method using gravitational lensing. In other words, it is possible to prove the existence of a global magnetic field structure. Since these methods are observable even at a distance, we can observe when and how large the global magnetic field exists in a galaxy. The galactic magnetic field model used in this thesis does not apply redshift dependence (evolution). Future simulations that apply these dependence will allow us to investigate in detail which redshifts can be observed.

Appendix A

Appendix

A.1 Polarization observation Stokes parameter

Radio waves from celestial objects are represented as a superposition of electromagnetic waves with various phases and intensities. Electromagnetic waves in which the oscillation direction of the electric field is biased in a certain direction are called polarized waves. Polarization is an important element in magnetic field observation because it allows us to determine the direction of the cosmic magnetic field. Here, we explain the basic properties of polarized waves and the Stokes parameter, which is an observable quantity.

The direction of propagation of a plane wave with a single frequency is the z-axis, and the x-axis and y-axis are on the plane of vibration. If $\mathbf{x}$ and $\mathbf{y}$ are the unit vectors in the x-axis and y-axis directions, respectively, the electric field $\mathbf{E}$ of a plane wave can be expressed as

$$\mathbf{E} = \mathrm{Re}\left[(E_1 e^{i\delta_1}\mathbf{x} + E_2 e^{i\delta_2}\mathbf{y})e^{i(\omega t - kz)}\right]. \tag{A.1}$$

The x and y components of the electric field $\mathbf{E}$ are

$$E_x = E_1 \cos(\omega t - kz + \delta_1) \tag{A.2}$$

$$E_y = E_2 \cos(\omega t - kz + \delta_2), \tag{A.3}$$

where ω is the angular frequency, k is the wave number, and δ_1 and δ_2 are the phases of the x and y components. The trajectory of the electric field is (Fig A.1)

$$\left(\frac{E_x}{E_1}\right)^2 + \left(\frac{E_y}{E_2}\right)^2 - 2\frac{E_x E_y}{E_1 E_2}\cos\delta = \sin\delta^2, \tag{A.4}$$

where $\delta = \delta_1 - \delta_2$. Polarization behaves differently for E_1 and E_2 and phase difference δ. For example, when $E_1 = E_2$ and $\delta = \pi/2$, the electric field rotates leftward toward the direction of the radio wave. This is called left circular polarization. When $\delta = -\pi/2$, it rotates rightward and is called right circularly polarized. When either E_1 or E_2 is

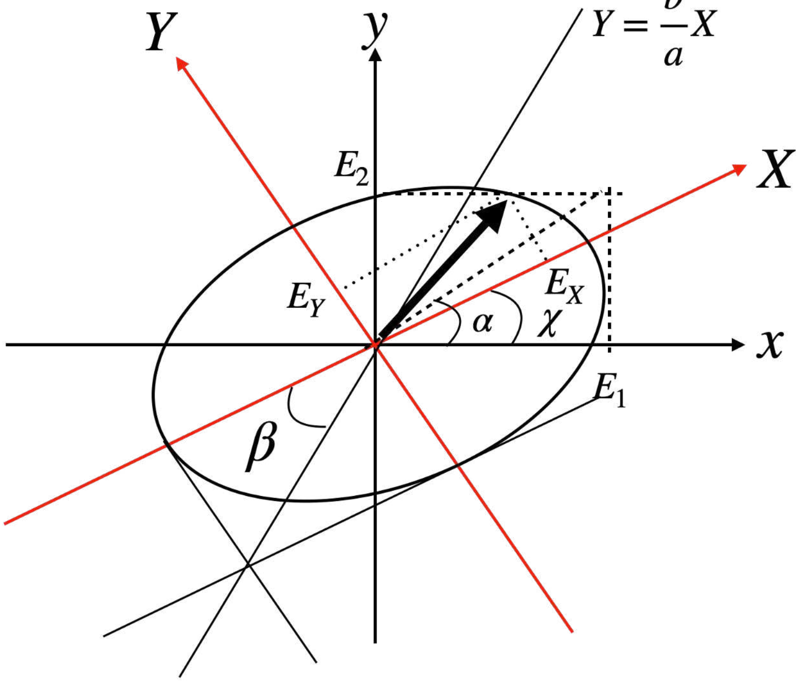

Figure A.1: Schematic figure of elliptical polarization zero or $\delta = n\pi$, the electric field oscillates in one direction and is linearly polarized. In other cases, the wave is elliptically polarized.

For elliptical polarization, let the X-axis be the major axis of the ellipse and the Y-axis be the minor axis, and the projected component of the electric field $\mathbf{E}$ is

$$\left(\begin{array}{c} E_X \\ E_Y \end{array} \right) = \left(\begin{array}{cc} \cos\chi & \sin\chi \\ -\sin\chi & \cos\chi \end{array} \right) \left(\begin{array}{c} E_x \\ E_y \end{array} \right), \tag{A.5}$$

where χ is the angle between the x-axis and the X-axis ($0 \leq \chi \leq \pi$). If the length of the major axis of the ellipse is $2a$ and the length of the minor axis is $2b$, then

$$\begin{cases} a^2 + b^2 = E_1^2 + E_2^2 \\ \tan 2\chi = \tan 2\alpha \cos\delta \\ \sin 2\beta = \sin 2\alpha \sin\delta \end{cases} \tag{A.6}$$

holds, where $\tan\alpha = E_2/E_1 (0 \leq \chi \leq \pi/2)$、$\tan\beta = \pm b/a$.

Since radio wave strength is measured in actual observations, it is very convenient to express the polarization information in terms of radio wave strength. This value is called the Stokes parameter. Let us consider the case of perfect polarization and define the Stokes parameter as follows.

$$\begin{cases} I & = E_1^2 + E_2^2 \\ Q & = E_1^2 - E_2^2 = I \cos 2\beta \cos 2\chi \\ U & = 2E_1E_2 \cos\delta = I \cos 2\beta \sin 2\chi \\ V & = 2E_1E_2 \sin\delta = I \sin 2\beta \end{cases} \tag{A.7}$$

I is the intensity of the radio wave. The Q shows the dominance of the x-axis component of linear polarization over the y-axis component. The U shows the dominance of the linearly polarized wave component in the direction of the axis tilted $\pi/4$ from the x-axis over the linearly polarized wave component in the axis perpendicular to that axis. Also, V indicates how dominant the right circularly polarized component is over the left circularly polarized component. Based on the above characteristics, Q and U are linearly polarized components and V is the circularly polarized component. The relations

$$I^2 = Q^2 + U^2 + V^2 \tag{A.8}$$

$$\chi = \frac{1}{2} \arctan\left(\frac{U}{Q}\right) \tag{A.9}$$

are established for these parameters. Hereafter, the χ is called the polarization angle.

Polarized waves in nature are not perfectly polarized and contain unpolarized waves that randomly vary in amplitude and phase. The electric field of a radio wave containing both polarized and unpolarized components can be expressed as

$$E_x(t) = E_1(t)\cos\left[\omega t - kz + \delta_1(t)\right] \tag{A.10}$$

$$E_y(t) = E_2(t)\cos\left[\omega t - kz + \delta_2(t)\right]. \tag{A.11}$$

If the observation time is long compared to the time-varying scale of amplitude and phase, what we obtain in actual observation is a time-averaged $\langle E(t)^2\rangle = \frac{1}{T}\int_0^T E(t)dt\,(T \gg 1/\omega)$.

The Stokes parameters are

$$\begin{cases} I &= \langle E_1(t)^2\rangle + \langle E_2(t)^2\rangle = I_U + I_P \\ Q &= \langle E_1(t)^2\rangle - \langle E_2(t)^2\rangle = I_P\cos 2\chi \\ U &= 2\langle E_1(t)E_2(t)\cos\delta(t)\rangle = I_P\sin 2\chi \\ V &= 2\langle E_1(t)E_2(t)\sin\delta(t)\rangle, \end{cases} \tag{A.12}$$

where I_U represents the unpolarized component and I_P the polarized component. At this time $I^2 \geq Q^2 + U^2 + V^2$ holds. In addition, the polarization factor P is defined as the value that expresses the degree of polarization as follows.

$$p = \frac{\sqrt{Q^2 + U^2 + V^2}}{I}. \tag{A.13}$$

Since the circular polarization component is very small and negligible in the actually observed polarization, it is sufficient to consider only the linear polarization component, and the dgree of polarization can be written as

$$p = \frac{\sqrt{Q^2 + U^2}}{I}. \tag{A.14}$$

When considering only linear polarization, polarization may be described in the complex plane with Stokes parameters Q and U. The polarization rate on the complex plane can be expressed as:

$$pe^{2i\chi} = \frac{I_P}{I}e^{2i\chi} = \frac{I_P}{I}(\cos 2\chi + i\sin 2\chi) = \frac{Q + iU}{I} = \frac{P}{I}. \tag{A.15}$$

The P is called the polarization intensity and $P = Q + iU$.

A.2 Synchrotron radiation mechanism

Synchrotron radiation is observed from active objects where high-energy electrons are present. Synchrotron radiation is electromagnetic radiation produced by the motion of high-energy electrons in a magnetic field and the bending of their orbits. Synchrotron radiation is observed in a wide frequency range from radio waves to γ rays. Radio waves observed in radio galaxies are synchrotron radiation, and active galaxies emit synchrotron radiation up to X-rays. Since synchrotron radiation is polarized, it is important for observing magnetic fields.

First consider the non-relativistic case where the electron has low kinetic energy. An electron of mass m_e entering a magnetic field $\mathbf{B}$ with velocity $\mathbf{v}$ is subjected to the Lorentz force of

$$m_e \frac{d\mathbf{v}}{dt} = -\frac{e}{c}\mathbf{v} \times \mathbf{B} \tag{A.16}$$

and is in spiral motion around the magnetic field, with radius

$$r_g = \frac{m_e c v}{eB \sin\psi}, \tag{A.17}$$

where m_e is the electron mass, e is the elementary charge, c is the speed of light, and ψ is the pitch angle of the helix. This radius is called the cyclotron radius. Electrons emit electromagnetic radiation in order to undergo acceleration. This radiation is called cyclotron radiation. The frequency at which this occurs is

$$\nu_g = \frac{v}{2\pi r_g} = \frac{eB \sin\psi}{2\pi m_e c}. \tag{A.18}$$

When the electron is in motion at relativistic energy, the effective mass of the electron can be expressed as $m_e\gamma$ using the Lorentz factor $\gamma = (1 - v^2/c^2)^{-1/2}$. The cyclotron radiation at this time is called synchrotron radiation. Therefore, the cyclotron frequency in the relativistic case is

$$\nu_s = \frac{eB \sin\psi}{2\pi\gamma m_e c} = \frac{eB_\perp}{2\pi\gamma m_e c} = \frac{\nu_g}{\gamma}, \tag{A.19}$$

where $B_\perp = B \sin\psi$ is the magnetic field perpendicular to the line of sight. The synchrotron radiation is emitted as a sharp beam in the direction tangent to the electron orbit. The angular width of the beam is about $1/\gamma$. This is called the relativistic beaming effect.

The observer can only observe the radiation for the short period of time that this beam passes. Therefore, a periodic pulse of radio waves is observed. Since this period corresponds to the period of the spiral motion, the reciprocal of the frequency is

$$\tau = \frac{1}{\nu_s} = \frac{2\pi\gamma m_e c}{eB_\perp}. \tag{A.20}$$

The time at which the pulse is observed is

$$\Delta t \sim \frac{m_e c}{eB_\perp \gamma^2}, \tag{A.21}$$

considering the spiral motion from the observation of the end of the cone to the observation of the opposite end. From the Fourier transform relationship, a pulse wave with a time width Δt can be transformed into a decreasing function with a frequency width of $1/\Delta t$. In radio astronomy, $1/\Delta t$ multiplied by $3/4\pi$ is used as the critical frequency ν_c in synchrotron radiation and is expressed as

$$\nu_c \equiv \frac{3eB_\perp \gamma^2}{4\pi m_e c} \tag{A.22}$$

The radiation intensity peaks near the critical frequency. Also, from $\omega = 2\pi\nu$, the critical angular frequency is

$$\omega_c \equiv \frac{3eB_\perp \gamma^2}{2m_e c}. \tag{A.23}$$

The frequency distribution of synchrotron radiation intensity from electrons of energy $E = m_e c^2 \gamma$ is obtained by Fourier transforming the electric field and is given by

$$P(\omega) = \frac{\sqrt{3}}{2\pi} \frac{e^3 B_\perp}{m_e c^2} F\left(\frac{\omega}{\omega_c}\right), \tag{A.24}$$

where

$$F(x) = x \int_x^\infty K_{5/3}(\eta) d\eta \tag{A.25}$$

and K is a Bessel function. If we divide this radiation into a vertical component relative to the magnetic field and a horizontal component, we can express it as

$$P_\perp(\omega) = \frac{\sqrt{3} e^3 B_\perp}{4\pi m_e c^2} \left[F(x) + G(x)\right] \tag{A.26}$$

$$P_\parallel(\omega) = \frac{\sqrt{3} e^3 B_\perp}{4\pi m_e c^2} \left[F(x) – G(x)\right], \tag{A.27}$$

where $x \equiv \omega_c/\omega$. Also,

$$G(x) = xK_{2/3}(x). \tag{A.28}$$

In actual observations, it is necessary to consider synchrotron radiation from the electron population. The energy distribution of high-energy electrons produced by Fermi acceleration, etc., can usually be approximated (e.g. [43]) by the power function shown below and expressed as

$$N(E)dE = C(r)E^{-s}dE \;\; or \;\; N(\gamma)d\gamma = C(r)\gamma^{-s}d\gamma \tag{A.29}$$

$N(E)$ is the number of electrons whose energy is between $E - E - E + dE$, $C(r)$ is the number density of electrons at position r, and s is the power exponent of the electron energy distribution. The frequency spectrum of synchrotron radiation can be integrated over the entire energy range of electrons for each ν, and if we take care of $\omega_c \propto \gamma^2$, we get

$$P_{tot}(\omega) = \frac{\sqrt{3}e^3 B_\perp}{2\pi m_e c^2} C(r) \int F\left(\frac{\omega}{\omega_c}\right) \gamma^{-s} d\gamma \propto \omega^{-\frac{s-1}{2}} \int F(x)\, x^{\frac{s-3}{2}} dx \tag{A.30}$$

. From this, the frequency spectrum of synchrotron radiation when the power exponent of the electron energy distribution is s is $P_{tot}(\omega) \propto \omega^a lpha \propto \nu^\alpha$, where

$$\alpha = \frac{s-1}{2} \tag{A.31}$$

and α is called the spectral index.

$$\int_0^\infty x^\mu F(x) dx = \frac{2^{\mu+1}}{\mu+2} \Gamma\left(\frac{\mu}{2} + \frac{7}{3}\right) \Gamma\left(\frac{\mu}{2} + \frac{2}{3}\right) \tag{A.32}$$

$$\int_0^\infty x^\mu G(x) dx = 2^\mu \Gamma\left(\frac{\mu}{2} + \frac{4}{3}\right) \Gamma\left(\frac{\mu}{2} + \frac{2}{3}\right) \tag{A.33}$$

holds for $F(x)$ and $G(x)$ using the Γ function. From the above, the frequency distribution of the synchrotron radiation spectrum per unit solid angle and frequency from the electron population per unit volume of the radiation source can be expressed as

$$P_{tot}(\omega) = 2 g_1(s) j(s) C(r) B_\perp^{\frac{1+s}{2}} \omega^{\frac{1-s}{2}} \tag{A.34}$$

$$g_1(s) = \frac{1}{1+s} 2^{\frac{1+s}{2}} \Gamma\left(\frac{s}{4} + \frac{19}{12}\right) \Gamma\left(\frac{s}{4} - \frac{1}{12}\right) \tag{A.35}$$

$$j(s) = \frac{1}{4\pi} \frac{\sqrt{3}e^3}{8\pi m_e c^2} \left(\frac{2 m_e c}{3e}\right)^{\frac{1-s}{2}} \tag{A.36}$$

In actual observations, the information in the line-of-sight direction is degenerate, and the frequency distribution of the synchrotron radiation spectrum obtained is given by

$$I = \int P_{tot}(\omega) dr = \int 2 g_1(s) j(s) C(r) B_\perp^{\frac{1+s}{2}} \omega^{\frac{1-s}{2}} dr. \tag{A.37}$$

The I is called the characteristic Stokes parameter.

Polarization due to synchrotron radiation can be regarded as linear polarization. From the above discussion, since the polarization wave due to synchrotron radiation is perpendicular to the magnetic field, the polarization wave $P_\perp$ has the maximum intensity, and the intensity of the polarization wave $P_{parallel}$ parallel to the magnetic field has the minimum intensity. Here, the linear polarization rate can be expressed as

$$p = \frac{P_\perp - P_\parallel}{P_\perp + P_\parallel} \tag{A.38}$$

from the discussion of the Stokes parameter. Replacing this equation with the actual observation, we can express it as

$$p = \frac{\int (P_\perp - P_\parallel) dr}{\int (P_\perp + P_\parallel) dr} = \frac{Q + iU}{I} \tag{A.39}$$

The I, Q, and U are the characteristic Stokes parameters. Furthermore, $Q + iU$ can be expressed as

$$Q + iU = \int 2g_2(s) j(s) C(r) B_\perp^{\frac{1+s}{2}} \omega^{\frac{1-s}{2}} e^{2i\chi} dr \tag{A.40}$$

$$g_2(s) = 2^{\frac{s-3}{2}} \Gamma\left(\frac{s}{4} - \frac{1}{12}\right) \Gamma\left(\frac{s}{4} + \frac{7}{12}\right) \tag{A.41}$$

A.3 Faraday rotation

The polarization angle is known to rotate under the influence of magnetized plasma in the line of sight. This phenomenon is called Faraday rotation. In the following, we will explain the principle and the method of observing the magnetic field in the line-of-sight direction using Faraday rotation.

There are many plasma gases in space. Radio waves emitted from celestial objects are observed after being affected by that plasma gas. The electric field of a radio wave propagating in plasma is denoted as

$$\mathbf{E} = \mathbf{E_0} \exp\{[i(\omega t - \mathbf{k} \cdot \mathbf{r})]\}, \tag{A.42}$$

where $\mathbf{K}$ is the wave number vector, $\mathbf{R}$ is the position vector, and ω is the frequency. For simplicity, let us consider a situation where a magnetic field $\mathbf{H}$ exists uniformly in the z-axis direction and a radio wave propagates in the xz plane. In this case, $\mathbf{k}$ can be expressed as $\mathbf{k} = (k \sin\theta, 0, k\cos\theta)$ using the angle θ between the direction of the radio wave and the z axis. Electrons in the plasma are subject to the Lorentz force as follows.

$$\frac{d(m_e \mathbf{v})}{dt} = -e\left(\mathbf{E} + \frac{1}{c}\mathbf{v} \times \mathbf{H}\right) \tag{A.43}$$

Considering that the motion of electrons varies with $|\mathbf{v}| \propto e^{i\omega t}$ in the same way as the electric field, each component of the velocity is

$$\begin{cases} v_x = \frac{ie}{m_e(\omega^2 - \omega_g^2)} \left(\omega E_x + i\omega_g E_y\right) \\ v_y = \frac{-ie}{m_e(\omega^2 - \omega_g^2)} \left(i\omega_g E_x - \omega E_y\right) \\ v_z = \frac{ie}{m_e \omega} E_z \end{cases} \tag{A.44}$$

where ω_g is the cyclotron frequency, which can be written as

$$\omega_g = \frac{eH_z}{m_e c} \tag{A.45}$$

If the current density is

$$\mathbf{j} = -n_e e \mathbf{v} \tag{A.46}$$

and so, from the Ampere-Maxwell equation

$$\nabla \times \mathbf{H} = -\frac{4\pi}{c} n_e e \mathbf{v} + \frac{i\omega}{c}\mathbf{E} \tag{A.47}$$

is obtained. From equation A.44, we get

$$(\nabla \times \mathbf{H})_i = \frac{i\omega}{c}\epsilon_{ij}E_j \tag{A.48}$$

$$\epsilon = \begin{pmatrix} 1 + \frac{\omega_p^2}{\omega_g^2 - \omega^2} & \frac{i\omega_p^2\omega_g}{\omega(\omega_g^2-\omega^2)} & 0 \\ \frac{i\omega_p^2\omega_g}{\omega(\omega_g^2-\omega^2)} & 1 + \frac{\omega_p^2}{\omega_g^2-\omega^2} & 0 \\ 0 & 0 & 1 - \frac{\omega_p^2}{\omega^2} \end{pmatrix} = \begin{pmatrix} \epsilon_{11} & \epsilon_{12} & \epsilon_{13} \\ \epsilon_{21} & \epsilon_{22} & \epsilon_{23} \\ \epsilon_{31} & \epsilon_{32} & \epsilon_{33} \end{pmatrix}, \tag{A.49}$$

where $\omega_p^2 = \frac{4\pi e^2 n_e}{m_e}$. This ω_p is called the plasma frequency.

From the electromagnetic wave equation propagating in vacuum and the equation (A.48),

$$\{\mathbf{k} \times (\mathbf{k} \times \mathbf{E})\}_i = \frac{\omega}{c}(\mathbf{k} \times \mathbf{H})_i = -\frac{\omega^2}{c^2}\epsilon_{ij}E_j \tag{A.50}$$

is obtained. Using the formula for vector analysis, $\mathbf{k} \times (\mathbf{k} \times \mathbf{E}) = (\mathbf{k} \cdot \mathbf{E})\mathbf{k} - (\mathbf{k} \cdot \mathbf{k})\mathbf{E}$, it can be transformed to

$$k^2 E_i - k_i k_j E_j - \frac{\omega^2}{c^2}\epsilon_{ij}E_j = 0. \tag{A.51}$$

The equation is

$$\left| k^2 \delta_{ij} - k_i k_j - \frac{\omega^2}{c^2}\epsilon_{ij} \right| = 0 \tag{A.52}$$

from the dispersion formula of the determinant = 0 for this equation to have a solution. Because $\omega \gg \omega_g$ in the radio observation, we can approximate $\epsilon_{11} = \epsilon_{22} \sim \epsilon_{33}$. Then, we get

$$k^2 = \frac{\omega^2}{c^2}\epsilon_{11}\left[1 - \frac{\epsilon_{12}^2}{2\epsilon_{11}^2}\left\{\sin^2\theta \pm \sqrt{\sin^4\theta + \left(\frac{2\epsilon_{11}\cos\theta}{\epsilon_{12}}\right)^2}\right\}\right]. \tag{A.53}$$

Here, when the radio wave propagates in a direction parallel to the magnetic field of the plasma, that is, $\theta \sim 0$, the wave number is

$$k_{\mp} = \frac{\omega}{c}\sqrt{\epsilon_{11} \mp \epsilon_{12}\cos\theta}. \tag{A.54}$$

The k_- represents a right circularly polarized wave rotating clockwise toward the direction of propagation, and k_+ represents a left circularly polarized wave rotating counterclockwise toward the direction of propagation.

Next, consider the case where the radio wave is linearly polarized. Linearly polarized waves can be described by superposition of right circularly polarized waves and left circularly polarized waves with the same amplitude. These circularly polarized waves have wave numbers k_- and k_+, respectively, from the equation (A.54). Therefore, a phase shift occurs in the circularly polarized wave as it propagates through the magnetized plasma, and the direction of oscillation of the electric field changes. This phenomenon is called Faraday rotation.

Suppose that under the conditions $\omega \gg \omega_g$ and $\omega \gg \omega_p$, the magnetic field exists along the z axis and the linearly polarized wave propagates in the z direction ($\theta \sim 0$). In this case, the phase change when the wave travels dz in the plasma is

$$d\phi_- = k_- dz,\ d\phi_+ = k_+ dz. \tag{A.55}$$

Because the amount of change in this linear polarization is equal to the total phase shift, we get

$$\begin{aligned}\phi &= \int_{\infty}^{0} \frac{k_- - k_+}{2} dz = \frac{\omega}{2c}\int_{\infty}^{0}\left[\sqrt{\epsilon_{11} - \epsilon_{12}\cos\theta} - \sqrt{\epsilon_{11}\epsilon_{12}\cos\theta}\right] dz \\ &= \frac{e^3\lambda^2}{8\pi^2 c^3 m_e^2 \epsilon_0}\int_{\infty}^{0} n_e(z) B_{\parallel}(z) dz = \mathrm{RM}\,\lambda^2, \end{aligned} \tag{A.56}$$

where $B_{\parallel}$ is the magnetic field strength parallel to the line of sight and n_e is the electron number density. RM is called Rotation Measure and is written as

$$\mathrm{RM} = 0.81 \int_{\infty}^{0} \left(\frac{n_e}{\mathrm{cm}^{-3}}\right)\left(\frac{B_{\parallel}}{\mu\mathrm{G}}\right) d\left(\frac{z}{\mathrm{pc}}\right)\ \mathrm{rad\,m^{-2}}, \tag{A.57}$$

where the unit of wavelength is m. RM is defined as positive if the magnetic field is in direction toward the observer and negative if it is in the opposite direction.

These results indicate that when a linearly polarized wave passes through a magnetized plasma, the polarization angle changes in proportion to the square of the observed wavelength. From this relationship, if the observed polarization angle is χ and the polarization angle of the polarization source itself is χ_0, it can be written as

$$\chi = \mathrm{RM}\lambda^2 + \chi_0. \tag{A.58}$$

From this equation (A.58), information on the polarization angle of the polarization

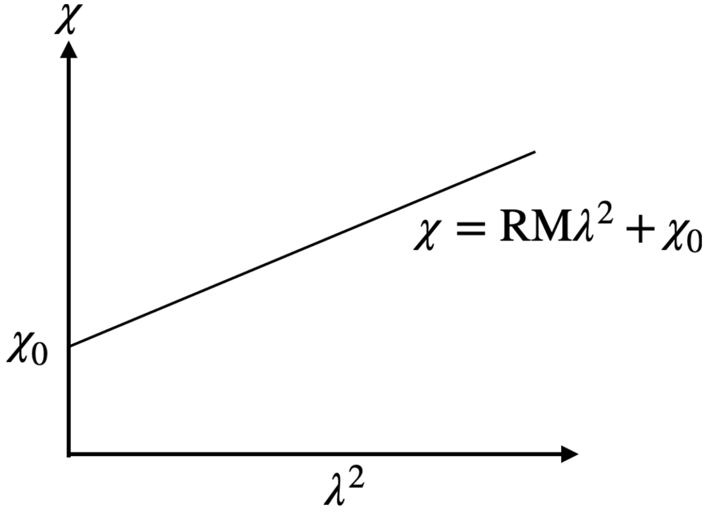

Figure A.2: Polarization angle vs. wavelength squared

source and the magnetic field parallel to the line of sight on the line of sight can be obtained. In actual observation, the Stokes parameters Q and U are observed at multiple wavelengths, the polarization angle χ is obtained, and a straight line fit is made to a plot with $\chi - \lambda^2$. The slope is RM, and the Y-intercept is χ_0 (FigureA.2).

A.4 Faraday tomography

RM stands for Rotation Measure which can be written as

$$\mathrm{RM} = 0.81 \int_{\infty}^{0} \left(\frac{n_e}{\mathrm{cm}^{-3}}\right) \left(\frac{B_{\parallel}}{\mu\mathrm{G}}\right) d\left(\frac{r}{\mathrm{pc}}\right) \mathrm{rad/m}^2, \tag{A.59}$$

where n_e is the number density of electron, $B_{\parallel}$ is line of sight component of the magnetic field strength and r is the physical distance to the source. It is clear from this equation that the observed RM has degenerated information in the line of sight. Then, Faraday tomography, proposed by Burn (1966) [45], has been attracting attention as a new method for estimating material structure in the line of sight. The expression for the linear polarized intensity $P(\lambda^2)$ can be written as

$$P(\lambda^2) = \int_{-\infty}^{\infty} F(\phi) e^{2i\phi\lambda^2} d\phi. \tag{A.60}$$

This $F(\phi)$ is called the Faraday Dispersion Function (FDF) or Faraday spectrum, and represents the polarized intensity distribution in ϕ space. ϕ is written as

$$\phi(r) = 0.81 \int_{r}^{0} n_e(r') B_{\parallel}(r') dr'. \tag{A.61}$$

It is a physical quantity similar to RM, but it is an integral up to position r, whereas RM is an integral from the observer to infinity. $\phi(r)$ is called the Faraday depth. Also, Equation A.60 is a Fourier transform with ϕ and λ^2 as conjugate variables. The inverse transformation can be written as

$$F(\phi) = \frac{1}{2\pi} \int_{-\infty}^{\infty} P(\lambda^2) e^{-2i\phi\lambda^2} d\phi. \tag{A.62}$$

We can estimate $F(\phi)$ from the observables $P(\lambda^2)$.

However, in reality, it is impossible to observe all the points in λ^2 space, which results in an incomplete Fourier transform and makes it difficult to obtain a true Faraday spectrum. Then, a method of estimation using the window function W was proposed by Brentjens & de Bruyn (2005) [46]. The Faraday spectrum $\tilde{F}(\phi)$, which consists only of the polarized intensity of the observed wavelength, can be written as,

$$\tilde{F}(\phi) = \frac{1}{2\pi} \int_{-\infty}^{\infty} W(\lambda^2) P(\lambda^2) e^{-2i\phi\lambda^2} d\phi, \tag{A.63}$$

where $\tilde{F}(\phi)$ is called the dirty FDF. Furthermore, because of the convolution, we can write

$$\tilde{F}(\phi) = \frac{1}{K} F(\phi) * R(\phi), \tag{A.64}$$

$$K^{-1} = \int_{-\infty}^{\infty} W(\lambda^2) d\lambda^2, \tag{A.65}$$

$$R(\phi) = K \int_{-\infty}^{\infty} W(\lambda^2) e^{-2i\phi\lambda^2} d\lambda^2. \tag{A.66}$$

The $R(\phi)$ is called the Rotation Measure Spread Function (RMSF) and the Full Width at Half Maximum (FWHM) of the RMSF is the RM resolution of Faraday tomography. In general, the window function takes the value, in the observable wavelength band ($\lambda^2_{\rm min} \le \lambda^2 \le \lambda^2_{\rm max}$), with $W(\lambda^2) = 1$ and 0 otherwise. In this case, the FWHM of the RMSF is written as,

$$\mathrm{FWHM}\,[\mathrm{rad/m^2}] = \frac{2\sqrt{3}}{\Delta\lambda^2\,[\mathrm{m^2}]}, \ \Delta\lambda^2 = \lambda^2_{\rm max} - \lambda^2_{\rm min}. \tag{A.67}$$

As can be seen from this equation, the range of the wavelength squared space determines the RM resolution.

A.4.1 QU-fitting

QU-fitting is a method of constructing an FDF by model fitting without an incomplete Fourier transform of the polarization spectrum, which is an observable. The first model assumption considers functions that can be mathematically fully Fourier transformed (e.g., delta, Gaussian, top-hat, etc.) (generally to reduce computational complexity). The form and number of functions are inferred from simple inverse transforms and RM CLEAN results. Next, the model parameters are estimated using the Metropolis-Hasting algorithm in the Markov Chain Monte Carlo (MCMC) method. This is a method to estimate the value of the best-fit parameter by adopting the parameter value with the highest likelihood when randomly transitioning in a step width with a certain defined width in the parameter space. In addition, since this algorithm adopts the parameter value with a certain probability even when the likelihood drops, it is less likely to be trapped by local minima in the likelihood than simpler methods such as the steepest descent method.

Acknowledgment

First and foremost, I am deeply grateful to my supervisor, Associate Prof. Mami Machida, for their continuous guidance, support, and enthusiasm. She provided a very friendly environment where I could discuss anything with them. I would take this opportunity to thank the following people. Dr. Takuya Akahori for being a wonderful collaborator and for long discussions. He shared with me the interesting nature of magnetic field observations of the Universe. I would like to thank the review committee members Associate Prof. Hatsukade Bunyo, Associate Prof. Daisuke Iono, Assistant Prof. Kimihiko Nakajima, Prof. Motokazu Takizawa, and Associate Prof. Ryuichi Takahashi for their hard work in reviewing the thesis. Thank you very much for taking time out of your busy schedule to carefully read my thesis and provide valuable comments. I wish to thank all (present and former) members of theoretical astrophysics group in Kyushu University, Department of Astronomical Science in SOKENDAI and the Division of Science in National Astronomical Observatory of Japan. In particular, Dr. Haruka Sakemi and Dr. Takumi Ohmura have taught me many things from everyday life to research life since I was an undergraduate student. I can't thank you enough. I would like to thank Dr. Kohei Kurahara and Dr. Yuki Kudo for all their help with my seminar and research. At this important stage of my life, I would like to remember my friend Yuta Tashima. SKA-JP and the POSSUM team gave me many opportunities to introduce my research and to meet many people. Last but surely not least, I would like to thank my parents, Kiriko Omae and Shigenori Omae, for their love, support, and everything.

Bibliography

[1] S. A. Mao, C. Carilli, B. M. Gaensler, O. Wucknitz, C. Keeton, A. Basu, R. Beck, P. P. Kronberg, and E. Zweibel. Detection of microgauss coherent magnetic fields in a galaxy five billion years ago. *Nature Astronomy*, Vol. 1, pp. 621–626, August 2017.

[2] Luke Chamandy, Anvar Shukurov, Kandaswamy Subramanian, and Katherine Stoker. Non-linear galactic dynamos: a toolbox. *MNRAS*, Vol. 443, No. 3, pp. 1867–1880, September 2014.

[3] Peng Wang and Tom Abel. Magnetohydrodynamic Simulations of Disk Galaxy Formation: The Magnetization of the Cold and Warm Medium. *ApJ*, Vol. 696, No. 1, pp. 96–109, May 2009.

[4] Rüdiger Pakmor and Volker Springel. Simulations of magnetic fields in isolated disc galaxies. *MNRAS*, Vol. 432, No. 1, pp. 176–193, June 2013.

[5] Rüdiger Pakmor, Federico Marinacci, and Volker Springel. Magnetic Fields in Cosmological Simulations of Disk Galaxies. *ApJ*, Vol. 783, No. 1, p. L20, March 2014.

[6] M. A. de Avillez and D. Breitschwerdt. Global dynamical evolution of the ISM in star forming galaxies. I. High resolution 3D simulations: Effect of the magnetic field. *A&A*, Vol. 436, No. 2, pp. 585–600, June 2005.

[7] Christophe Gissinger, Sebastien Fromang, and Emmanuel Dormy. Direct numerical simulations of the galactic dynamo in the kinematic growing phase. *MNRAS*, Vol. 394, No. 1, pp. L84–L88, March 2009.

[8] Alex S. Hill, M. Ryan Joung, Mordecai-Mark Mac Low, Robert A. Benjamin, L. Matthew Haffner, Christian Klingenberg, and Knut Waagan. Vertical Structure of a Supernova-driven Turbulent, Magnetized Interstellar Medium. *ApJ*, Vol. 750, No. 2, p. 104, May 2012.

[9] Oliver Gressel, Detlef Elstner, and Udo Ziegler. Towards a hybrid dynamo model for the Milky Way. *A&A*, Vol. 560, p. A93, December 2013.

[10] Mami Machida, Kenji E. Nakamura, Takahiro Kudoh, Takuya Akahori, Yoshiaki Sofue, and Ryoji Matsumoto. Dynamo Activities Driven by Magnetorotational Instability and the Parker Instability in Galactic Gaseous Disks. *ApJ*, Vol. 764, No. 1, p. 81, February 2013.

[11] Yuval Birnboim, Shmuel Balberg, and Romain Teyssier. Galaxy evolution: modelling the role of non-thermal pressure in the interstellar medium. *MNRAS*, Vol. 447, No. 4, pp. 3678–3692, March 2015.

[12] Planck Collaboration, P. A. R. Ade, N. Aghanim, M. I. R. Alves, M. Arnaud, D. Arzoumanian, M. Ashdown, J. Aumont, C. Baccigalupi, A. J. Banday, R. B. Barreiro, N. Bartolo, E. Battaner, K. Benabed, A. Benoît, A. Benoit-Lévy, J. P. Bernard, M. Bersanelli, P. Bielewicz, J. J. Bock, L. Bonavera, J. R. Bond, J. Borrill, F. R. Bouchet, F. Boulanger, A. Bracco, C. Burigana, E. Calabrese, J. F. Cardoso, A. Catalano, H. C. Chiang, P. R. Christensen, L. P. L. Colombo, C. Combet, F. Couchot, B. P. Crill, A. Curto, F. Cuttaia, L. Danese, R. D. Davies, R. J. Davis, P. de Bernardis, A. de Rosa, G. de Zotti, J. Delabrouille, C. Dickinson, J. M. Diego, H. Dole, S. Donzelli, O. Doré, M. Douspis, A. Ducout, X. Dupac, G. Efstathiou, F. Elsner, T. A. Enßlin, H. K. Eriksen, D. Falceta-Gonçalves, E. Falgarone, K. Ferrière, F. Finelli, O. Forni, M. Frailis, A. A. Fraisse, E. Franceschi, A. Frejsel, S. Galeotta, S. Galli, K. Ganga, T. Ghosh, M. Giard, E. Gjerløw, J. González-Nuevo, K. M. Górski, A. Gregorio, A. Gruppuso, J. E. Gudmundsson, V. Guillet, D. L. Harrison, G. Helou, P. Hennebelle, S. Henrot-Versillé, C. Hernández-Monteagudo, D. Herranz, S. R. Hildebrandt, E. Hivon, W. A. Holmes, A. Hornstrup, K. M. Huffenberger, G. Hurier, A. H. Jaffe, T. R. Jaffe, W. C. Jones, M. Juvela, E. Keihänen, R. Keskitalo, T. S. Kisner, J. Knoche, M. Kunz, H. Kurki-Suonio, G. Lagache, J. M. Lamarre, A. Lasenby, M. Lattanzi, C. R. Lawrence, R. Leonardi, F. Levrier, M. Liguori, P. B. Lilje, M. Linden-Vørnle, M. López-Caniego, P. M. Lubin, J. F. Macías-Pérez, D. Maino, N. Mandolesi, A. Mangilli, M. Maris, P. G. Martin, E. Martínez-González, S. Masi, S. Matarrese, A. Melchiorri, L. Mendes, A. Mennella, M. Migliaccio, M. A. Miville-Deschênes, A. Moneti, L. Montier, G. Morgante, D. Mortlock, D. Munshi, J. A. Murphy, P. Naselsky, F. Nati, C. B. Netterfield, F. Noviello, D. Novikov, I. Novikov, N. Oppermann, C. A. Oxborrow, L. Pagano, F. Pajot, R. Paladini, D. Paoletti, F. Pasian, L. Perotto, V. Pettorino, F. Piacentini, M. Piat, E. Pierpaoli, D. Pietrobon, S. Plaszczynski, E. Pointecouteau, G. Polenta, N. Ponthieu, G. W. Pratt, S. Prunet, J. L. Puget, J. P. Rachen, M. Reinecke, M. Remazeilles, C. Renault, A. Renzi, I. Ristorcelli, G. Rocha, M. Rossetti, G. Roudier, J. A. Rubiño-Martín, B. Rusholme, M. Sandri, D. Santos, M. Savelainen, G. Savini, D. Scott, J. D. Soler, V. Stolyarov, R. Sudiwala, D. Sutton, A. S. Suur-Uski, J. F. Sygnet, J. A. Tauber, L. Terenzi, L. Toffolatti, M. Tomasi, M. Tristram, M. Tucci, G. Umana, L. Valenziano, J. Valiviita, B. Van Tent, P. Vielva, F. Villa, L. A. Wade, B. D. Wandelt, I. K. Wehus, N. Ysard, D. Yvon, and A. Zonca. Planck intermediate results. XXXV. Probing the role of the magnetic field in the

formation of structure in molecular clouds. *A&A*, Vol. 586, p. A138, February 2016.

[13] Enrique Vázquez-Semadeni, Jongsoo Kim, and Javier Ballesteros-Paredes. Star Formation Efficiency in Driven, Supercritical, Turbulent Clouds. *ApJ*, Vol. 630, No. 1, pp. L49–L52, September 2005.

[14] Joshua Wiener, Ellen G. Zweibel, and S. Peng Oh. Cosmic Ray Heating of the Warm Ionized Medium. *ApJ*, Vol. 767, No. 1, p. 87, April 2013.

[15] Ruth Durrer and Andrii Neronov. Cosmological magnetic fields: their generation, evolution and observation. *A&ARv*, Vol. 21, p. 62, June 2013.

[16] M. Lazar, R. Schlickeiser, R. Wielebinski, and S. Poedts. Cosmological Effects of Weibel-Type Instabilities. *ApJ*, Vol. 693, No. 2, pp. 1133–1141, March 2009.

[17] R. Schlickeiser. Cosmic Magnetization: From Spontaneously Emitted Aperiodic Turbulent to Ordered Equipartition Fields. *Phys. Rev. Lett.*, Vol. 109, No. 26, p. 261101, December 2012.

[18] R. Schlickeiser and T. Felten. Strength of the Spontaneously Emitted Collective Aperiodic Magnetic Field Fluctuations in the Reionized Early Intergalactic Medium. *ApJ*, Vol. 778, No. 1, p. 39, November 2013.

[19] G. S. Bisnovatyi-Kogan, A. A. Ruzmaikin, and R. A. Syunyaev. Star Contraction and Magnetic-Field Generation in Protogalaxies. *Soviet Ast.*, Vol. 17, p. 137, August 1973.

[20] Martin J. Rees. Magnetic Fields in the Early Universe. In Richard Wielebinski and Rainer Beck, editors, *Cosmic Magnetic Fields*, Vol. 664, p. 1. 2005.

[21] Hidekazu Hanayama, Keitaro Takahashi, Kei Kotake, Masamune Oguri, Kiyotomo Ichiki, and Hiroshi Ohno. Biermann Mechanism in Primordial Supernova Remnant and Seed Magnetic Fields. *ApJ*, Vol. 633, No. 2, pp. 941–945, November 2005.

[22] K. Ferriere. Alpha-tensor and diffusivity tensor due to supernovae and superbubbles in the Galactic disk near the Sun. *A&A*, Vol. 310, pp. 438–455, June 1996.

[23] Chang-Goo Kim, Woong-Tae Kim, and Eve C. Ostriker. Interstellar Turbulence Driving by Galactic Spiral Shocks. *ApJ*, Vol. 649, No. 1, pp. L13–L16, September 2006.

[24] Russell M. Kulsrud, Renyue Cen, Jeremiah P. Ostriker, and Dongsu Ryu. The Protogalactic Origin for Cosmic Magnetic Fields. *ApJ*, Vol. 480, No. 2, pp. 481–491, May 1997.

[25] D. R. G. Schleicher, R. Banerjee, S. Sur, T. G. Arshakian, R. S. Klessen, R. Beck, and M. Spaans. Small-scale dynamo action during the formation of the first stars and galaxies. I. The ideal MHD limit. *A&A*, Vol. 522, p. A115, November 2010.

[26] A. M. Beck, H. Lesch, K. Dolag, H. Kotarba, A. Geng, and F. A. Stasyszyn. Origin of strong magnetic fields in Milky Way-like galactic haloes. *MNRAS*, Vol. 422, No. 3, pp. 2152–2163, May 2012.

[27] Michael Rieder and Romain Teyssier. A small-scale dynamo in feedback-dominated galaxies as the origin of cosmic magnetic fields - I. The kinematic phase. *MNRAS*, Vol. 457, No. 2, pp. 1722–1738, April 2016.

[28] H. Kotarba, H. Lesch, K. Dolag, T. Naab, P. H. Johansson, and F. A. Stasyszyn. Magnetic field structure due to the global velocity field in spiral galaxies. *MNRAS*, Vol. 397, No. 2, pp. 733–747, August 2009.

[29] B. M. Gaensler, M. Haverkorn, B. Burkhart, K. J. Newton-McGee, R. D. Ekers, A. Lazarian, N. M. McClure-Griffiths, T. Robishaw, J. M. Dickey, and A. J. Green. Low-Mach-number turbulence in interstellar gas revealed by radio polarization gradients. *Nature*, Vol. 478, No. 7368, pp. 214–217, October 2011.

[30] A. Fletcher, R. Beck, A. Shukurov, E. M. Berkhuijsen, and C. Horellou. Magnetic fields and spiral arms in the galaxy M51. *MNRAS*, Vol. 412, No. 4, pp. 2396–2416, April 2011.

[31] Rainer Beck. Magnetic fields in spiral galaxies. *A&ARv*, Vol. 24, p. 4, December 2015.

[32] L. F. S. Rodrigues, A. Shukurov, A. Fletcher, and C. M. Baugh. Galactic magnetic fields and hierarchical galaxy formation. *MNRAS*, Vol. 450, No. 4, pp. 3472–3489, July 2015.

[33] Rüdiger Pakmor, Freeke van de Voort, Rebekka Bieri, Facundo A. Gómez, Robert J. J. Grand, Thomas Guillet, Federico Marinacci, Christoph Pfrommer, Christine M. Simpson, and Volker Springel. Magnetizing the circumgalactic medium of disc galaxies. *MNRAS*, Vol. 498, No. 3, pp. 3125–3137, November 2020.

[34] Jr. Davis, Leverett and Jesse L. Greenstein. The Polarization of Starlight by Aligned Dust Grains. *ApJ*, Vol. 114, p. 206, September 1951.

[35] S. M. Scarrott, D. Ward-Thompson, and R. F. Warren-Smith. Evidence for a spiral magnetic field configuration in the galaxy M 51. *MNRAS*, Vol. 224, pp. 299–305, January 1987.

[36] Ch. Fendt, R. Beck, and N. Neininger. Spiral pattern in the optical polarization of NGC 6946. *A&A*, Vol. 335, pp. 123–133, July 1998.

[37] Aiara Lobo Gomes, Antônio Mário Magalhães, Antonio Pereyra, and Cláudia Vilega Rodrigues. A New Optical Polarization Catalog for the Small Magellanic Cloud: The Magnetic Field Structure. *ApJ*, Vol. 806, No. 1, p. 94, June 2015.

[38] Ya-Wen Tang, Paul T. P. Ho, Patrick M. Koch, Josep M. Girart, Shih-Ping Lai, and Ramprasad Rao. Evolution of Magnetic Fields in High-Mass Star Formation: Linking Field Geometry and Collapse for the W51 e2/e8 Cores. *ApJ*, Vol. 700, No. 1, pp. 251–261, July 2009.

[39] Jin-Ah Kim, Terry Jay Jones, and C. Darren Dowell. Exploring the Magnetic Field Geometry in NGC 891 with SOFIA/HAWC+. *AJ*, Vol. 165, No. 6, p. 223, June 2023.

[40] S. Chandrasekhar and E. Fermi. Magnetic Fields in Spiral Arms. *ApJ*, Vol. 118, p. 113, July 1953.

[41] Aritra Basu and Subhashis Roy. Magnetic fields in nearby normal galaxies: energy equipartition. *MNRAS*, Vol. 433, No. 2, pp. 1675–1686, August 2013.

[42] R. Beck and M. Krause. Revised equipartition and minimum energy formula for magnetic field strength estimates from radio synchrotron observations. *Astronomische Nachrichten*, Vol. 326, No. 6, pp. 414–427, July 2005.

[43] A. R. Bell. The acceleration of cosmic rays in shock fronts - II. *MNRAS*, Vol. 182, pp. 443–455, February 1978.

[44] Rodion Stepanov, Anvar Shukurov, Andrew Fletcher, Rainer Beck, Laura La Porta, and Fatemeh Tabatabaei. An observational test for correlations between cosmic rays and magnetic fields. *MNRAS*, Vol. 437, No. 3, pp. 2201–2216, January 2014.

[45] B. J. Burn. On the depolarization of discrete radio sources by Faraday dispersion. *MNRAS*, Vol. 133, p. 67, January 1966.

[46] M. A. Brentjens and A. G. de Bruyn. Faraday rotation measure synthesis. *A&A*, Vol. 441, No. 3, pp. 1217–1228, October 2005.

[47] Peter C. Tribble. Depolarization of extended radio sources by a foreground Faraday screen. *MNRAS*, Vol. 250, p. 726, June 1991.

[48] D. D. Sokoloff, A. A. Bykov, A. Shukurov, E. M. Berkhuijsen, R. Beck, and A. D. Poezd. Depolarization and Faraday effects in galaxies. *MNRAS*, Vol. 299, No. 1, pp. 189–206, August 1998.

[49] Tigran G. Arshakian and Rainer Beck. Optimum frequency band for radio polarization observations. *MNRAS*, Vol. 418, No. 4, pp. 2336–2342, December 2011.

[50] Takuya Akahori, Hiroyuki Nakanishi, Yoshiaki Sofue, Yutaka Fujita, Kiyotomo Ichiki, Shinsuke Ideguchi, Osamu Kameya, Takahiro Kudoh, Yuki Kudoh, Mami Machida, Yoshimitsu Miyashita, Hiroshi Ohno, Takeaki Ozawa, Keitaro Takahashi, Motokazu Takizawa, and Dai G. Yamazaki. Cosmic magnetism in centimeter- and meter-wavelength radio astronomy. *PASJ*, Vol. 70, No. 1, p. R2, January 2018.

[51] Michał Hanasz, Dominik Wóltański, and Kacper Kowalik. Global Galactic Dynamo Driven by Cosmic Rays and Exploding Magnetized Stars. *ApJ*, Vol. 706, No. 1, pp. L155–L159, November 2009.

[52] Russell M. Kulsrud. A Critical Review of Galactic Dynamos. *ARA&A*, Vol. 37, pp. 37–64, January 1999.

[53] Anvar Shukurov. Introduction to galactic dynamos. *arXiv e-prints*, pp. astro–ph/0411739, November 2004.

[54] Steven A. Balbus and John F. Hawley. A Powerful Local Shear Instability in Weakly Magnetized Disks. I. Linear Analysis. *ApJ*, Vol. 376, p. 214, July 1991.

[55] Axel Brandenburg, Ake Nordlund, Robert F. Stein, and Ulf Torkelsson. Dynamo-generated Turbulence and Large-Scale Magnetic Fields in a Keplerian Shear Flow. *ApJ*, Vol. 446, p. 741, June 1995.

[56] James M. Stone, John F. Hawley, Charles F. Gammie, and Steven A. Balbus. Three-dimensional Magnetohydrodynamical Simulations of Vertically Stratified Accretion Disks. *ApJ*, Vol. 463, p. 656, June 1996.

[57] Ya. B. Zel'dovich, A. A. Ruzmaikin, S. A. Molchanov, and D. D. Sokolov. Kinematic dynamo problem in a linear velocity field. *Journal of Fluid Mechanics*, Vol. 144, pp. 1–11, January 1984.

[58] Russell M. Kulsrud and Stephen W. Anderson. The Spectrum of Random Magnetic Fields in the Mean Field Dynamo Theory of the Galactic Magnetic Field. *ApJ*, Vol. 396, p. 606, September 1992.

[59] X. H. Sun, W. Reich, A. Waelkens, and T. A. Enßlin. Radio observational constraints on Galactic 3D-emission models. *A&A*, Vol. 477, No. 2, pp. 573–592, January 2008.

[60] A. R. Taylor, J. M. Stil, and C. Sunstrum. A Rotation Measure Image of the Sky. *ApJ*, Vol. 702, No. 2, pp. 1230–1236, September 2009.

[61] M. Prouza and R. Šmída. The Galactic magnetic field and propagation of ultra-high energy cosmic rays. *A&A*, Vol. 410, pp. 1–10, October 2003.

[62] Xiao-Hui Sun and Wolfgang Reich. The Galactic halo magnetic field revisited. *Research in Astronomy and Astrophysics*, Vol. 10, No. 12, pp. 1287–1297, December 2010.

[63] Guangtun Zhu and Brice Ménard. The JHU-SDSS Metal Absorption Line Catalog: Redshift Evolution and Properties of Mg II Absorbers. *ApJ*, Vol. 770, No. 2, p. 130, June 2013.

[64] P. P. Kronberg, M. L. Bernet, F. Miniati, S. J. Lilly, M. B. Short, and D. M. Higdon. A Global Probe of Cosmic Magnetic Fields to High Redshifts. *ApJ*, Vol. 676, No. 1, pp. 70–79, March 2008.

[65] Martin L. Bernet, Francesco Miniati, Simon J. Lilly, Philipp P. Kronberg, and Miroslava Dessauges-Zavadsky. Strong magnetic fields in normal galaxies at high redshift. *Nature*, Vol. 454, No. 7202, pp. 302–304, July 2008.

[66] M. L. Bernet, F. Miniati, and S. J. Lilly. The Interpretation of Rotation Measures in the Presence of Inhomogeneous Foreground Screens. *ApJ*, Vol. 761, No. 2, p. 144, December 2012.

[67] J. S. Farnes, S. P. O'Sullivan, M. E. Corrigan, and B. M. Gaensler. Faraday Rotation from Magnesium II Absorbers toward Polarized Background Radio Sources. *ApJ*, Vol. 795, No. 1, p. 63, November 2014.

[68] Sunil Malik, Hum Chand, and T. R. Seshadri. Role of Intervening Mg II Absorbers on the Rotation Measure and Fractional Polarization of the Background Quasars. *ApJ*, Vol. 890, No. 2, p. 132, February 2020.

[69] B. M. Gaensler, R. Beck, and L. Feretti. The origin and evolution of cosmic magnetism. *New Astron. Rev.*, Vol. 48, No. 11-12, pp. 1003–1012, December 2004.

[70] J. McKean, N. Jackson, S. Vegetti, M. Rybak, S. Serjeant, L. V. E. Koopmans, R. B. Metcalf, C. Fassnacht, P. J. Marshall, and M. Pandey-Pommier. Strong Gravitational Lensing with the SKA. In *Advancing Astrophysics with the Square Kilometre Array (AASKA14)*, p. 84, April 2015.

[71] Jennifer Schober, Dominik Schleicher, Christoph Federrath, Ralf Klessen, and Robi Banerjee. Magnetic field amplification by small-scale dynamo action: Dependence on turbulence models and Reynolds and Prandtl numbers. *Phys. Rev. E*, Vol. 85, No. 2, p. 026303, February 2012.

[72] Axel Brandenburg and Kandaswamy Subramanian. Astrophysical magnetic fields and nonlinear dynamo theory. *Phys. Rep.*, Vol. 417, No. 1-4, pp. 1–209, October 2005.

[73] T. G. Arshakian, R. Beck, Marita Krause, and D. Sokoloff. Evolution of magnetic fields in galaxies and future observational tests with the Square Kilometre Array. *A&A*, Vol. 494, No. 1, pp. 21–32, January 2009.

[74] J. M. Stil, M. Krause, R. Beck, and A. R. Taylor. The Integrated Polarization of Spiral Galaxy Disks. *ApJ*, Vol. 693, No. 2, pp. 1392–1403, March 2009.

[75] X. H. Sun and W. Reich. Polarisation properties of Milky-Way-like galaxies. *A&A*, Vol. 543, p. A127, July 2012.

[76] C. L. Van Eck, M. Haverkorn, M. I. R. Alves, R. Beck, A. G. de Bruyn, T. Enßlin, J. S. Farnes, K. Ferrière, G. Heald, C. Horellou, A. Horneffer, M. Iacobelli, V. Jelić, I. Martí-Vidal, D. D. Mulcahy, W. Reich, H. J. A. Röttgering, A. M. M. Scaife, D. H. F. M. Schnitzeler, C. Sobey, and S. S. Sridhar. Faraday tomography of the local interstellar medium with LOFAR: Galactic foregrounds towards IC 342. *A&A*, Vol. 597, p. A98, January 2017.

[77] Haruka Sakemi, Mami Machida, Takumi Ohmura, Shinsuke Ideguchi, Yoshimitsu Miyashita, Keitaro Takahashi, Takuya Akahori, Hiroki Akamatsu, Hiroyuki Nakanishi, Kohei Kurahara, and Jamie Farnes. Faraday Tomography of the SS433 Jet Termination Region. *Galaxies*, Vol. 6, No. 4, p. 137, December 2018.

[78] T. M. Cantwell, J. D. Bray, J. H. Croston, A. M. M. Scaife, D. D. Mulcahy, P. N. Best, M. Brüggen, G. Brunetti, J. R. Callingham, A. O. Clarke, M. J. Hardcastle, J. J. Harwood, G. Heald, V. Heesen, M. Iacobelli, M. Jamrozy, R. Morganti, E. Orrú, S. P. O'Sullivan, C. J. Riseley, H. J. A. Röttgering, A. Shulevski, S. S. Sridhar, C. Tasse, and C. L. Van Eck. Low-frequency observations of the giant radio galaxy NGC 6251. *MNRAS*, Vol. 495, No. 1, pp. 143–159, June 2020.

[79] Kwang Seong Kim, Simon J. Lilly, Francesco Miniati, Martin L. Bernet, Rainer Beck, Shane P. O'Sullivan, and Bryan M. Gaensler. Faraday Rotation Measure Synthesis of Intermediate Redshift Quasars as a Probe of Intervening Matter. *ApJ*, Vol. 829, No. 2, p. 133, October 2016.

[80] N. Oppermann, H. Junklewitz, G. Robbers, M. R. Bell, T. A. Enßlin, A. Bonafede, R. Braun, J. C. Brown, T. E. Clarke, I. J. Feain, B. M. Gaensler, A. Hammond, L. Harvey-Smith, G. Heald, M. Johnston-Hollitt, U. Klein, P. P. Kronberg, S. A. Mao, N. M. McClure-Griffiths, S. P. O'Sullivan, L. Pratley, T. Robishaw, S. Roy, D. H. F. M. Schnitzeler, C. Sotomayor-Beltran, J. Stevens, J. M. Stil, C. Sunstrum, A. Tanna, A. R. Taylor, and C. L. Van Eck. An improved map of the Galactic Faraday sky. *A&A*, Vol. 542, p. A93, June 2012.

[81] Takuya Akahori, Dongsu Ryu, Jongsoo Kim, and B. M. Gaensler. Simulated Faraday Rotation Measures toward High Galactic Latitudes. *ApJ*, Vol. 767, No. 2, p. 150, April 2013.

[82] Jun Xu and Jin-Lin Han. A compiled catalog of rotation measures of radio point sources. *Research in Astronomy and Astrophysics*, Vol. 14, No. 8, pp. 942–958, August 2014.

[83] S. Hutschenreuter, C. S. Anderson, S. Betti, G. C. Bower, J. A. Brown, M. Brüggen, E. Carretti, T. Clarke, A. Clegg, A. Costa, S. Croft, C. Van Eck, B. M. Gaensler, F. de Gasperin, M. Haverkorn, G. Heald, C. L. H. Hull, M. Inoue, M. Johnston-Hollitt, J. Kaczmarek, C. Law, Y. K. Ma, D. MacMahon, S. A. Mao, C. Riseley, S. Roy, R. Shanahan, T. Shimwell, J. Stil, C. Sobey, S. P. O'Sullivan, C. Tasse, V. Vacca, T. Vernstrom, P. K. G. Williams, M. Wright, and T. A. Enßlin. The Galactic Faraday rotation sky 2020. *A&A*, Vol. 657, p. A43, January 2022.

[84] Takuya Akahori and Dongsu Ryu. Faraday Rotation Measure Due to the Intergalactic Magnetic Field. *ApJ*, Vol. 723, No. 1, pp. 476–481, November 2010.

[85] Takuya Akahori and Dongsu Ryu. Faraday Rotation Measure due to the Intergalactic Magnetic Field. II. The Cosmological Contribution. *ApJ*, Vol. 738, No. 2, p. 134, September 2011.

[86] Alison M. Hammond, Timothy Robishaw, and B. M. Gaensler. A New Catalog of Faraday Rotation Measures and Redshifts for Extragalactic Radio Sources. *arXiv e-prints*, p. arXiv:1209.1438, September 2012.

[87] T. Vernstrom, B. M. Gaensler, L. Rudnick, and H. Andernach. Differences in Faraday Rotation between Adjacent Extragalactic Radio Sources as a Probe of Cosmic Magnetic Fields. *ApJ*, Vol. 878, No. 2, p. 92, June 2019.

[88] S. P. O'Sullivan, M. Brüggen, F. Vazza, E. Carretti, N. T. Locatelli, C. Stuardi, V. Vacca, T. Vernstrom, G. Heald, C. Horellou, T. W. Shimwell, M. J. Hardcastle, C. Tasse, and H. Röttgering. New constraints on the magnetization of the cosmic web using LOFAR Faraday rotation observations. *MNRAS*, Vol. 495, No. 3, pp. 2607–2619, July 2020.

[89] Yoshiaki Sofue, Mitsuaki Fujimoto, and Richard Wielebinski. Global structure of magnetic fields in spiral galaxies. *ARA&A*, Vol. 24, pp. 459–497, January 1986.

[90] Rainer Beck. Galactic and Extragalactic Magnetic Fields. *Space Sci. Rev.*, Vol. 99, pp. 243–260, October 2001.

[91] R. Beck. Galactic and extragalactic magnetic fields - a concise review. *Astrophysics and Space Sciences Transactions*, Vol. 5, No. 1, pp. 43–47, October 2009.

[92] Yoshiaki Sofue. Vertical Magnetic Fields in Spiral Galaxies. In R. Beck, P. P. Kronberg, and R. Wielebinski, editors, *Galactic and Intergalactic Magnetic Fields*, Vol. 140, p. 227, January 1990.

[93] Haruya Eguchi, Masaki Suzuki, Yoshimitsu Miyashita, Shinsuke Ideguchi, and Keitaro Takahashi. Faraday Dispersion Function of Disk Galaxies with Axisymmetric Global Magnetic Fields. I. *ApJ*, Vol. 899, No. 2, p. 122, August 2020.

[94] George Heald. The Faraday rotation measure synthesis technique. In Klaus G. Strassmeier, Alexander G. Kosovichev, and John E. Beckman, editors, *Cosmic Magnetic Fields: From Planets, to Stars and Galaxies*, Vol. 259, pp. 591–602, April 2009.

[95] Yoshimitsu Miyashita, Shinsuke Ideguchi, and Keitaro Takahashi. Performance test of RM CLEAN and its evaluation with chi-square value. *PASJ*, Vol. 68, No. 3, p. 44, June 2016.

[96] Yoshimitsu Miyashita, Shinsuke Ideguchi, Shouta Nakagawa, Takuya Akahori, and Keitaro Takahashi. Performance test of QU-fitting in cosmic magnetism study. *MNRAS*, Vol. 482, No. 2, pp. 2739–2749, January 2019.

[97] J. M. Cordes and T. J. W. Lazio. NE2001.I. A New Model for the Galactic Distribution of Free Electrons and its Fluctuations. *arXiv e-prints*, pp. astro–ph/0207156, July 2002.

[98] J. M. Yao, R. N. Manchester, and N. Wang. A New Electron-density Model for Estimation of Pulsar and FRB Distances. *ApJ*, Vol. 835, No. 1, p. 29, January 2017.

[99] B. M. Gaensler, G. J. Madsen, S. Chatterjee, and S. A. Mao. The Vertical Structure of Warm Ionised Gas in the Milky Way. *Publ. Astron. Soc. Australia*, Vol. 25, No. 4, pp. 184–200, November 2008.

[100] Ronnie Jansson and Glennys R. Farrar. A New Model of the Galactic Magnetic Field. *ApJ*, Vol. 757, No. 1, p. 14, September 2012.

[101] Volker Heesen, M. Krause, R. Beck, and R. J. Dettmar. The magnetic field structure in NGC 253 in presence of a galactic wind. In Klaus G. Strassmeier, Alexander G. Kosovichev, and John E. Beckman, editors, *Cosmic Magnetic Fields: From Planets, to Stars and Galaxies*, Vol. 259, pp. 509–514, April 2009.

[102] M. Krause. Magnetic Fields and Star Formation in Spiral Galaxies. In *Revista Mexicana de Astronomia y Astrofisica Conference Series*, Vol. 36 of *Revista Mexicana de Astronomia y Astrofisica Conference Series*, pp. 25–29, August 2009.

[103] Silvia Carolina Mora and Marita Krause. Magnetic field structure and halo in NGC 4631. *A&A*, Vol. 560, p. A42, December 2013.

[104] Jason Tumlinson, Molly S. Peeples, and Jessica K. Werk. The Circumgalactic Medium. *ARA&A*, Vol. 55, No. 1, pp. 389–432, August 2017.

[105] Takuya Akahori, Kohei Kumazaki, Keitaro Takahashi, and Dongsu Ryu. Exploring the intergalactic magnetic field by means of Faraday tomography. *PASJ*, Vol. 66, No. 3, p. 65, June 2014.

[106] J. Xu and J. L. Han. Redshift evolution of extragalactic rotation measures. *MNRAS*, Vol. 442, No. 4, pp. 3329–3337, August 2014.

[107] Takuya Akahori, B. M. Gaensler, and Dongsu Ryu. Statistical Techniques for Detecting the Intergalactic Magnetic Field from Large Samples of Extragalactic Faraday Rotation Data. *ApJ*, Vol. 790, No. 2, p. 123, August 2014.

[108] P. D. Greenfield, D. H. Roberts, and B. F. Burke. The gravitationally lensed quasar 0957+561 : VLA observations and mass models. *ApJ*, Vol. 293, pp. 370–386, June 1985.

[109] J. E. Geach, E. Lopez-Rodriguez, M. J. Doherty, Jianhang Chen, R. J. Ivison, G. J. Bendo, S. Dye, and K. E. K. Coppin. Polarized thermal emission from dust in a galaxy at redshift 2.6. *Nature*, Vol. 621, No. 7979, pp. 483–486, September 2023.

[110] Rikuto Omae, Takuya Akahori, and Mami Machida. Effects of depolarizing intervening galaxies on background radio emission. I. Global disk magnetic field. *PASJ*, Vol. 75, pp. S108–S122, February 2023.

[111] J. W. Nightingale, R. G. Hayes, Ashley Kelly, Aristeidis Amvrosiadis, Amy Etherington, Qiuhan He, Nan Li, XiaoYue Cao, Jonathan Frawley, Shaun Cole, Andrea Enia, Carlos S. Frenk, David R. Harvey, Ran Li, Richard J. Massey, Mattia Negrello, and Andrew Robertson. ‘pyautolens‘: Open-source strong gravitational lensing. *J. Open Source Softw.*, Vol. 6, No. 58, p. 2825, 2021.

[112] J. W. Nightingale and S. Dye. Adaptive semi-linear inversion of strong gravitational lens imaging. *MNRAS*, Vol. 452, No. 3, pp. 2940–2959, sep 2015.

[113] J. W. Nightingale, S. Dye, and Richard J. Massey. AutoLens: Automated modeling of a strong lens’s light, mass, and source. *MNRAS*, Vol. 478, No. 4, pp. 4738–4784, 2018.

[114] D. D. Sokoloff, A. A. Bykov, A. Shukurov, E. M. Berkhuijsen, R. Beck, and A. D. Poezd. Depolarization and Faraday effects in galaxies. *MNRAS*, Vol. 299, No. 1, pp. 189–206, August 1998.

[115] Aritra Basu, S. A. Mao, Andrew Fletcher, Nissim Kanekar, Anvar Shukurov, Dominic Schnitzeler, Valentina Vacca, and Henrik Junklewitz. Statistical properties of Faraday rotation measure in external galaxies - I. Intervening disc galaxies. *MNRAS*, Vol. 477, No. 2, pp. 2528–2546, June 2018.

[116] Hilay Shah and Amit Seta. Magnetic fields in elliptical galaxies: using the Laing-Garrington effect in radio galaxies and polarized emission from background radio sources. *MNRAS*, Vol. 508, No. 1, pp. 1371–1388, November 2021.

[117] Alison M. Hammond, Timothy Robishaw, and B. M. Gaensler. A New Catalog of Faraday Rotation Measures and Redshifts for Extragalactic Radio Sources. *arXiv e-prints*, p. arXiv:1209.1438, September 2012.

[118] M. L. Bernet, F. Miniati, and S. J. Lilly. The Interpretation of Rotation Measures in the Presence of Inhomogeneous Foreground Screens. *ApJ*, Vol. 761, No. 2, p. 144, December 2012.